International School for Advanced Studies
Trieste

THEORETICAL INVESTIGATIONS OF OPTICAL ABSORPTION AND OF TUNNELING BEHAVIOUR OF HETEROSTRUCTURES IN STRONG MAGNETIC FIELDS

Thesis submitted for the degree of
"Doctor Philosophiae"

CANDIDATE

Francesco Ancilotto

SUPERVISORS

Dr. Annalisa Fasolino
Dr. Annabella Selloni
Prof. Erio Tosatti

December 1988

Acknowledgements.

I wish to express my deep gratitude to my thesis supervisors Erio Tosatti, Annalisa Fasolino and Annabella Selloni, for their precious guidance and constant help throughout this work.

My sincere thanks to A.F. and A.S. for careful critical readings of the manuscript and for friendly encouragements during the early stages of this work.

I am indebted to J.C.Maan for an enlightening discussion on magneto-optical experiments in Quantum Wells.

Much of this work has relied on the facilities of the ICTP-SISSA computing center and I would like to thank its staff for help and friendly cooperation.

Contents

Introduction.

The recent improvement in epitaxial growth techniques has made it possible to obtain high-quality semiconductor heterostructures with interfaces sharp on an atomic scale. These "superlattice" structures possess unusual electronic properties of quasi-two dimensional character.

Of particular interest is the behaviour of such systems in an external magnetic field. In a strictly 2-D system, such as electrons or holes in a Quantum Well, a perpendicular magnetic field quantizes both available degrees of freedom, producing an entirely discrete spectrum. This leads, for instance, to an enrichment and sharpening of the optical spectra and also gives rise to new transport phenomena, the most noticeable being the Quantum Hall effect.

In this thesis we shall discuss a number of problems related to the behaviour of heterostructures in strong magnetic fields. The thesis is roughly divided into two parts. The first part (from Chapter 1 to Chapter 5) is mostly devoted to the study of magneto-optic effects in semiconductor Quantum Wells in the presence of a quantizing magnetic field applied perpendicularly to the Quantum Well layer. The second part (from Chapter 6 on) deals with the numerical simulation of tunneling in a magnetic field perpendicular to the current direction. In the following we introduce separately these two topics and provide at the same time a schematic layout of the thesis.

(a) Magneto-optics.

The magneto-optical absorption spectra of Quantum Well systems exhibit complex features that cannot be accounted for by simple models of quantum confinement. In particular, the degeneracy of the bulk valence bands and the effect of the confinement in the one-dimensional superlattice potential combine to produce strong non-parabolicities in the hole-subband

dispersion. This fact, together with the relaxation of the usual optical selection rules caused by the coupling between Heavy and Light Hole subbands, makes the comparison between theory and experiments rather difficult.

With the purpose of providing such a comparison, in **Chapter 3** we investigate the effect of mixing of the hole subbands on the interband magneto-optical spectra of a GaAs Quantum Well placed in an external magnetic field perpendicular to the Quantum Well growth axis. The calculations are performed within the six-band Envelope-Function approach described in detail in **Chapter 2**. Our results compare favorably with interband magneto-optical experimental data and help considerably in their understanding [58,59]. In particular, the explicit evaluation of the transition strengths is found essential for the explanation of the experimental results. The quantitative details of our calculations depend critically on the sample parameters, implying the possibility of their precise determination through the comparison between theory and magneto-optical experiments .

Another case where the explicit evaluation of transition strengths is very important, is the study of relaxation processes in Quantum Wells under excitation in a magnetic field. In **Chapter 4** we show that, by identifying the spin character involved in each of the inter-band transitions in magneto-absorption spectra, spin-relaxation experiments in Quantum Wells can be interpreted [78,79].

Finally, in **Chapter 5** we study the related topic of the intra-band Cyclotron Resonance of the 2-D holes in Quantum Wells, and compare the results of our theoretical calculations with available experimental data [83].

(b) Magneto-tunneling.

The present availability of high magnetic fields and high-quality semiconductor heterostructures has stimulated many experimental studies of magneto-transport in low-dimensional electronic systems. Most of the efforts has been devoted to the geometrical configuration of the Quantum Hall effect, i.e., the magnetic field is perpendicular to the electronic currents. A closely related topic, of increasing current interest, concerns the effect of a transverse magnetic field on the tunnel current through a barrier, separating, e.g., two semiconductors, where electrons are forced to execute cyclotron motion by tunneling through the barrier in the plane perpendicular to the field. In particular, the recent availability of ultra-low

semiconductor barriers, of thickness comparable with the cyclotron orbit radius, is raising new questions concerning the way in which the dynamics of tunneling is influenced by the field.

One possible way to gain insight into the time-dependence of a tunneling process is to use direct numerical simulations. After a brief overview of the basic concepts involved in single-particle tunneling, which forms the content of **Chapter 6**, we present in **Chapter 7** a numerical study of the three-dimensional time-dependent tunneling of a localized electron wavepacket through a thick barrier in the presence of a transverse magnetic field [152]. The time evolution of the packet density, current density and total current are described in detail. The current density profile, in particular, shows strong under-barrier currents which accompany tunneling. The center of mass of both the reflected and transmitted packet follow closely their semi-classical trajectories. However, very noticeable deformations are revealed by the full density contours. The total current is studied, and found to approach the classical "skipping" orbit current for very large times. The effective packet transmission coefficient of the barrier is field-dependent, and also depends upon the position relative to the barrier center x_c of the classical orbit center X_0 in absence of the barrier. Both these aspects are found to agree well with semi-classical WKB transmission formulae including an effective field-dependent barrier thickness. The packet center-of-mass delay time τ_{CM} is also studied, and compared with the zero-field value. It is argued that τ_{CM}, which is usually larger than the classical Wigner time, will tend towards the latter for very large magnetic fields.

The time dependence of resonant tunneling through a double-structure in a transverse magnetic field is also studied in Chapter 7 and compared with the zero-field tunneling. In particular, we find that the lifetime of the resonant level in the well has an oscillatory behavior with increasing magnetic field. This effect is explained as due to the field-induced hybridization of the quasi-local level inside the well with the interfacial magnetic levels just outside the confining barriers [153].

Although the systems studied in Chapters 7 are highly idealized, our results provide however interesting qualitative insight into the evolution, during the tunneling process, of relevant quantities like charge and current density. This seems of much potential importance for the future understanding of more complex situations, such as for instance the interaction

with impurities and disorder, as well as for time and space dependent perturbations.

A number of **Appendices**, containing results which are pertinent to the arguments faced in this thesis, is provided at the end.

Chapter 1

General considerations about semiconductor heterostructures.

1.1 Superlattices, Quantum Wells and Heterojunctions.

The steady improvement in the thin-film growth techniques such as Molecular Beam Epitaxy (MBE) [1] or Metal Organic Chemical Vapor Deposition (MOCVD) [2], has made possible to realize high quality semiconductor heterostructures composed of periodic sequences of ultra-thin crystalline layers ($10 - 1000\,\mathring{A}$) of alternating semiconducting compounds with interfaces sharp on an atomic scale: these artificial media exhibit novel properties not shown by their parent compounds in the bulk.

Interest in SuperLattices (**SL**), as these multilayer structures are usually called, originates from an early proposal [3] of a one-dimensional man-made "superlattice" having period shorter than the electron mean free path. These structures are generally grown alternating lattice-matched semiconductor compounds of group-III and group-V or group-II and group-VI elements; there are various reasons for this choice:

- these compounds have a direct band gap: this means that, since they can emit or absorb light without the help of lattice vibrations, they are particularly suited for the realization of opto-electronic devices;

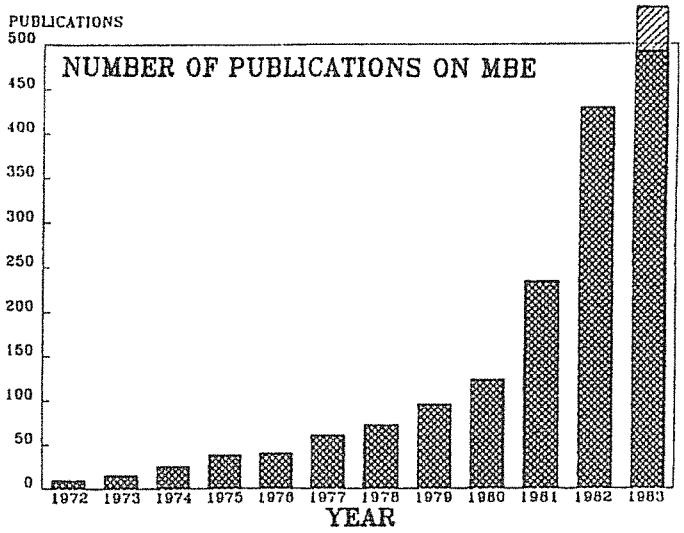

Figure 1.1: (From Ref.[4])

- they can be easily doped;
- they can form various solid solutions with identical crystal structure and well-matched lattice parameters but with different energy band gaps.

Table I gives a list of several SL systems, indicating where the major interest lies for each of them (from Ref.[5]). An almost exhaustive list of closely-matched pairs of binary and elemental semiconductors, including III-V/II-VI Superlattice systems, is given in Ref.[6].

SL structures possess unusual electronic properties of quasi-two dimensional character. The simplest case is that of an undoped GaAs layer (A layer) sandwiched between barrier-layers of $Al_x\ Ga_{1-x}As$ (B layer): the GaAs band gap is entirely contained within that of AlGaAs, the latter being a function of the alloy composition x (this is an example of the so-called "type-I" SL). The net potential is the sum of the potential in the A and B layer and of a square wave-shaped "superpotential" which arises from the band gap differences between A and B materials (see Fig.1.2). For thick AlGaAs barriers, the electron and hole wavefunctions are mainly localized in the A-layer, with evanescent wings in the adjacent B layers. In this case, the system is usually called a Quantum Well (QW).

However, if the decay length of the wavefunction in the B-layer is com-

Systems	*Techniques*	*Remarks*
GaAs-GaAlAs {AlAs}	MBE,MOCVD,LPE	Extensively studied
InAs{InGaAs}-GaSb{GaSbAs}	MBE	Extensively studied
GaSb-AlSb	MBE	Metallurgical and optical properties
InAs-AlSb	MBE	Optical and magnetoproperties
GaAs{GaP}-GaAsP	MOCVD,CVD	Strained superlattice, luminescence
GaAs-InAs{InGaAs}	MBE,MOCVD	Light-emitting properties
InP-InGaAs	MOCVD	Magnetoproperties
InP-InGaAsP	LPE	Light-emitting properties
InSb-GaSb	Sputtering	Ordered structure, interdiffusion
GaP-AlP		Theoretical indirect-direct gap
Ge-GaAs{GaAlAs}	MBE	Metallurgical properties, defects
Si-SiGe	MBE,CVD	Dislocations, mobility enhancement
CdTe-HgTe	MBE	Zero-finite gap
PbTe-PbSnTe	Hot-wall	Interdiffusion, magnetotransport
PbTe-PbGeTe	MBE	Dislocations, Auger profiling
InAs-GaSb-AlSb	MBE	Polytype superlattice
GaAs(n)-GaAs(p)	MBE	Doping superlattice, tunable gap

TABLE I

Semiconductor Superlattices

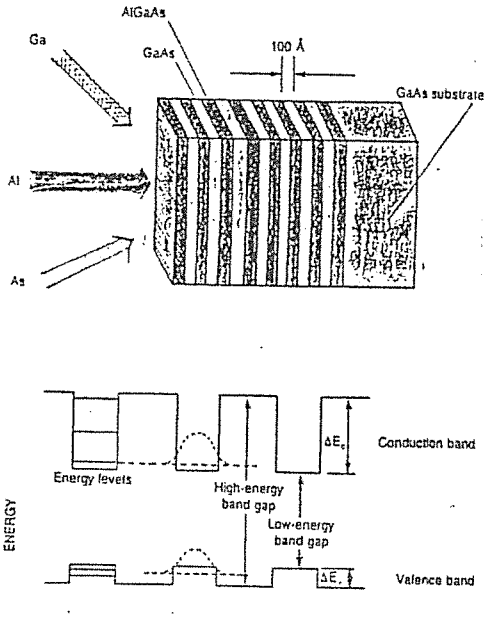

Figure 1.2:
Quantum Well structure and corresponding real-space energy band structure. The upper part of the Figure shows compositional profiling in thin layers.

parable with the width of the barrier, tunnelling of electrons (and holes) through these potential barriers can occur, leading to the formation of subbands having small but finite widths, which are the SL conduction bands (or minibands)[1]. The SL periodicity d (see Fig.1.3), superimposed on the lattice periodicity, leads to a division of the original Brillouin zone in subzones, with boundaries at wave vectors $k_z = n\pi/d$, n being an integer [2]. In the SL direction, i.e. perpendicularly to the layers, the original bulk bands are split into minibands separated by small bandgaps (minigaps), while the bands in the (k_x, k_y) direction (i.e. those corresponding to the motion in the plane of the layers) are practically unaffected by the SL periodicity. One is dealing, therefore, with a very asymmetric band structure with a bulk-like band width (typically $\sim$ 10 eV) in the k_x, k_y plane and narrow ($\sim$ 10 meV) bands in the k_z -direction. Quite recently, magneto-optical experiments on very thin SL in a magnetic field parallel to the plane of the SL layers have made possible a direct observation of minibands and minigaps [7]. In these experiments the electrons, in order to complete their cyclotron orbit, are forced to tunnel through several layers of the SL: as shown in Ref. [7], well defined peaks can be seen in interband magneto-luminescence only for transitions that originate from Landau levels within the electron and hole minibands. The analysis of the inter-subband optical transitions thus allows for a direct determination of the subband width.

Thus SL's present a duality of aspects, the QW aspect with quantized confinement energies, 2D density of states and localized wavefunctions, and the Superlattice aspect, with strong anisotropy in the Brillouin zone and the resulting small but finite bandwidth in the direction perpendicular to the layers. The dimensionality ($2D$ or $3D$) of a SL can thus be characterized by the subband width. A flat subband, corresponding to an infinite effective mass in the SL direction, means that successive layers do not interact (Quantum Well case). A QW is an almost ideal realization of the "particle-in-the-box" model: owing to the confinement of the carriers through the band gap discontinuity, the continuous spectrum of electrons and holes in

[1] For free electron wavefunctions the penetration depth into the barriers is just the de Broglie wavelength $\lambda = (\hbar^2/2m^*V)^{1/2}$, where $\hbar$ is the Planck's constant, m^* the effective mass of the electron and V the height of the confining potential barriers. Typical values for type I-SL are $V \sim 100$ meV, $m^* \sim 0.05 m_0$, leading to the value $\lambda \sim 30$ Å.

[2] We assume that the growth axis of an MBE heterostructure is in the $<001>$ direction, as it usually is.

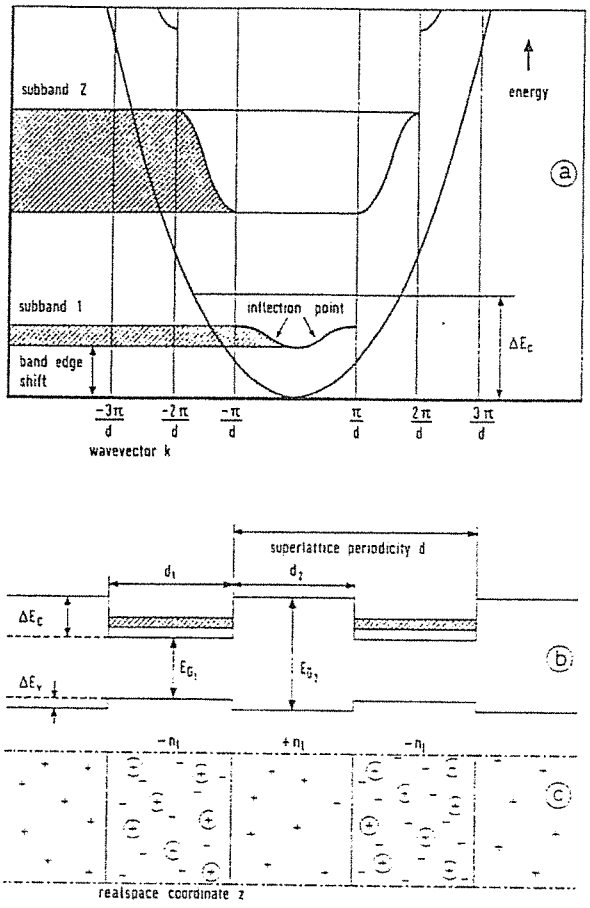

Figure 1.3:
Schematic energy level structure of a type-I superlattice. (a) shows the formation of subbands and the division of the Brillouin zone into subzones due to the periodic potential ΔE_c. These subbands result from the difference in band-gaps of the neighbouring materials as shown in (b). (c) shows the charge distribution in real space for a homogeneously doped superlattice.

the direction perpendicular to the layers is split into discrete energy levels. The quantized confinement energies of electrons and holes (measured from the conduction [valence] band edge) are of the order of

$$|E_n| = \pi^2\hbar^2 n^2/2m^*_{e[h]}L_z^2 \qquad , \qquad n = 1, 2, 3, ... \tag{1.1}$$

where $m^*_{e[h]}$ is the effective band-edge mass for the electron [hole] and L_z is the width of the Quantum Well. To each of these "particle-in-the-box" levels corresponds a two-dimensional density of states $m^*_{e[h]}/\pi\hbar$.

In particular, the effective band gap E_g^{eff} (difference between the lowest electron and highest hole level) increases with decreasing layer thickness (Quantum Size Effect), allowing to vary continuously the effective band gap over wide ranges, making in turn possible to tailor both the electronic and optical properties of QW's utilized in practical devices.

The simple "particle in the box" model fails however to describe fully the experimental observations on QW's; for instance, it neglects *excitonic effects* which are expected to play an important role in these systems: the excitonic binding energy in a thin GaAs layer is significantly higher than that in the bulk material, due to the quasi-two dimensional nature of the exciton (a brief introduction to excitonic effects in SL structures is given in Appendix G). Furthermore, a realistic description of the bulk band structure of the constituent materials must include necessarily *band coupling* and *degeneracies*. These facts are important especially for the dispersion relations in the plane of the layers which is not trivial for states derived from coupled bands such as the p-like valence bands of all III-V semiconducting compounds. In Chapters 3 and 4 of this thesis we will be mostly concerned precisely with the effect of band mixing on the magneto-absorption in Quantum Wells.

The simple square-well profile of Fig.1.2 is substantially modified in the so-called "modulation doped" GaAs/GaAlAs SL (see Fig.1.4, from Ref.[8]), due to the band-edge curvature produced by space-charge effects. In these systems electrons from the donors in the doped barriers are transferred to the undoped wells. The resulting space charge of alternating sign cause a periodic bending of the band-edges, as shown in Fig.1.4. The electrons, which occupy the QW states up to the Fermi level E_F, are spatially separated from their parent donor impurities. As a result, they can propagate within the GaAs layers with strongly reduced probability of being scattered by the ionized impurities. In this way a great enhancement of the

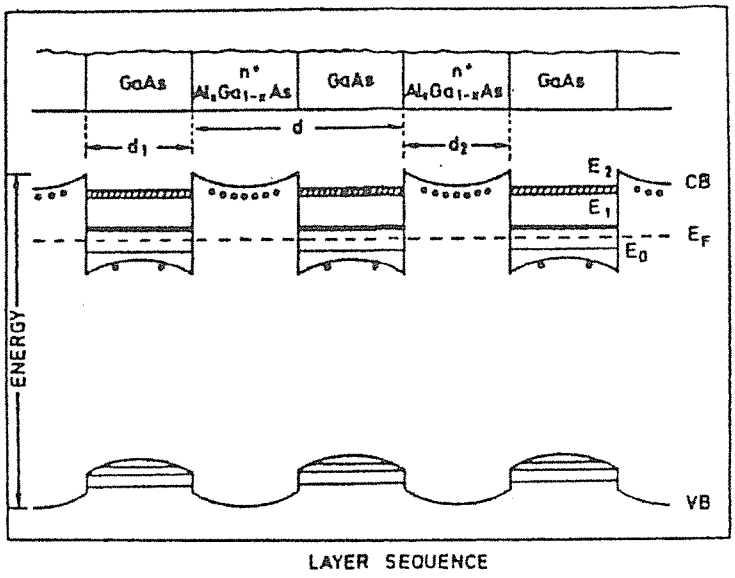

Figure 1.4:
Schematic illustration of layer sequence in modulation doped $Al_xGa_{1-x}As/GaAs$ superlattices (top) and of corresponding real-space energy band diagram (bottom, not to scale). The band bending at the constituent AlGaAs/GaAs interfaces arises from the space charges, due to a spatial transfer of free-electrons from the ionized donors in the AlGaAs barriers into the GaAs wells.

mobility with respect to the bulk value can be achieved. In fact, peak mobilities in excess of $10^6\, cm^2/Vs$ at $4^\circ K$ have been measured for electrons in GaAs-modulation doped QW's, about three orders of magnitude higher than those measured in bulk materials [9]. The same technique can be used to form high-mobility 2D-hole gas. This had a profound impact in device applications, leading for instance to the fabrication of high-speed MODFET (Modulation Doped Field Effect Transistors) [10].

A typical length that must be considered when free charges coming from dopant impurities are present is the *screening length*. For degenerate materials it is given by the Thomas-Fermi expression $\lambda_{TF} = (\varepsilon E_F/6\pi e^2 n_0)^{1/2}$, where E_F is the Fermi energy, n_0 is the net free-carrier concentration and ε is the dielectric constant of the material. For a typical degenerate semiconductor with $n_0 \sim 5 \times 10^{17}\, cm^{-3}$ and $\varepsilon \sim 12$, this results in a screening length λ_{TF} of the order of 90 $\mathring{A}$. If the layer thickness is much less than λ_{TF}, the charge can be considered as homogeneously distributed over the layer. In the opposite case the charge will be redistributed across the interface and electrons and holes will accumulate on the two sides of the interface: this situation is typical for **heterojunctions**. The resulting potential can be calculated by using the Poisson's equation: in general the problem must be solved self consistently because the charge distribution is the result of the band structure, that in turn depends on the charge distribution itself. Fig.1.5 shows schematically the band bending profile resulting from the transfer of charge released from donor or acceptor atoms: in the case represented the heterojunction is made of n-doped GaAs/p-doped GaAlAs. Note the roughly triangular potential well binding the holes and resulting from the ionization of the impurities in the depletion layer. Note that this system, in contrast to SL and QW, lacks inversion symmetry: this leads to a removal of the Kramer's spin degeneracy (much larger than the one already present in bulk GaAs because of inversion symmetry breaking owing to the difference between Ga and As ionic potentials).

1.2 Various types of Superlattices.

Hetero-interfaces can be classified roughly into four kinds: type I, type II-staggered, type II-misaligned and type III SL's, as illustrated in Fig.1.6 (taken from Ref. [11]).

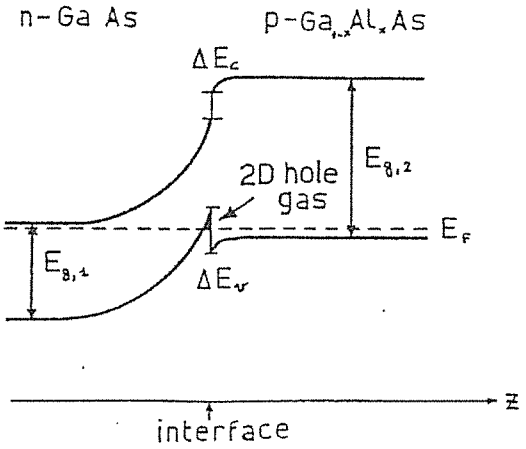

Energy band profile of a modulation doped heterojunction made of an n-doped GaAs layer grown on a p-doped GaAlAs layer.
Holes are confined near the interface where a 2D hole gas is formed.
z is the coordinate of the growth axis.

Figure 1.5:

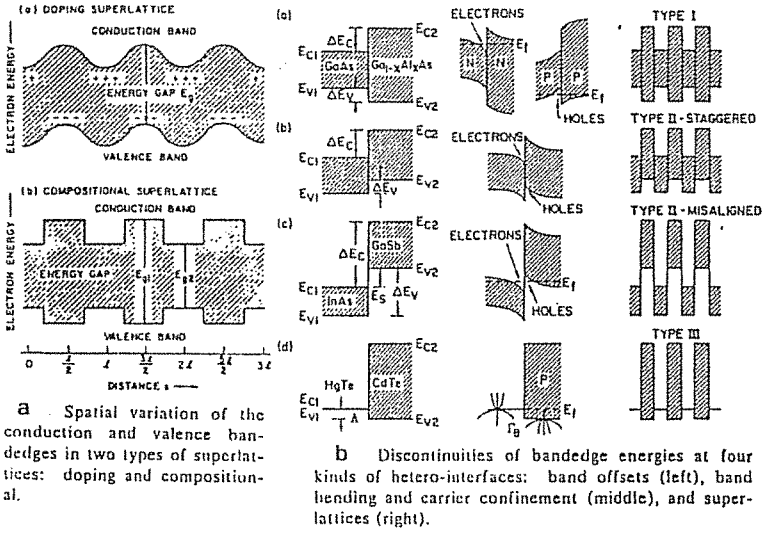

a Spatial variation of the conduction and valence bandedges in two types of superlattices: doping and compositional.

b Discontinuities of bandedge energies at four kinds of hetero-interfaces: band offsets (left), band bending and carrier confinement (middle), and superlattices (right).

Figure 1.6: Types of Superlattices.

This classification reflects the different ways in which the band-gap discontinuity $E_{g1} - E_{g2}$ is shared between valence and conduction bands.

The most investigated case is that of undoped GaAs/Ga_{1-x} Al_x As heterostructure, where the GaAs bandgap is entirely contained within that of GaAlAs, leading to the square wave modulated potential for the valence and the conduction band schematically shown in Fig.1.6a. This is an example of type I superlattice.

The so called 'type II-staggered' SL's differs from its type I counterpart by the sign of the band edge discontinuity between the two components of the structure. In this kind of SL, conduction and valence subband wavefunctions are concentrated in different regions: we are thus dealing with an 'indirect band gap in real space'. The spatial separation between electron and hole states reduces the dipole matrix elements for transitions between conduction and valence subbands, thus increasing considerably the radiative electron-hole recombination time.

The binary system $InAs/GaSb$ (type II-misaligned) is characterized by the very unusual band-edge profile shown in Fig.1.6b: in this case the conduction band edge of $InAs$ is lower in energy than the valence band edge of $GaSb$, by about 0.15 eV. Charge transfer across the interface is therefore to be expected: experiments show that when the layer thickness reaches a critical value of about 180 $\AA$, a sudden increase in the effective carrier concentration is observed [12]. This transition can easily be understood in a simple double-confinement model; for thicker layers, electrons (and holes) become less confined and the lowest (highest) subband approaches the bulk band-edge: consequently, at some point the subbands must cross, showing a semiconductor-semimetal transition. Theoretical calculations [13] based on an Effective Mass approach show that actually a small hybridization gap of a few meV opens up at the Fermi energy, producing a very narrow-gap semiconductor rather than a semimetal: the semimetallic behavior observed is then probably produced by extrinsic effects .

The unique member of the type III family is the II-VI $HgTe/CdTe$ system (see, for instance, Ref. [14]) where $HgTe$ is a zero-gap semiconductor due to the inversion of the relative position of Γ_6 and Γ_8 edges; the Γ_8 Light Hole band in $CdTe$ becomes the conduction band in $HgTe$, where their energy difference Λ (see Fig.1.6b) was determined to be ~ 40 meV.

In a modulation doped superlattice (see Fig.1.6a), where the periodic potential is induced by space charge effects resulting from an alternated

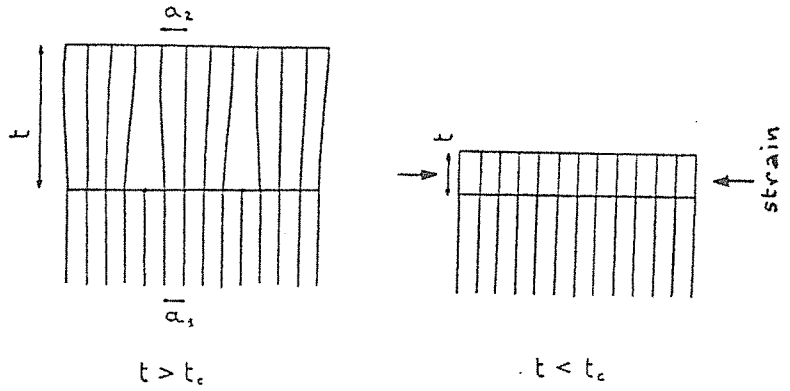

Figure 1.7:

doping (e.g., n-GaAs/p-GaAs) of the same semiconductor compound , the spatial separation between the electrons and their parent donor impurities reduces drastically the Coulomb scattering and thus enhances greatly the mobility of the electrons. A recent review on the fundamental properties of Modulation Doped Superlattices is contained in Ref. [8].

1.3 Strained Layer Superlattices

The requirement of a nearly perfect lattice match between the constituents of a semiconductor-semiconductor interface can, at certain conditions, be relaxed. Good superlattices with much more severely mismatched semiconductor materials than, for instance, GaAs/AlGaAs, can in fact be grown [16]. For sufficiently thin layers -up to about 300 $\AA$ - alternating materials with lattice constants a differing by as much as a few percent will accommodate themselves by elastic deformation to a compromise lattice constant, giving rise to Strained Layer Superlattices (SLSL) [15]. Fig.1.7 shows schematically that for thicker layers a significant lattice mismatch will be accomodated by the creation of more or less regularly spaced misfit dislocations at the interface.

SLSL come out to be astonishingly free of the interface dislocations that would have destroyed those optical and electrical properties that are desirable in a SL. In particular, theoretical and experimental analysis of SLSL made of mismatched ($\delta a/a \gtrsim 1\%$) ternary compounds such as $In_x Ga_{1-x}$ As or $GaAs_xP_{1-x}$, indicate that by varying their layer thickness and composition one can vary, continuously and independently of one another,

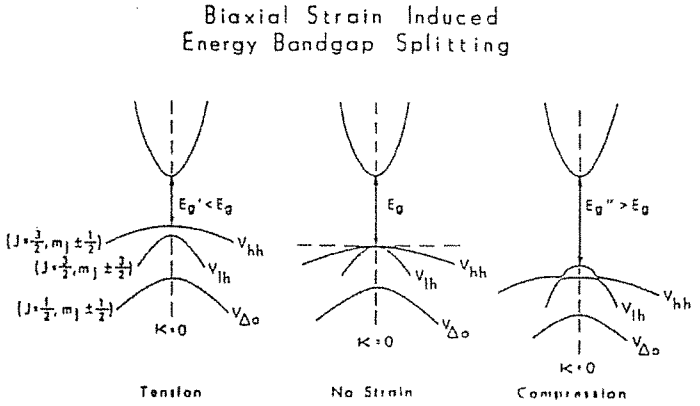

Figure 1.8:
Representation of the energy band-gap splittings and shifts caused by mismatch strain in the epitaxial layer. The biaxial shear strain lifts the degeneracy of Light- and Heavy-hole valence bands at $k = 0$.

the lattice constants, the forbidden energy gap and the transverse carrier mobility of the overall SL [16]. Recently, optical absorption measurements in $GaSb/AlSb$ SLSL have also shown a reversal of the Heavy Hole and Light Hole exciton peak position: the ground valence state in these structures is the Light hole level [17]. This effect can be understood by noting that: (i) a biaxial tensile stress resulting from the lattice mismatch acts on the $GaSb$ layer, which is stretched in the direction of the layer plane; (ii) as a result of this strain the degeneracy of Light and Heavy hole valence bands at $k = 0$ is lifted (see Fig.1.8).

These facts, together with the competing splitting of valence bands due to the quantum confinement, are responsible for the mentioned observed behavior. Another consequence of this elastic deformation in $GaSb/AlSb$ system is an observed band-gap shrinkage of about 50 meV .

Between SLSL systems, the combination of Si and $SiGe$ (lattice mismatch ~ 4 %) is very attractive due to the possibility, as a result of Brillouin zone folding, of making a direct-gap SL starting from indirect-gap host materials [18]. In particular, $Si/SiGe$ multilayer structures are of potential interest in opto-electronic applications, since the band-gap of bulk Si_xGe_{1-x} lies in the interesting range of optical fiber communications.

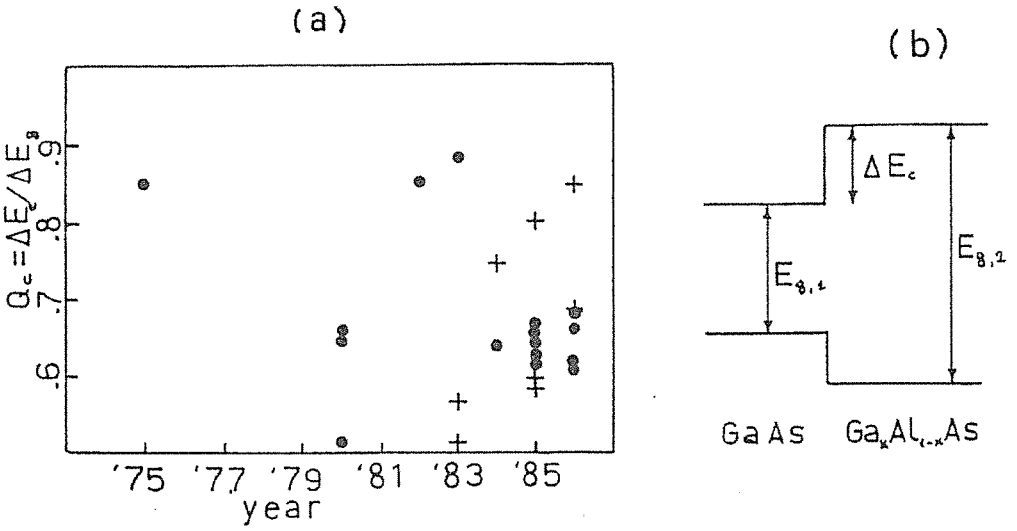

Figure 1.9:
Experimental determinations of the conduction-band discontinuity $Q_c = \Delta E_c/(E_{g,2} - E_{g,1})$ vs. year. Dots and crosses mean that optical and electrical methods of measure, respectively, have been used.

1.4 Band offset in GaAs/AlGaAs heterostructures.

A relevant input parameter for the calculation of energy levels in heterostructures is the band gap discontinuity, i.e. the relative energy position between the conduction band edges of the two constituent materials (see Fig.1.9b). This parameter determines the height of the barriers confining the particles in the quantum wells and thus controls the distribution and flow of mobile carriers. In spite of its central role this quantity is not accurately known, even for extensively investigated systems like $GaAs/Ga_{1-x}Al_xAs$. As can be seen in Fig.1.9a, the published experimental values of $Q_c = \Delta E_c/\Delta E_g$ are quite scattered even in recent years, ranging from the 85% of the earliest determination [19] to the more recent 60% [20]. The experiments do not seem to indicate any relevant dependence of Q_c on the *Al* concentration x. The most accurate estimate, based on anelastic light scattering by photoexcited electrons, gave $Q_c = 0.69 \pm 0.03$, $(x = .06)$ [21]: this method doesn't suffer from the large amount of uncertainty usually present in optical determination of band-offset (primarily because of the complicated valence band structure and of excitonic effects) since it involves only electronic subbands. Also, it allows a direct measurement of

the total discontinuity $\Delta E = E_{g1} - E_{g2}$, so that an exact knowledge of the alloy composition x is no longer needed. Theoretical predictions can hardly be of any help, given the normal uncertainty ($\gtrsim 0.1$ eV) of the best band-calculations in bulk materials. We note in passing that the oldest and simplest model used to predict semiconductor - semiconductor band lineup, based on the assumption that the conduction band discontinuity Q is simply equal to the difference between the electron affinities of the two materials, has proven to be incorrect [22].

Chapter 2

The Envelope Function Approximation.

2.1 The Envelope Function Approximation.

An approach to the description of electronic states in semiconductor heterostructures that has proved to be simple, versatile and accurate is based on the "Envelope Function" (**EF**) method ([23,24]). We briefly discuss in the following the basic equations of the EF approach in the simple case of an isotropic, non-degenerate conduction and valence bands with an extremum at $\mathbf{k} = 0$, in the scheme provided by the Effective Mass (**EM**) theory (for a detailed derivation, see Appendix A). We then consider the problem of imposing the appropriate boundary conditions on the envelope function at a sharp interface between two different semiconductors. The approach to the more realistic, although quite complex, problem involving degenerate bands will be treated in Sect.2.4 and in Appendix D.

2.2 The Effective Mass Equation.

We will quote only the main results of EM theory in a simple one band case (a detailed derivation is contained in Appendix A). Consider the motion of an electron in a semiconductor, in the presence of some external potential $U(\mathbf{r})$; the Schrodinger equation is:

$$[p^2/2m + V_c(\mathbf{r}) + U(\mathbf{r}) - E]\Psi(\mathbf{r}) = 0 \qquad (2.1)$$

For instance, $U(\mathbf{r})$ could be the band-bending potential at the interface shown schematically in Fig.1.5. If the additional potential is slowly varying and weak, the wave function $\Psi(\mathbf{r})$ is approximately given by the $\mathbf{k} \cdot \mathbf{p}$ expansion (see Appendix B for a detailed derivation):

$$\Psi(\mathbf{r}) = F_n(\mathbf{r})u_{n0}(\mathbf{r}) + (1/m)\sum_{n' \neq n} \frac{-i[\nabla F_n(\mathbf{r})] \cdot p_{nn'}}{E_n(0) - E_{n'}(0)} u_{n'0}(\mathbf{r}) \qquad (2.2)$$

Eq.(2.2) is the basic result of the EF approach. It shows that, to lowest order, the wavefunction $\Psi(\mathbf{r})$ is given by a slowly varying "envelope" function $F(\mathbf{r})$ modulating the rapidly varying Bloch part $u_{n0}(\mathbf{r})$. The second term is a correction arising from the coupling with other bands, as it is obtained in the $\mathbf{k} \cdot \mathbf{p}$ method (see Appendix B).

The envelope function $F(\mathbf{r})$ satisfies the Effective Mass Equation (A.17), that is:

$$[-\frac{\hbar^2}{2m^*}\nabla^2 + U(\mathbf{r})]F(\mathbf{r}) = [E - E_n(0)]F_n(\mathbf{r}) \qquad (2.3)$$

The energy E of the electron, in the case of a simple, isotropic band extremum (e.g. the conduction band minimum in GaAs semiconductor) is given by:

$$E_n(\mathbf{k}) = E_n(0) + \hbar^2 k^2/2m^* \qquad (2.4a)$$

where

$$1/m^* = 1/m + (2/m^2)\sum_{n' \neq n} \frac{p^\alpha_{nn'} p^\alpha_{n'n}}{E_n(0) - E_{n'}(0)} \quad , \quad \alpha = x, y, z \qquad (2.4b)$$

2.3 Boundary conditions for the Envelope Function.

In the EM equation (2.3) for the envelope function, all reference to the microscopic structure of the host semiconductor is condensed in the effective

mass m^* and the band edge energy $E_n(0)$. These two parameters assume different values in the two semiconductors, say A and B, making up an interface system. Thus one could think of writing a more general form of the Eq.(2.3), in which the effective mass and the band edge vary as a function of z, the coordinate of the axis perpendicular to the interface.

$$[-\frac{\hbar^2}{2}\nabla\cdot(\frac{1}{m^*(z)}\nabla)]F(\mathbf{r}) = [E - E_n(0,z) - U(\mathbf{r})]F(\mathbf{r}) \qquad (2.5)$$

$z = 0$ is assumed to coincide with the interface plane. The kinetic energy term in the first member has been written in a way that restores the Hermitean character of the EM Hamiltonian . Typically, the transition region between A and B material include only a few atomic layers: the potential term in Eq.(2.5) is thus rapidly varying near the interface, contrarily to the fundamental assumption of the EM theory (see Appendix A), and the whole EM formalism becomes questionable. Nevertheless, it is possible to provide the EM equation with boundary conditions that makes it useful also in the case of abrupt junctions, by means of the following argument[24].

Assume that an abrupt heterojunction is located at $z = 0$. Then for $z < 0$, $m^* = m_A^*$ and $E_n(0) = E_n^A(0)$; for $z > 0$, $m^* = m_B^*$ and $E_n(0) = E_n^B(0)$. One now imposes the reasonable requirement that $F(z)$ be finite everywhere: thus the right-hand side of Eq.(2.5) is finite, having only a finite discontinuity at the interface. The left-hand side must be similarly well behaved; this implies

$$\frac{d}{dz}(\frac{1}{m^*})\frac{dF}{dz} \quad \textit{finite for all } z \qquad (2.6)$$

By integrating the preceding expression between $z = -\varepsilon$ and $z = +\varepsilon$ and taking the limit $\varepsilon \to 0$, one is lead to the conclusion (first derived in Ref.[23]):

$$(\frac{1}{m^*})\frac{dF}{dz} \quad \textit{continuous at the interface} \qquad (2.7)$$

The existence of stationary states (probability density constant in time) implies that the z-component of the current be the same on all planes parallel to the interface and therefore also that its average over a microscopic volume Ω, including one or few unit cells, be the same on both sides of the interface. One finds, for the average current $\bar{J}$ in A-material:

$$\bar{J}_A = (\hbar/m) Im \int_\Omega \Psi_A^* \frac{\partial}{\partial z} \Psi_A d\mathbf{r} = (\hbar/m_A^*) Im[F^{A*}(0) \frac{\partial}{\partial z} F^A(0)] \qquad (2.8)$$

Therefore the continuity of $\bar{J}$ implies:

$$(\hbar/m_A^*) Im[F^{A*}(0) \frac{\partial}{\partial z} F^A(0)] = (\hbar/m_B^*) Im[F^{B*}(0) \frac{\partial}{\partial z} F^B(0)] \qquad (2.9)$$

One can see that, from the condition (2.7) together with the requirement that $F(z)$ be continuous across the junction

$$F^A(0^-) = F^B(0^+) \qquad (2.10)$$

it follows that the current $\bar{J}(z)$ is continuous across the interface. It is easy to show furthermore that the Hamiltonian appearing in Eq.(2.5) is consistent with the conserved current $\bar{J}(z)$, that is the usual continuity equation holds for the probability density $F^{i*}F^i$ in each material:

$$\frac{d|F^i|^2}{dt} + \frac{d\bar{J}_i(z)}{dz} = 0 \quad , \quad i = A, B \qquad (2.11)$$

It is now clear that the boundary conditions (2.7,2.10) on the envelope function imply that the average of the probability current is constant. They are, therefore, significant on physical grounds and can be safely adopted in the treatment of heterostructures. From the condition (2.10), the continuity of the total wavefunction (2.2) implies [1]

$$u_n^A \simeq u_n^B \qquad (2.12)$$

(We drop, from now on, the subscript '0' in the Bloch part of the wavefunction). The above assumption is plausible, given the structural and chemical similarities of the III-V compounds, as long as one is considering the same band edge on both side of the interface.

[1] It is also assumed that the second term in the wavefunction (2.2) is small.

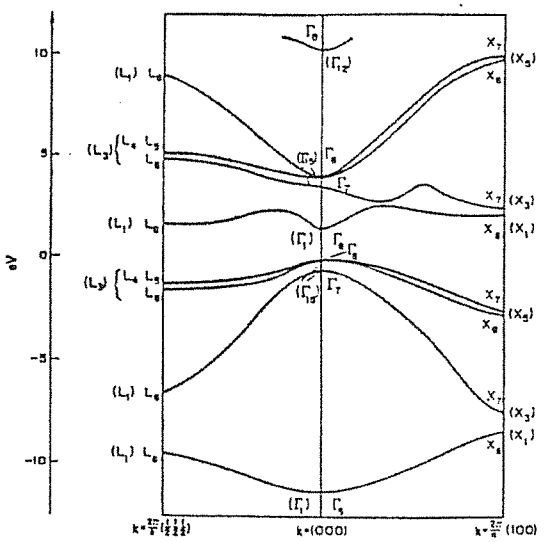

Energy bands for GaAs with the inclusion of spin-orbit interaction. The irreducible representations for the states of the simple group are supplied in brackets.

(a)

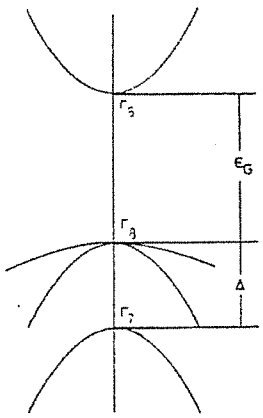

schematic illustration of the band structure in III-V semiconductors near the Γ point. Γ_6 is the conduction band, Γ_8 gives the heavy and light holes, and Γ_7 is called the spin-splitoff band.

(b)

Figure 2.1: GaAs band structure.

2.4 Coupled bands.

The simple band approach that has been outlined in the previous paragraphs cannot be used in practice in many situations of interest. This may happen because of:

- Band degeneracy near an extremum, as in the valence band maximum at Γ in all cubic semiconductors.
- Coupling between bands that produces deviations from parabolicity, as in the conduction band of direct gap semiconductors.

In the case of GaAs, which is of interest here, this non parabolicity has a sizeable effect on levels with energy $\gtrsim$ 100 meV above the band minimum: since this energy is comparable with the confinement energy of an electron in a typical superlattice, this effect cannot be neglected.

Let's consider explicitly the case of the III-V compound GaAs. In Fig.2.1a we show the calculated energy bands for GaAs, with the inclusion of spin-orbit interaction (from Ref.[25]).

The top of the valence band is at k = 0; the non-relativistic bands are six-fold degenerate (including the spin degeneracy) at Γ point, with sym-

metry Γ_{15} (p-like orbitals). The additional spin-orbit interaction couples operators in spin space and ordinary space and thus reduce the symmetry: the Γ_{15} states are split into Γ_7 and Γ_8 states; the upper manifold is four-fold degenerate and can be classified with the total angular momentum quantum number J=3/2, the four states thus corresponding to $J_z = \pm 1/2, \pm 3/2$; the Γ_7 states are two-fold degenerate and correspond to $J_z = \pm 1/2$. The spin-orbit interaction is very important in narrow-gap semiconductors, where it produces valence band splittings as big as the main gap. In the case of GaAs, the splitting Δ (see Fig.2.1b) is found to be 0.341 eV, while the value of the energy gap is $E_g = 1.519$ eV (at $4^\circ K$). Even if we regard the interaction between states Γ_7 and Γ_8 as being very small, we still have a degenerate problem and we must include the interaction between the two bands that go into Γ_8 at $\mathrm{k} = 0$. The problem is then to derive an extended version of the Effective Mass equation (2.3) in this case: one cannot use the simple procedure outlined in Appendix A since the band structure is not a single valued function of k and cannot be simply written as a Taylor expansion.

It can be shown [26] that, in a standard second-order $\mathbf{k} \cdot \mathbf{p}$ description of a set of coupled band edges at the Γ-point of a direct gap semiconductor, the band structure at a given k-value is given by the eigenvalues of an $N \times N$ matrix:

$$H_{ij}(\mathrm{k}) = \sum_{\alpha,\beta} D_{ij}^{\alpha\beta} k_\alpha k_\beta + \sum_{\alpha} P_{ij}^{\alpha} k_\alpha + E_i \delta_{ij} \qquad (i,j = 1,2,...,N) \quad (2.13)$$

where α, β run over x, y and z and N is the number of bulk bands that contribute with comparable weight to the formation of the wavefunctions. The E_i are the band-edge energies for the N band considered. The terms $P_{ij}^{\alpha} k_\alpha$ in Eq.(2.13), where the matrix P^α is defined as $P_{ij}^{\alpha} = (\hbar/m) < u_i | p_\alpha | u_j >$, represent the first order direct $\mathbf{k} \cdot \mathbf{p}$ interactions between the N bands, while the quadratic terms $D_{ij}^{\alpha\beta} k_\alpha k_\beta$ represent the indirect $\mathbf{k} \cdot \mathbf{p}$ coupling between two of the N bands via the other bands not included explicitly in the set. The form of the matrix depends on the choice of the unperturbed functions at $\mathrm{k} = 0$.

To give a specific example, consider the six-bands $\mathbf{k} \cdot \mathbf{p}$ matrix given in Appendix C (atomic units, in which $\hbar = m = 1$, are used in that Appendix and will be used in the text from now on), which represents the conduction

band and the upper spin-orbit split component of the valence band in a direct-gap semiconductor. (in the case of GaAs, these states are the Γ_6 and Γ_8 edges in Fig.2.1b): this matrix is known to give a very accurate description of these bands near k = 0 for materials with large spin-orbit splittings. One has a conduction band with s-like character at Γ_6 and two spin states $s\uparrow$ and $s\downarrow$. The parameter P is defined in terms of the interband momentum matrix element

$$P = -i < s|p_x|x > \tag{2.14}$$

where $|x>$ indicates the valence band state that transforms as an atomic p_x -like function under the symmetry operations of the cubic group T_d and $|s>$ indicates the conduction wavefunction at Γ_6. The effective mass m^* appearing in the corresponding diagonal terms originates from the coupling to the bands not included in the set, and primarily from the split-off valence band. One finds [27]: $(m^*)^{-1} = 1 + 2P^2/3(E_c - E_v + \Delta)$, where Δ is the valence band spin-orbit splitting and E_c, E_v are the conduction and valence band edges at the Γ-point. The basis set used in the representation of Appendix C consists of the (J, J_z) functions for a total angular momentum $J = 3/2$ [28]

$$\begin{aligned}
u_1 &= |s\uparrow> \\
u_2 &= |3/2;\, 3/2> = |\frac{1}{\sqrt{2}}(x+iy)\uparrow> \\
u_3 &= |3/2;\, -1/2> = |-\frac{1}{\sqrt{6}}(x-iy)\uparrow - \sqrt{\frac{2}{3}}z\downarrow> \\
u_4 &= |s\downarrow> \\
u_5 &= |3/2;\, 1/2> = |-\sqrt{\frac{2}{3}}z\uparrow + \frac{1}{\sqrt{6}}(x+iy)\downarrow> \\
u_6 &= |3/2;\, -3/2> = |-\sqrt{\frac{1}{2}}(x-iy)\downarrow>
\end{aligned} \tag{2.15}$$

where $|x>$, $|y>$, $|z>$ are valence p-like band states and the symbols $\uparrow$ and $\downarrow$ denote the spin "up" and "down" states respectively.

The parameters γ_1, γ_2, γ_3, κ and P which appear in the matrix (C.1) are specific of each material and represent, together with the band edges

TABLE II

Material parameters used in the calculations.

Band parameters		
	GaAs	AlAs[a]
P (a.u.)	8.78[b]	8.78
γ_1 (")	2.41	1.29
γ_2 (")	-0.12	-0.40
γ_3 (")	0.68	0.21
κ (")	-1.02	-0.96
$E_g(eV)$	1.53[c]	3.13[d]
$\Delta(eV)$	0.34	0.27

[a] Linear interpolation is used for $Al_xGa_{1-x}As$.

[b] corresponding to the value $m^*=0.074$ for the electron mass.

[c] The energy gap of GaAs at $0°K$ is 1.52 eV : the 10 meV difference is due to the presence of a slight amount ($\leq 1\%$) of Al in the GaAs well of the sample analyzed.

[d] The energy gap for $Al_xGa_{1-x}As$ is: $E_g(x)=E_g^{GaAs}+1.155x+0.37x^2$.

positions E_j, the only input parameters required for the energy band calculation in an EM Theory. Usually they are determined experimentally by fitting cyclotron resonance data: their values for GaAs and AlAs are listed in Table II, those of AlGaAs following by linear interpolation.

The extension of the Effective Mass equation (2.3) to the many-band case, in analogy with the many-band EM equation used in the theory of acceptor impurities [30], is represented by the following system of N differential coupled equations

$$\sum_{j=1}^{N}[H_{ij}(-i\nabla)+U(\mathrm{r})\delta_{ij}]F_j(\mathrm{r})=EF_i(\mathrm{r}) \qquad (2.16)$$

for the N-component envelope function $F_i(\mathbf{r})$, $i = 1, 2, ..., N$; H_{ij} is the Hamiltonian matrix (2.13). The total wavefunction $\Psi(\mathbf{r})$ is expressed, in analogy with Eq.(2.2), as

$$\Psi(\mathbf{r}) = \sum_j \{F_j(\mathbf{r})u_j(\mathbf{r}) + (\frac{1}{m}) \sum_{j'>N} \frac{-i[\nabla F_{j'}(\mathbf{r})] \cdot \mathbf{p}_{j'j}}{[E_j(0) - E_{j'}(0)]} u_{j'}(\mathbf{r})\} \qquad (2.17)$$

The second term in (2.17) represents a correction (to first order in $\mathbf{k}\cdot\mathbf{p}$) due to higher bands and can, for many purposes, be neglected.

We note in Eq.(2.16) that the kinetic energy part is just obtained by replacing $\mathbf{k}$ with $-i\nabla$ in the $\mathbf{k} \cdot \mathbf{p}$ matrix, and that the potential energy term is diagonal in the band index; this is a consequence of its slow spatial variation: as it can be taken as a constant in each unit cell, its off-diagonal matrix elements vanish by Bloch function orthogonality.

The generalization of the boundary conditions (2.7),(2.10) in the many-band case is quite straightforward and is discussed briefly in Appendix D.

2.5 Subbands in quantum wells and superlattices.

Consider again the $\mathbf{k}\cdot\mathbf{p}$ matrix introduced in the previous Section (Eq.(C.1) in Appendix C).

The dispersion in the k_z direction, corresponding to motion normal to the SL layers, is relatively simple to handle, since most of the diagonal terms in the matrix vanish for k_x, $k_y = 0$. In particular one sees that the $J_z = \pm 3/2$ states, corresponding to the Heavy Holes (**HH**), completely decouple from the other bands; their dispersion is purely parabolic, with an effective mass $m^*_{HH} = (\gamma_1 - 2\gamma_2)^{-1}$. In a superlattice geometry one thus has a Krönig-Penney type of eigenvalue problem, with the boundary conditions (2.7),(2.10). The dispersion relation can be found analytically and is given implicitly by the following equation [23]:

$$\begin{aligned} cos(k_z d) &= cos(k_{zA} d_A) cos(k_{zB} d_B) - \frac{1}{2}(m^A_{HH} k_{zB}/m^B_{HH} k_{zA} + \\ &\quad + m^B_{HH} k_{zA}/m^A_{HH} k_{zB}) sin(k_{zA} d_A) sin(k_{zB} d_B) \qquad (2.18) \end{aligned}$$

where $k^2_{zA,B} = 2m^{A,B}_{HH}(E - E^{A,B}_V)$: d_A, d_B are the layer thickness and $E^{A,B}_V$ are the valence band-edges in the A and B material respectively. As for the $J_z = \pm 1/2$ states (corresponding to the Light Holes (LH)) and the conduction electron states, one still has a 2×2 matrix between states $s\uparrow$ and $J_z = +1/2$ (and an equivalent one for $s\downarrow$ and $J_z = -1/2$).

Consider now the dispersion in the (k_x, k_y)-plane, corresponding to motion within the SL layer. If one is interested in the energy region close to the valence band top, then the conduction band can be ignored altogether, i.e. one removes rows and columns 1 and 4 in the matrix (C.1). The parameters γ_1, γ_2, γ_3 and κ must be renormalized, to take into account the coupling with these states [31]:

$$\begin{aligned} \gamma_1^L &= \gamma_1 + \frac{2P^2}{3E_g} \\ \gamma_{2,3}^L &= \gamma_{2,3} + \frac{P^2}{3E_g} \\ \kappa^L &= \kappa + \frac{P^2}{3E_g} \end{aligned} \qquad (2.19)$$

The resulting 4×4 matrix is the well-known Luttinger-Köhn Hamiltonian [32] describing the Light and Heavy hole bands in cubic semiconductor:

$$\hat{H} = E_v \hat{I} + \frac{\hbar^2}{2m} \begin{vmatrix} A_+ & B & C & 0 \\ B^* & A_- & 0 & C \\ C^* & 0 & A_- & -B \\ 0 & C^* & -B^* & A_+ \end{vmatrix} \qquad (2.20)$$

where:

$$\begin{aligned} A_\pm &= -(\gamma_1^L \pm \gamma_2^L)(k_x^2 + k_y^2) - (\gamma_1^L \mp 2\gamma_2^L)k_z^2 \\ B &= 2\sqrt{3}\gamma_3^L[\{k_z, k_x\} - i\{k_y, k_z\}] \\ C &= \sqrt{3}[\gamma_2^L(k_x^2 - k_y^2) - 2i\gamma_3^L\{k_x, k_y\}] \end{aligned} \qquad (2.21)$$

Here $\hat{I}$ is a unit 4×4 matrix and $\{..,..\}$ denotes the anticommutator [2].

[2] We prefer to quote this more general form of the Luttinger-Kohn Hamiltonian, written in terms of the anticommutators $\{k_x, k_y\}$ in view of its application when a magnetic field is present (see Chapter 3), in which case the different k_i components do not in general commute.

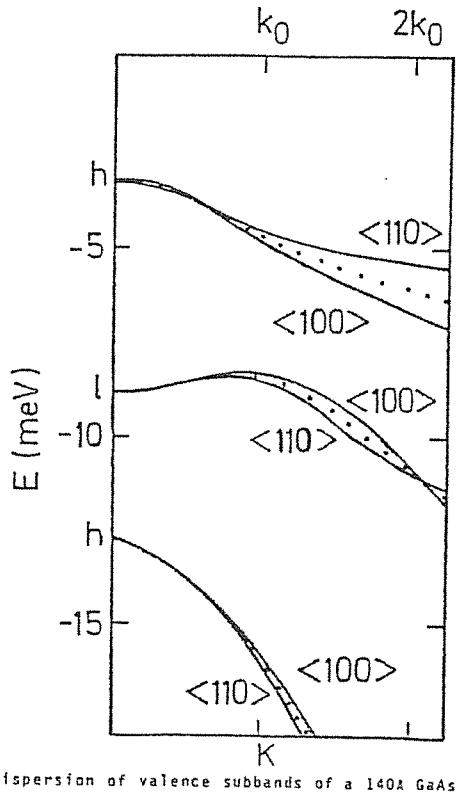

Dispersion of valence subbands of a 140Å GaAs - 200Å $Al_xGa_{1-x}As$ superlattice, with x = 0.21, in the plane perpendicular to the <001> growth axis. Solid lines: dispersion for $\vec{k}$ in the <100> or <110> directions. Dotted line: axial approximation. k_0 denotes $\pi/340Å = 9.24 \cdot 10^5$ cm^{-1}. h and l denote "heavy" or "light" character at $\vec{k} = 0$.

Figure 2.2:

It has been shown [33,34] that the coupling between HH and LH states via the Luttinger Hamiltonian matrix elements, together with the requirements imposed by the SL boundary conditions, results in strong non-parabolic dispersion of the subbands in the (k_x, k_y)-plane. For instance, in Fig.2.2 results for a 120 $\AA$ QW of GaAs sandwiched between $Al_{0.21}Ga_{0.79}As$ barriers are shown: they are obtained [35] in the many-band Envelope-Function model described previously. The calculation is done within the "axial model" in which [88] the parameters γ_2^L and γ_3^L in the matrix element C in Eq.(2.21) are replaced by the mean value $\overline{\gamma^L} = (\gamma_2^L + \gamma_3^L)/2$ [3]. With this

[3]The axial approximation becomes necessary in the presence of a magnetic field applied

replacement, the Hamiltonian (2.20) acquires cylindrical symmetry about the z-axis and the resulting bands are isotropic in the k_x, k_y plane. For comparison, the true dispersions for k in the $<100>$ and $<110>$ directions are also shown in Fig.2.2: the axial approximation is seen to represents a good average of them. The labels on the vertical axis of Fig.2.2 refer to the character of the solutions at $k_x = k_y = 0$, where there is no mixing of LH and HH components: the dispersion along k_z is purely parabolic, with effective masses

$$J_z = \pm 3/2 \quad : \qquad m^*_{HH} = (\gamma_1^L - 2\gamma_2^L)^{-1} = 0.377 \tag{2.22a}$$

$$J_z = \pm 1/2 \quad : \qquad m^*_{LH} = (\gamma_1^L + 2\gamma_2^L)^{-1} = 0.091 \tag{2.22b}$$

As soon as one moves out of the k = 0 axis, the mixing of these components grows rapidly, leading to strong deviations from parabolicity. Notice in particular the first LH subband that starts off with a positive (i.e. electron-like) mass. The anti-crossing behavior leads in addition to a HH mass in the first subband heavier than expected in the absence of mixing. The strong mixing at $k \neq 0$ and the consequent non-parabolicity were first pointed out in Ref. [33]. For a symmetry-based justification of the anti-crossing behavior in Superlattices, see Ref.[37].

We will see in Chapter 3 how these non-parabolicities lead to a complicate non-linear behavior of the Landau level structure when a magnetic field perpendicular to the interfaces is applied.

2.6 Effective Mass vs. Tight-binding Theories.

In the EM approximation the superlattice wavefunction is written as a linear combination of Brillouin zone-center bulk states, with a slowly varying envelope modulation along the SL-axis (see Eq.2.17). Although envelope-function calculations are found to be in very good overall agreement with experiments, there are specific situation where a more complete description is needed. This can occur when two or more bulk states with widely separated wave vectors contribute significantly to a given SL state. An example

along the z-direction: in such a case, as it will be explained in Section 3.2, it is possible to write an exact solution for the motion in the (x, y)-plane only within the axial model.

occurs in the SL subbands above the lowest conduction subband in the *GaAs/AlGaAs* SL. As the subband energies approach the GaAs X-point conduction band minimum (see the band structure in Fig.2.1a), the SL states become a mixture of Γ-point and X-point related bulk states. Since the Envelope Function method is based on a single k-point bulk states only (the Γ-point in the present case), this X-point contribution is omitted.

A second example can occur in SL valence bands. The Envelope-Function approximation allows no mixing of bulk Heavy Hole and Light Hole states in the SL wavefunction at the BZ-center (this is immediately apparent from the expression of the Hamiltonian (C.1) in Appendix C when $k_x = k_y = k_z = 0$). This approximation is realistic as long as the HH and LH states are sufficiently separated in energy. However, for certain layer thickness and barrier alloy concentration, they can be close to one another. For instance, in a GaAs QW between Al_x $Ga_{1-x}As$ barriers, with $x = 0.25$ and assuming that the valence band discontinuity is 40 % of the total band-gap discontinuity, a crossover between the first LH and the second HH subbands is expected when the GaAs layer thickness is about 280 $\AA$. This k = 0 mixing can have a substantial effect on optical and transport properties, since they depend mainly on the band structure near the zone-center.

A surprisingly large ($\sim$ 30 %) admixture of the LH states in the highest Heavy hole subband state in a 210 $\AA$ - *GaAs/AlGaAs* QW structure was found at k = 0 by investigating the polarization of the optical emission spectra [38]. Attempts to interpret these results within the Effective Mass approximation and coupling with Luttinger Hamiltonian yield quantitative disagreement: several other coupling mechanism (strains in the layers, electric fields, asymmetry in the Quantum Well), were found to be inadequate as well.

An alternative approach to the EM scheme consists in the use of empirical Tight-Binding (**TB**) models, in which the SL wavefunction is described as a linear combination of atomic-like orbitals. TB calculations have been performed on *InAs/GaSb* and *GaAs/AlGaAs* SL [39]: although in most cases the Γ-point states are found to be predominant, a certain admixture of other bulk states seems necessary in order to describe correctly the aforementioned particular situations. A drawback of TB methods is that they lead to big-sized problems when they are applied to thick SL's, since the dimension of the Hamiltonian matrix increases with the size of the repeated unit cell. Moreover, the implementation of self-consistent calculations when

charge transfer in the heterostructure is expected, is somewhat difficult in a TB approach.

Chapter 3

Hole-subband mixing in Quantum Wells: a magneto-optic study.

3.1 Introduction.

Many of the most revealing experiments on 2D systems are performed in an external magnetic field: the reason is that in a two-dimensional system - for instance electrons or holes in an isolated QW or in the binding potential at the interface of a doped heterojunction (Fig.1.5) - a perpendicular magnetic field fully quantizes the two available degrees of freedom, producing an entirely discrete spectrum and thus leading to an enrichment of optical structures and also to new transport phenomena, like for instance the Quantum Hall Effect [40,41,42].

In this Chapter we are concerned with the effect of mixing of the hole subbands on the magneto-optical interband transitions in Quantum Wells. The system investigated is a $GaAs/Al_xGa_{1-x}As$ QW in an external magnetic field applied along the $< 001 >$ growth axis. The inter-band transition energies and strengths for this system are calculated in Sect.3.4, within the six-band Envelope-Function approach described in Chapter 2, and the results of these calculations are compared in Sect.3.5 with available experimental data.

3.2 Effect of an external magnetic field.

One of the main advantages of the Envelope-Function method described in Chapter 2 is that it can be easily extended to include external fields. Here we shall discuss the effect of an external magnetic field applied perpendicularly to the layers constituting the heterostructure [34].

The field $\mathbf{B} = (0, 0, B)$ is described by the vector potential $\mathbf{A}$ (it is convenient to choose the gauge with $A_z = 0$). Thus in the six-bands $\mathbf{k} \cdot \mathbf{p}$ bulk Hamiltonian (C.1), $\mathbf{k}$ has to be replaced by $\mathbf{k}' = \mathbf{k} + (e/c)\mathbf{A}$. Since the components of $\mathbf{k}'$ doesn't commute:

$$[k'_x, k'_y] = -i(e/c)B \tag{3.1}$$

one must go back to the original Luttinger-Kohn Hamiltonian [32], written in term of the anticommutators $\{k_i, k_j\}$, to derive the correct expression when a magnetic field is present. Moreover, new diagonal terms arise, representing the direct coupling of the electron and hole to the field; the conduction band diagonal terms in the 6×6 Hamiltonian (C.1) now become:

$$H_{cc} = E_c + (\mathbf{k} + e\mathbf{A}/c)^2/2m^* + (e/2mc)g^* s_z B \tag{3.2}$$

where $\mathbf{s}$ is the electron spin ($s_z = \pm 1/2$) and the effective g-factor is written, following Roth et al. [27], as:

$$g^* = 2/m^* \tag{3.3}$$

For the valence band diagonal elements, one must add the terms:

$$(e/c)\kappa J_z B + (e/c)q J_z^3 B \tag{3.4}$$

where J_z is the spin 3/2 matrix operator and κ, q are two material parameters [30]. Actually q is very small for the semiconductors of interest here and will be set to zero.

As a consequence of (3.1), one can define conjugate operators a, a^+

$$a = (c/2eB)^{1/2}(k'_x - ik'_y) \qquad a^+ = (c/2eB)^{1/2}(k'_x + ik'_y) \tag{3.5}$$

obeying the commutation relation $[a, a^+] = 1$. Thus all terms in k_x, k_y in the Luttinger Hamiltonian can be expressed in terms of these harmonic oscillator raising and lowering operators.

It is possible to write a closed-form solution of the eigenvalue problem only if one takes the so-called axial approximation. In fact, the full Hamiltonian in the presence of a magnetic field can be written as[34]:

$$H = H_{ax} + H_{cub} \tag{3.6}$$

where [1]

$$H_{ax}= \begin{vmatrix} H_{11} & iP\sqrt{\frac{eB}{c}}a^+ & -iP\sqrt{\frac{eB}{3c}}a & 0 & -iP\sqrt{\frac{2}{3}}k_z & 0 \\ & H_{22} & \overline{\gamma}\sqrt{3}\frac{eB}{c}a^2 & 0 & \gamma_3\sqrt{\frac{6eB}{c}}k_z a & 0 \\ & & H_{33} & iP\sqrt{\frac{2}{3}}k_z & 0 & -\gamma_3\sqrt{\frac{6eB}{c}}k_z a \\ & & & H_{44} & iP\sqrt{\frac{eB}{3c}}a^+ & -iP\sqrt{\frac{eB}{c}}a \\ & & & & H_{55} & \overline{\gamma}\sqrt{3}\frac{eB}{c}a^2 \\ & & & & & H_{66} \end{vmatrix} \tag{3.7}$$

$$H_{11} = H_{44} = E_c + (eB/m_{so}c)(a^+a + 1) + k_z^2/2m_{so}$$
$$H_{22} = E_v - (\gamma_1/2 - \gamma_2)k_z^2 - (eB/c)[(\gamma_1 + \gamma_2)(a^+a + 1/2) + 3\kappa/2]$$
$$H_{33} = E_v - (\gamma_1/2 + \gamma_2)k_z^2 - (eB/c)[(\gamma_1 - \gamma_2)(a^+a + 1/2) - \kappa/2]$$
$$H_{55} = E_v - (\gamma_1/2 + \gamma_2)k_z^2 - (eB/c)[(\gamma_1 - \gamma_2)(a^+a + 1/2) + \kappa/2]$$
$$H_{66} = E_v - (\gamma_1/2 - \gamma_2)k_z^2 - (eB/c)[(\gamma_1 + \gamma_2)(a^+a + 1/2) - 3\kappa/2]$$

and the lower half of the matrix is obtained by Hermitean conjugation [2]. In (3.7) $\overline{\gamma} = (\gamma_2 + \gamma_3)/2$, E_c and E_v are the conduction and valence band-edge energies, B is the magnetic field strength, a and a^+ are the harmonic oscillator raising and lowering operators (3.5); five band parameters $P \equiv -i < s|p_x|x >$, γ_1, γ_2, γ_3 and κ appear in this matrix, describing electron and hole effective masses and g-factors (see Sect. 2.4). The effective mass $m_{so}^{-1} = 1 + 2P^2/3(E_g + \Delta)$ appearing in the electron terms H_{11} and H_{44} takes into account indirectly the coupling to the split-off (J=1/2) band [27], E_g and Δ being, respectively, the energy gap and the spin-orbit splitting at k=0.

[1] atomic units are used here and throughout this Chapter.

[2] Additional terms that come from the lack of inversion symmetry in zinc-blend semiconductors [26] are neglected, as usual.

The term H_{cub} has the form:

$$H_{cub} = \begin{pmatrix} H_a & 0 \\ 0 & H_a \end{pmatrix} \tag{3.8}$$

where

$$H_a = \frac{\sqrt{3}eB}{2c}(\gamma_2 - \gamma_3) \begin{pmatrix} 0 & 0 & 0 \\ 0 & 0 & a^{+2} \\ 0 & a^2 & 0 \end{pmatrix}$$

Inclusion of this term, which accounts for the anisotropy of the hole dispersion in the (k_x, k_y)-plane, uncrosses some of the Landau levels, namely those differing in the Landau index n by ± 4, but the absolute shifts are always less than 10% [43,44]. We will then assume $H_{cub} = 0$.

The H_{ax} term in (3.6), which neglects the anisotropy in the (k_x, k_y)-plane, can be solved exactly. In this case the solution of the Effective Mass equation in each of the A and B materials constituting the SL takes the form [34,32]:

$$F_n = (c_1(z)\phi_n, c_2(z)\phi_{n-1}, c_3(z)\phi_{n+1}, c_4(z)\phi_{n+1}, c_5(z)\phi_n, c_6(z)\phi_{n+2}) \tag{3.9}$$

where $\phi_n(x, y)$ are harmonic oscillator wavefunctions with $n = -2, -1, 0, \ldots$ and the $c_j(z)$ coefficients are automatically vanishing for the components with negative oscillator index.

The total zeroth-order wavefunction is (see (2.17)):

$$\Psi_n = \sum_{j=1}^{6} F_n^j u_j \tag{3.10}$$

where u_j is the periodic part of the j-th host Bloch function. The set of functions u_i used is given explicitly in (2.15). These functions are assumed to be identical in A and B layers, in the spirit of the Envelope Function approach (see Sect.2.3).

With the replacement $k_z = -i\partial/\partial z$ in the Hamiltonian (3.6), the Effective Mass equations $\sum_{j'} H_{jj'}F_{j'} = EF_j$ become a system of differential equations for the envelope functions $c_j(z)$. Writing the effective Hamiltonian (3.6) in the form $H_{jj'} = (D^z_{jj'}k_z^2 + E_j)\delta_{jj'} + (P^z_{jj'} + A_{jj'}(n, B))k_z + C_{jj'}(n, B)$, the appropriate boundary conditions are written as [34]:

$$-iD^{zz}_{jj}\partial c_j(z)/\partial z + (1/2)\sum_{j'} A_{jj'}c_{j'}(z) \quad \textit{continuous} \quad (j = 1, ..., 6) \tag{3.11}$$

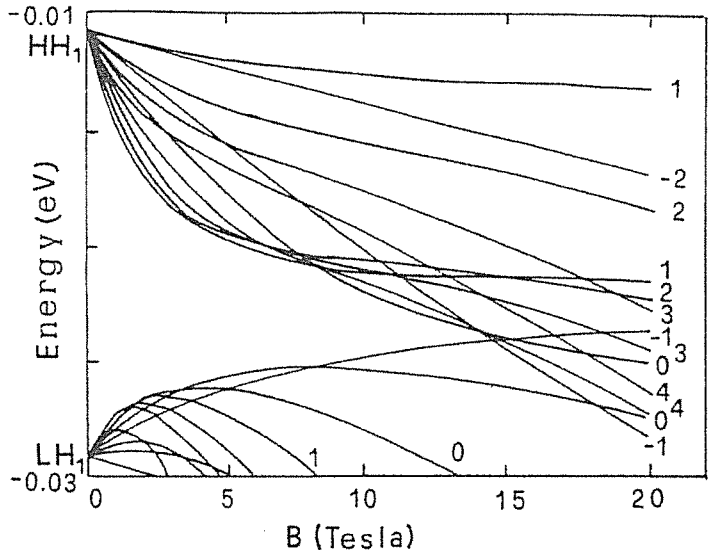

Figure 3.1:
Calculated Landau levels for the first two hole subbands in a 78 $\AA$ GaAs QW between 160 $\AA$ $Al_{0.3}Ga_{0.7}As$ barriers. The numbers are the Landau level indices n.

For the superlattice case, all six $c_j(z)$ functions have the common pre-factor $exp(ik_{sz}z)$, where k_{sz} is the quasi-momentum in the SL-Brillouin zone. For SL with very thick barriers (QW limit), the latter dependence is very small and can be neglected.

3.3 Landau levels in a Quantum Well.

Using the formalism described in Sect.3.2, we have calculated hole and electron Landau Levels (LL) for the case of a 78 Å-QW between $Al_{0.3}Ga_{0.7}As$ barriers. The results of such calculation are shown in Fig.3.1 and Fig.3.2 (the zero of energy is taken at the top of the GaAs valence band). They are obtained using a 60/40% rule for the band-offset (i.e. the conduction band discontinuity ΔE_c in Fig.1.9 is 60 % of the total band-gap difference). The material parameters used in the Hamiltonian (3.7) are listed in Table II, in Sect.2.4.

The most remarkable feature of the calculated hole LL displayed in Fig.3.1 is their strong non-linear dependence on the magnetic field [34]: at $B \neq 0$, LL originating from the first HH subband interact with those from the next subbands giving rise to anti-crossing behavior. In particular, the initial electron-

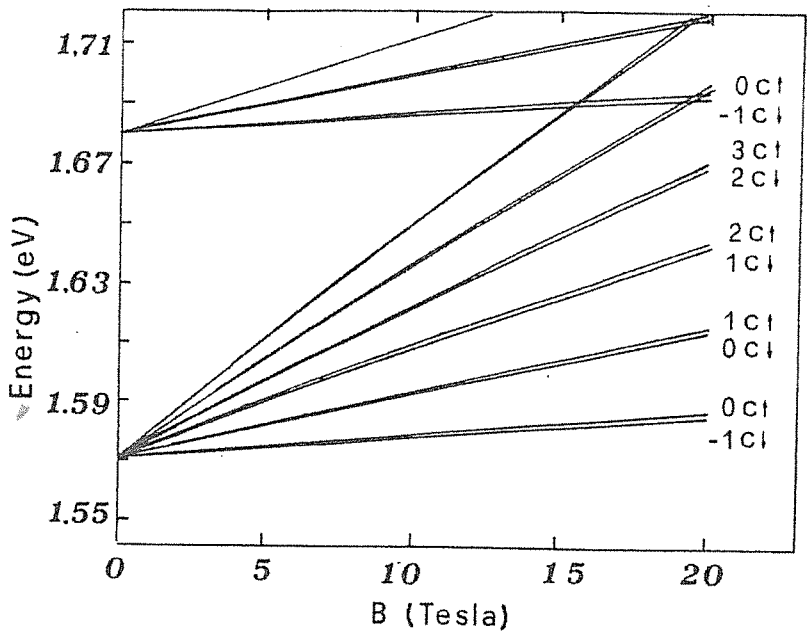

Figure 3.2:
Calculated Landau levels for the first two electron subbands. The two spin-splitted states are indicated for each level.

like dispersion of LL emerging from the LH_1 subband is mainly due to the interaction between LH_1 and the HH_2 subband, as explained in Appendix E. It is evident that this Landau level structure can no longer be described in terms of one effective mass per subband.

The Landau levels for the conduction subbands shown in Fig.3.2 are much more regular with respect to the ones derived for holes, displaying a simple "Landau ladder" form (note that a scale of energy different from Fig.3.1 has been used): at high fields slight deviations from a linear behavior occur, especially for large n ; in particular, the separation between successive levels, at a fixed value of B, decreases with increasing n. These effects, as it is well known, must be ascribed to non-parabolicity in the conduction band due to the coupling with valence band states. In fact, the energy of the electron levels - measured from the conduction subband edges at $B = 0$ - can be approximated as well by the following expression [45] (where the small spin-splitting terms are neglected) :

$$E_n = E(n, B, k_z)\left[1 + \frac{K_2}{E_g}E(n, B, k_z)\right] \qquad (3.12)$$

where $E(n,B,k_z) \equiv \omega_c^*(n+1/2)+k_z^2/2m^*$, $\omega_c^* = eB/m^*$ is the cyclotron energy, n is the LL index and m^* is the electron band-edge mass in the QW material. The non-parabolicity parameter K_2 is given, from four-band $\mathbf{k}\cdot\mathbf{p}$ theory, by [46]:

$$K_2 = -\frac{(1-m^*)^2 E_g(3E_g+4\Delta+2\Delta^2/E_g)}{(E_g+\Delta)(3E_g+2\Delta)} \tag{3.13}$$

For GaAs, one obtains $K_2 = -0.83$, using in (3.13) the value $m^* = 0.067$ for the effective mass [47]. It can be seen from Eq.(3.12) that non-parabolic effects are more important for high values of $E(n,B,k_z)$, as found in quantum wells due to the confinement energy.

In Ref.[48] magneto-optical data in GaAs QW's are fitted using (3.12) to describe the electron levels, with $m^* = 0.067$ but using the value $K_2 = -1.2$. This is an indication that the conduction band non-parabolicity is enhanced with respect to the values predicted by simple models. We will come back to this point at the end of Sect.3.5.

3.4 Interband optical transitions: matrix elements and selection rules.

Let's consider the process in which a photon is absorbed and an electron is raised from a valence band LL to a conduction band one. We indicate with $|\Psi_n^I>$ and $|\Psi_{n'}^F>$, respectively, the Initial (valence) and Final (conduction) states with Landau index n, n' defined in (3.10), whose envelope terms F_n^j depend implicitly on the magnetic field; the matrix elements for direct optical transitions are given by:

$$M_{n,n'} = <\Psi_n^I|\mathbf{p}\cdot\epsilon|\Psi_{n'}^F> = \sum_{i,j=1}^{6} <u_i|\mathbf{p}\cdot\epsilon|u_j><F_n^i|F_{n'}^j> + \sum_{i,j=1}^{6}\epsilon\cdot<F_n^i|\mathbf{p}|F_{n'}^j>\delta_{ij} \tag{3.14}$$

ϵ being a unit vector in the direction of the electric field of the incident radiation. We use here the compact notation :

$$<u_i|(..)|u_j> \equiv \int_{cell} u_i^*(\mathbf{r})(..)u_j(\mathbf{r})d\mathbf{r}\,; \quad <F_n^i|(..)|F_{n'}^j> \equiv \int_{crystal} F_n^{i\,*}(\mathbf{r})(..)F_{n'}^j(\mathbf{r})d\mathbf{r} \tag{3.15}$$

The first term on the right hand side of (3.14) gives the allowed interband transition matrix elements [50]. The second term, which gives the strength of the intraband transitions analogous to those observed in Cyclotron Resonance and whose explicit expression is given in Appendix F, involves essentially the overlap between the same components of the wavefunction (3.9) for the two states I and F; for this reason, it is expected to contribute also to the interband transition strengths in type II superlattice-systems like InAs/GaSb, where the conduction band states of one material are strongly mixed with the valence band states of the other , as a consequence of the peculiar band line-up of the InAs/GaSb heterojunction [13]. In the present case we neglect this term since it gives a contribution to $|M_{n,n'}|^2$ which is typically $1-2\%$ of that given by the first term.

The intensity of an inter-Landau level transition between the states I and F is thus proportional to the squared matrix element:

$$\begin{aligned} |M_{n,n'}|^2 &= \Big|\sum_{i,j=1}^{6} < u_i|\mathbf{p}\cdot\epsilon|u_j > \int c_i^*(z)c_j(z)dz \int \phi^*_{m_i}\phi_{m'_j}d\mathbf{r}\Big|^2 \\ &= \Big|\sum_{i,j=1}^{6} (\mathbf{p}\cdot\epsilon)_{ij} \int c_i^*(z)c_j(z)dz\, \delta_{m_i,m'_j}\Big|^2 \qquad (3.16) \end{aligned}$$

m_i,m'_j are the i-th and j-th component of the vectors $m = (n, n-1, n+1, n+1, n, n+2)$ and $m' = (n', n'-1, n'+1, n'+1, n', n'+2)$ respectively [3].

Since the only matrix elements $(\mathbf{p}\cdot\epsilon)_{ij}$ different from zero, for circularly polarized light and in the Faraday configuration (see Footnote 4), are

$$\begin{aligned} |(\mathbf{p}\cdot\epsilon)_{12}| = P/\sqrt{2} = |(\mathbf{p}\cdot\epsilon)_{46}| = \sqrt{3}|(\mathbf{p}\cdot\epsilon)_{13}| \\ |(\mathbf{p}\cdot\epsilon)_{45}| = |(\mathbf{p}\cdot\epsilon)_{13}| \qquad (3.17) \end{aligned}$$

(P being the Kane momentum matrix element appearing in (3.7)), one sees by inspection that the selection rule $n' - n = \pm 1$, must be satisfied, the plus (minus) sign referring to right (left)-handed circular polarization (hereafter σ^+ and σ^-).

[3]The matrix elements (3.16) for optical transitions in a magnetic field are proportional to the absorption coefficient. At zero field the evaluation of the absorption coefficient involves an integration over the in-plane momentum $k\|\equiv(k_x, k_y)$, whereas in a magnetic field the Landau levels are degenerate and the integration over $k\|$ reduces to a factor which expresses such degeneracy.

TABLE III

Components of the Landau-level wavefunction (see Eq.(3.9) in the text) involved in the optical transitions for the two different circular polarization.

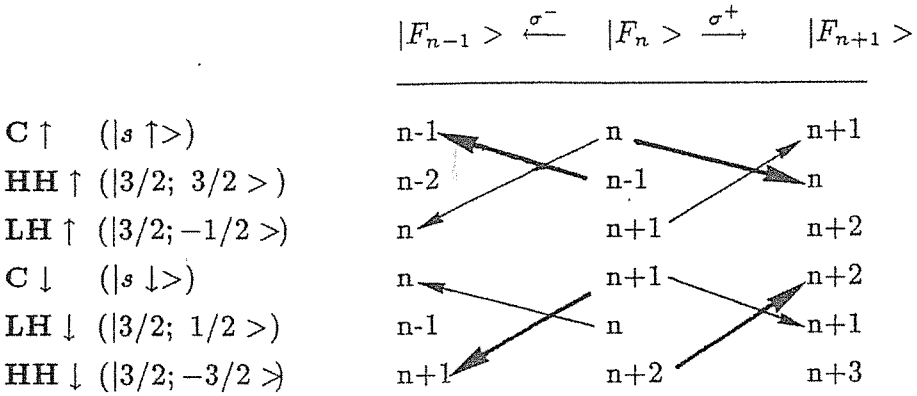

According to (3.17), we show in Table III how the various components of the wavefunction (3.9) are involved in the transitions $|F_n> \longrightarrow |F_{n\pm1}>$ for the two different polarizations σ^+ and σ^-, the arrows connecting the pairs of components which contribute to the overlap integral in (3.16): σ^+ corresponds to $\Delta m_J = +1$ and σ^- to $\Delta m_J = -1$, where m_J is the total angular momentum quantum number. A shorthand notation for the $|J; m_J>$ basis states (2.15) is introduced, as shown in the left part of Table III.
Note that the oscillator strength of an HH component is three times bigger than the LH one, as a consequence of the particular form of the atomic-like dipoles (3.17) associated with the basis set chosen (this is represented by the thicker lines in Table III): transitions from HH Landau levels are thus expected to be more intense than those involving LH levels. Pairs connected by down-pointing arrows are expected to give a negligible contribution to (3.16) since the conduction [valence] band components in a valence [conduction] state are always very small ($1 - 3\%$). We stress the fact that in a simple scheme which uses only the selection rule $\Delta n = \pm 1$ for the total wavefunction to determine the allowed transitions between Landau levels, far more transitions are predicted than experimentally observed [49], because the mixing between LH and HH hole subbands, together with the restrictions imposed by Table III, make many of the allowed transitions have small matrix elements. Moreover, the mixing makes the transition intensities strongly field-dependent: the resulting picture

of magneto-optical transitions is thus neither simple nor obvious. In addition, even transitions that satisfy the restrictions of Table III can still have vanishing matrix elements due to the different parity of the envelope-functions $c_j(z)$ of the initial and final state involved.

Thus the explicit evaluation of the dipole matrix elements (3.16) is an essential ingredient in any attempt to make a comparison between theory and experiment. Postponing this comparison to Sec.3.5, we discuss now briefly simple symmetry properties of the envelope functions $c_j(z)$ appearing in the overlap integrals in (3.16).

Every $c_j(z)$ in the envelope function (3.9) is a solution of a 1×1 effective Hamiltonian H_{eff}, obtained by projecting the Hamiltonian (3.7) onto the j-th edge. It can be shown that H_{eff}, if flat-band conditions prevail, contains only even powers of $k_z \equiv -i\partial/\partial z$ [51]: thus every $c_j(z)$ can be either even or odd with respect to the reflection $z \rightarrow -z$ in one of the mirror (x,y)-planes bisecting the QW layer. In particular the $HH\uparrow$ state is coupled, in the matrix (3.7), with the $LH\downarrow$ state by a term proportional to k_z, and to $LH\uparrow$ by a term independent of k_z (see the left column of Table III for the notation). As k_z is odd under the reflection with respect to the mirror planes, an even $HH\uparrow$ component will be coupled with an odd $LH\downarrow$ and an even $LH\uparrow$, and vice versa. A similar argument applies to the coupling between $HH\downarrow$,$LH\uparrow$ and $LH\downarrow$ states.

To illustrate this point, we show in Fig.3.3 the z-dependence of the squared amplitudes $|c_j(z)|^2$ for each of the hole components ($j = 2,3,5,6$) of the envelope function (3.9) for the highest (in energy) four hole Landau levels with n=1 at B=10 Tesla, in a 78 Å QW. The strong admixture between the HH and LH components is clearly visible in the LL_2, LL_3, LL_4 states : only the highest LL_1 state displays a dominant $HH\uparrow$ character. As anticipated, $HH\uparrow$ [$HH\downarrow$] and $LH\downarrow$ [$LH\uparrow$] states are mixed with opposite parity. The total wavefunction, not shown, doesn't exhibit any particular reflection symmetry.

It is worth noting that the mixing between LH and HH Landau levels at finite fields leads, as we shall see in the following, to the violation of the usual selection rule $\Delta m = even\ integer$, m and $m\prime$ being the subband indices of the valence (HH or LH) and conduction (C) states involved in the transition. Even at B=0 transitions between subbands of different parity are equally allowed, due to valence-band hybridization at finite $k||$ [52] (such transitions, as the one between HH_2 and C_1 subbands, have also experimentally been observed, see

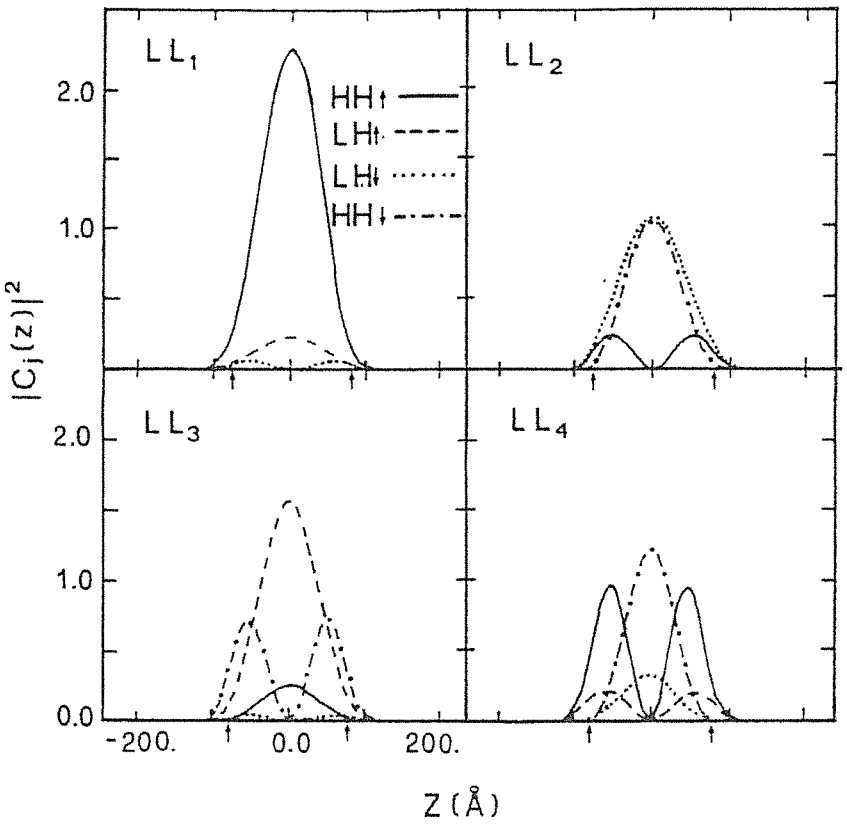

Figure 3.3:
Squared amplitudes associated with the four components (indicated in the first panel) of the envelope-functions for the four highest valence states with Landau index n=1, at B=10 Tesla. The levels are labelled with LL_1, LL_2, LL_3 and LL_4, in order of decreasing energy. The arrows show where the GaAs/AlGaAs interface is located.

Ref.[53]) [4].

In the following we will focus on the behavior of interband transitions at moderately high magnetic fields which, for the range of energy of interest here, result from Landau levels of index $n \lesssim 10$. These states derive at $B \simeq 0$ from the region of subband structure around $k|| = 0$. Hence *for these levels* the limit $B \to 0$ is equivalent to the limit $k|| \to 0$, where the HH and LH components are decoupled: this should be kept in mind especially when reading Sec.3.5. The full coupling provided by the off-diagonal elements in the Luttinger matrix Hamiltonian (3.7) would be present at $B \sim 0$ in Landau levels with high oscillator index, i.e. those resulting from states of finite $k||$: in particular, valence-to-conduction band transitions from high-n Landau levels originating from subbands of different parity would have finite dipole matrix elements at $B \simeq 0$ and the results of Ref.[52] would be recovered.

3.5 Comparison with the experiments.

We make in the following a comparison of theoretical calculations for the energies and strengths of magneto-optical inter-band transitions with the results of excitation spectroscopy experiments performed in a nominally 90 Å GaAs-Quantum Well [54] clad between thick $Al_{0.3}Ga_{0.7}As$ layers, at high field (up to 20 Tesla) and at very low temperature, in the Faraday configuration [55] [5].

An important input parameter in the calculation is the conduction band discontinuity $Q_c = \Delta E_c/(E_g^{AlGaAs} - E_g^{GaAs})$ (see Sect.1.4). We have estimated this quantity by fitting the energy of the observed peaks at $B = 0$ [56] as follows. The calculated dependence of the corresponding transition energies on Q_c is shown in Fig.3.4, with solid lines. The arrows drawn on the left side indicate the experimental observed values, corrected for the binding energies of the excitons: we used for these latter quantities the theoretical values quoted in Ref.[57], obtained with a variational method (they range from ~ 6 meV for the binding energy of the $HH_1 - C_1$ exciton to ~ 10 meV for the $LH_1 - C_1$). We

[4] The correspondence between $k||$ dispersion at B=0 and Landau-level behaviour can be easily understood by noting that, in the limit of high oscillator quantum numbers, the Landau levels of a subband $E(k_y)$ are given by $E_n(B) \simeq E(k_y = \sqrt{2eBn/c})$, $n \gg 1$.

[5] In the Faraday configuration both the incident and emitted radiation propagate at right angles with respect to the layer planes and parallel to the magnetic field axis: the exciting light is circularly polarized with respect to the magnetic field direction.

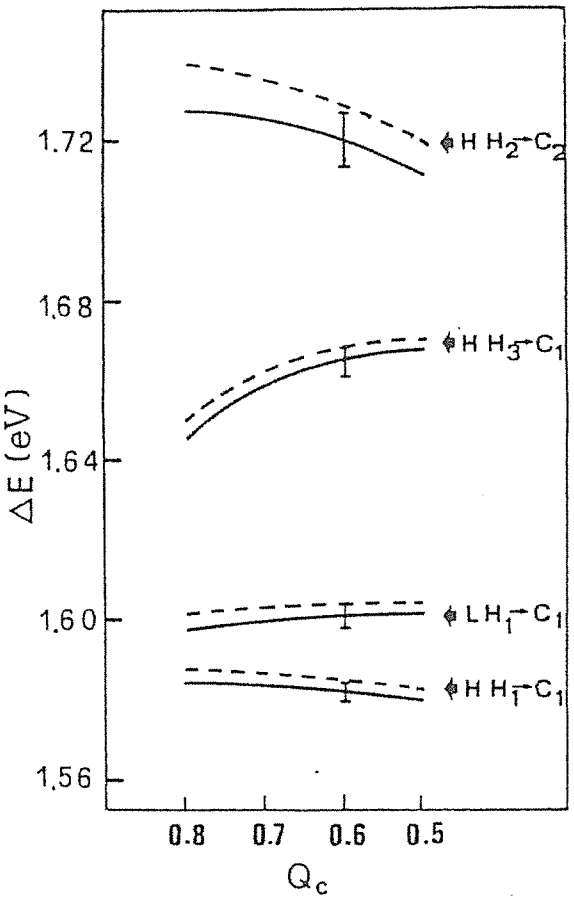

Figure 3.4:
Calculated dependence of the transition energies at B=0 on the conduction band discontinuity $Q_c \equiv \Delta E_c/\Delta E_g$. Solid lines are obtained with an electron mass $m^* = 0.074$, dashed lines with $m^* = 0.067$ (see text). The observed transitions, corrected for the binding energies of the excitons as explained in the text, are indicated by arrows. The bars drawn at $Q_c = 0.6$ account for a possible uncertainty of $\pm 2\,\AA$ in the well width.

found that the best fit to experimental points is obtained assuming $Q_c \simeq 0.6$ (the bars drawn on the curves at this value, account for a possible uncertainty of $\pm 2\AA$ on the GaAs well thickness): this estimate is close to the recent and perhaps most accurate determinations of this parameter for the GaAs/AlGaAs system, $Q_c = 0.69 \pm 0.03$ [21] (see Sect.1.4).

In Fig.3.5 we show the calculated interband transition energies for both the polarizations of incident light, with intensities obtained from the transition matrix elements (3.16)[59] vs. magnetic field B. They are obtained using in the matrix (3.7) band structure parameters that correctly reproduce the GaAs and GaAlAs bulk data (see Table II). We adopt for convenience, from now on, the following convention to label transitions: the numbers indicate the Landau level indices n of the initial and final level, while the letters refer to the character of the subband at $B = 0$; the subscript m is the subband index . The two spin-splitted hole levels, for every Landau index n, will be identified (when necessary) by giving in parenthesis the spin character at $B \simeq 0$, where the HH and LH mixing (for the low-n levels of interest here) is small.

We normalize intensities to the most intense transition, which turns out to be the $-2HH_1(\downarrow) \rightarrow -1C_1(\downarrow)$ in our notation (first line from below in the σ^+ spectrum of Fig.3.5a,b), and plot only those which are at least 5% of that one. Solid lines represent transitions with a calculated intensity between 1.0 and 0.4, dashed lines represent those between 0.4 and 0.05. With dotted lines we indicate transitions which are smaller than 5% at some fields but acquire intensity through the admixture with other states with increasing magnetic field. In particular, this is true for transitions between low-index LL deriving from the HH_2 and C_1 edges, which are parity forbidden at $B = 0$, but acquire intensity through the admixture with LH states with opposite parity at higher values of the magnetic field.

Many interesting features, that are not obvious on the basis of the calculated Landau levels only, are emphasized by the present calculation. For instance, the admixture between LH and HH hole-states in Landau levels with $n \geq 0$ leads, at fields above 10 Tesla, to a change of slope of the transition lines involving these levels, making them less steep at higher fields where they recover in part the LH character (which, because of the particular asymmetry in the diagonal elements of the Luttinger Hamiltonian [32], has a heavier mass in the (k_x, k_y) plane). One important consequence is that the the zero-field exciton binding energy in QW's, obtained by extrapolation at $B = 0$ of high field data as the difference in energy between the ground state and the continuum states, may in some cases give an

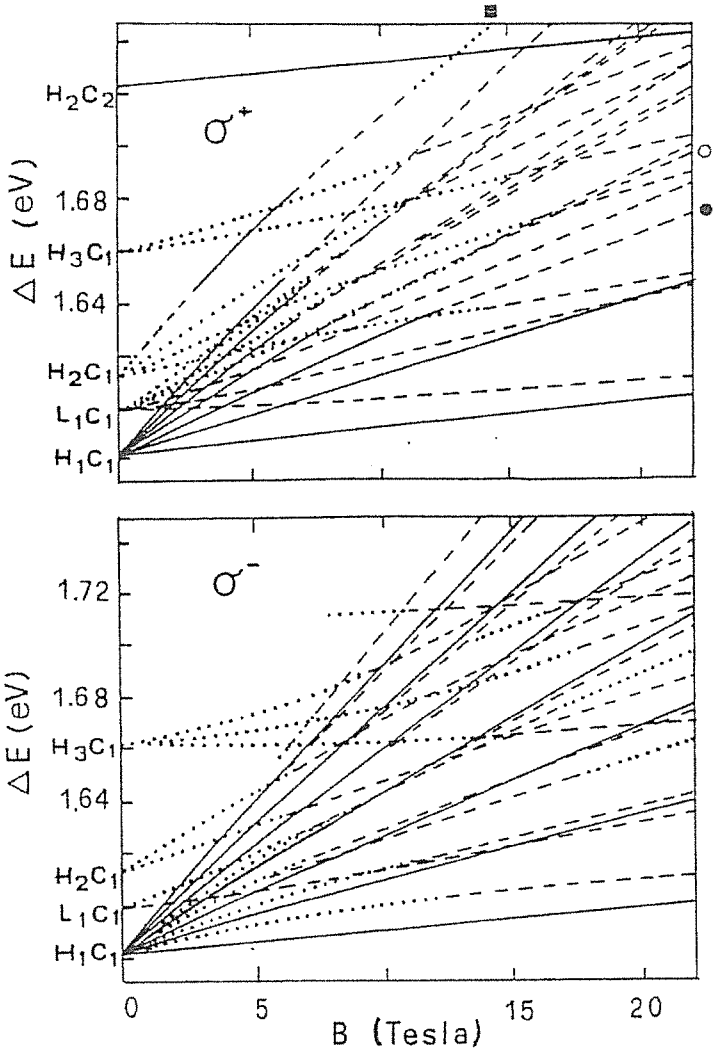

Figure 3.5:
Calculated transition energies for the two circular polarizations, as a function of the magnetic field B. Intensities are normalized to the lowest $HH_1 - C_1$ transition and are represented by :
dotted lines : intensity less than 0.05
dashed lines : between 0.05 and 0.4
solid lines : between 0.4 and 1.
The full and empty circles and the square identify the transition lines of Fig.3.6 and 3.7 respectively (see the text).

overestimated value for the binding energy: in fact the experimental values for this quantity, derived in the above manner [49], are systematically higher than the theoretical ones [60,66].

Note that, for the σ^- spectrum, the transitions associated with Landau levels that evolve from the zero-field $HH_1 - C_1$ edge are always stronger than those involving LH states. The more or less regular, equidistant Landau level-like features can in fact be recognized both in the experiment and the calculation. This statement is definitely not true in the more complicated σ^+ spectrum.

As an example of the effect of hole mixing on the transition strengths, we report in Fig.3.6 the calculated intensities of the $0HH_1(\downarrow) \rightarrow 1C_1(\downarrow)$ transition - curve (a) - and of the $0LH_1(\downarrow) \rightarrow 1C_1(\downarrow)$ transition - curve (b) -, as a function of the magnetic field B. (In Fig.3.5 the corresponding transition lines are identified with a full and empty circle, respectively). On the top of the figure we show, as functions of B, the relative weights of the hole components entering into the envelope-function (3.9) of the hole Landau level. The $0LH_1(\downarrow)$ and $0HH_1(\downarrow)$ levels are both visible in Fig.3.1, the $0LH_1(\downarrow)$ being the one which crosses the B-axis at about 13 Tesla. Their anti-crossing behavior is easily understood by recalling that the HH_1 subband has a parallel mass (i.e. the mass in the (k_x, k_y) plane) lighter than the LH_1 subband: the splitting of the would-be crossing levels arises from the off-diagonal terms in (3.7), with a resulting heavy mixing of the $m_J = \pm 3/2$ and $m_J = \pm 1/2$ character.

At zero field the transition (b) is forbidden, in σ^+ polarization, by the conservation of the total angular momentum since for this transition $\Delta m_J = -1$, (see Table III and the related discussion in Sect.3.4) but at $B \neq 0$ it acquires intensity through the admixture of the hole level with an $HH \downarrow$ component. At $B \gtrsim 15$ Tesla the intensity decreases again due to an increase of an $LH \uparrow$ component. On the other hand, the transition (a), which is allowed at $B = 0$, becomes less intense at higher fields due to the increasing mixing with the $LH \downarrow$ component. For comparison, we report with dashed lines the intensities of the corresponding transitions in *bulk*-GaAs: it is evident the strong field-dependence of the transition lines in the QW case.

A similar analysis (see Fig.3.7) is performed on the $3HH_2(\downarrow) \rightarrow 4C_1(\uparrow)$ transition, which is parity forbidden at $B = 0$ (the corresponding line is identified with a square in Fig.3.5): at $B \neq 0$ it grows in intensity as the mixing of the odd $HH \downarrow$ state with an $LH \uparrow$ component of the opposite parity makes a non-vanishing overlap with the even C state in the matrix element (3.16). At fields higher than 8 Tesla, a "forbidden" $HH \uparrow$ component is picked up, making the

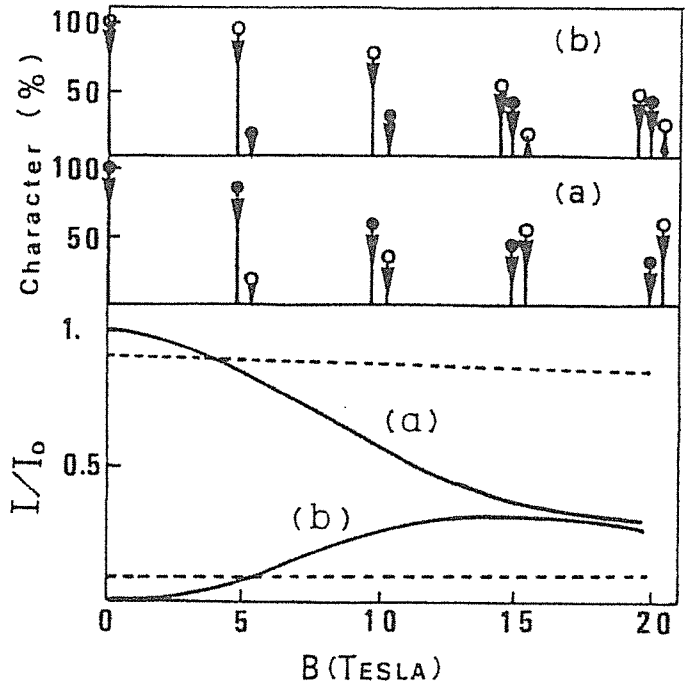

Figure 3.6:
Normalized intensities of the transition $0HH_1(\downarrow) \rightarrow 1C_1(\downarrow)$ (curve (a)) and $0LH_1(\downarrow) \rightarrow 1C_1(\downarrow)$ (curve (b)) as a function of the magnetic field B (in Fig.3.5 the corresponding transition lines are identified with a full and empty circle, respectively).
In the upper part of the Figure the weight of the various hole components in the envelope-functions (3.9) are shown for different values of B: full and empty circles correspond respectively to Heavy and Light states while up and down-pointing arrows identify the spin states. For comparison, the intensities of the corresponding transitions in *bulk*-GaAs are shown with dashed lines.

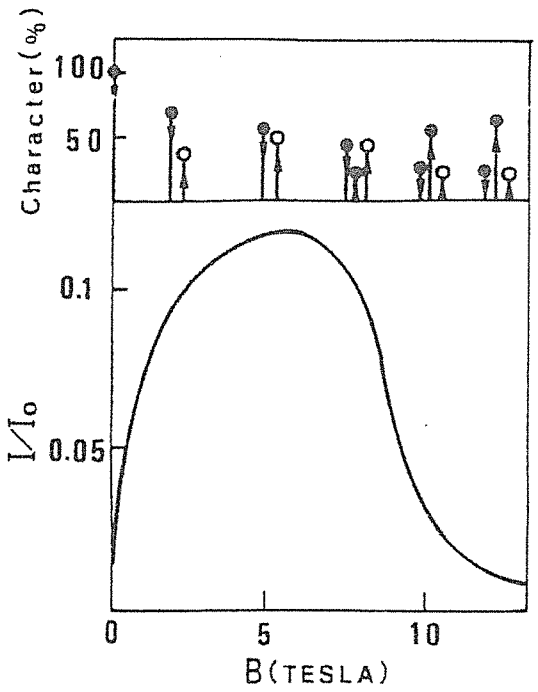

Figure 3.7:
Same as in Fig.3.6, for the $3HH_2(\downarrow) \rightarrow 4C_1(\uparrow)$ transition.

intensity vanish again.

In Fig.3.8, the calculated intensities *vs.* magnetic field for the same two transitions of Fig.3.6 are shown, for three different values of the QW width. For the narrow well case the coupling between the two states starts to be effective at high fields, due to the marked difference in the confinement energies of the two holes: the intensities are thus slowly varying with the field and in particular the transition from the upper HH_1 level (the one which is allowed at B=0) shows a closer resemblance to the corresponding bulk transition line (upper dashed line in figure). On the other hand, for the thick well case, the mixing takes place at much lower fields, the upper level thus acquiring a dominant $LH \downarrow$ character that makes the intensity decrease abruptly towards the corresponding bulk value (lower dashed line): in particular, this level becomes nearly flat after $\sim$ 5 Tesla, due to the anti-crossing behavior with the lower Landau levels, displaying only a very weak dependence on the magnetic field. The partner transition from the lower LH_1 level (thin line), after an initial increasing of strength due to the interchange of character between the two LL, is also depressed after $\sim$ 5 Tesla because of a strong mixing with a third "forbidden" $LH \uparrow$ component.

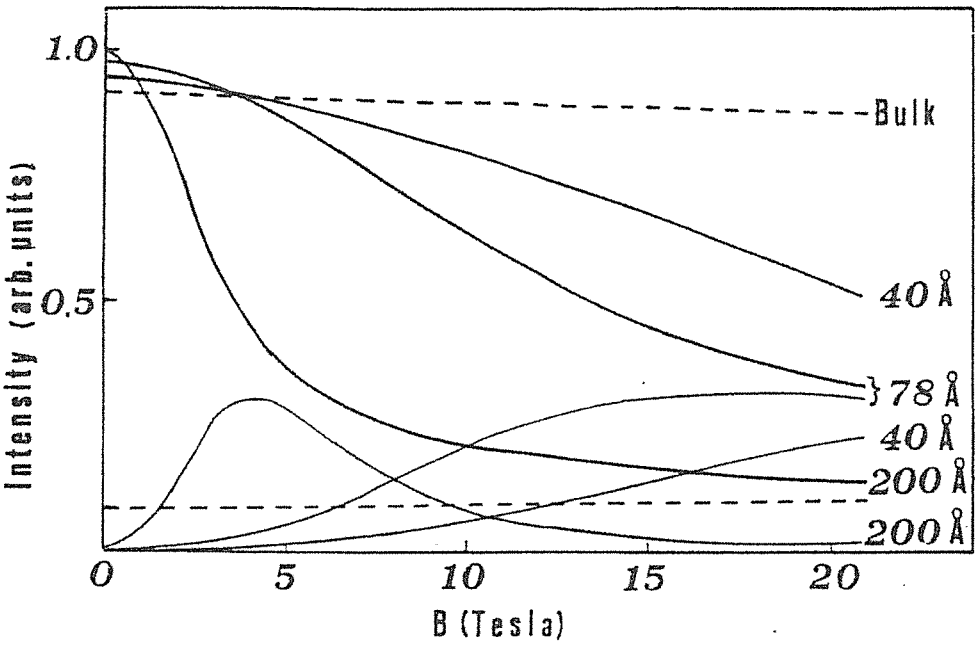

Figure 3.8:
Intensity *vs.* magnetic fields plot for the two transitions of Fig.3.6, for three different values of the QW width (solid lines) and for the bulk (dashed lines).

We compare next the outcome of our calculation, summarized in Fig.3.5, with available magneto-optical experimental data. Before doing this comparison, we correct the results of Fig.3.5 for excitonic effects, in the same way as done in Ref.[48]. The structure of the magneto-optical spectra in GaAs QW has been interpreted by several authors [49,55,61] in terms of transitions between free-carrier Landau levels, of which only the lowest is affected by excitonic effects. This is known, however, not to be the case in bulk-GaAs in which Coulomb binding is appreciable at high fields even in the higher levels [62]: in a Quantum Well, due to the enhanced binding energy of excitons (see Appendix G), the Coulomb interaction between electron and holes is expected to play a major role in the interpretation of magneto-optical spectra.

In the theory of simple-bands excitons in highly anisotropic systems in an external magnetic field described in Ref.[68], the high-field correction to the free Landau level energy due to Coulomb interaction is written as (see also Appendix G):

$$E_B = 3Ry^* D_1 \left(\frac{eB}{2(2n'+1)\mu Ry^*} \right)^{1/2}, \quad n' = 0, 1, 2, \ldots \tag{3.18}$$

In the above formula μ is the exciton reduced mass, Ry^* is an effective Rydberg $Ry^* = \mu e^4/2\epsilon^2$ (ϵ being the dielectric constant of the QW material) and D_1 is a parameter related to the dimensionality of the exciton ($D_1 = 1/4$ in the $3D$ case, while $D_1 = 1$ for a strictly $2D$ exciton) [6].

We subtracted the binding energy (3.18) from the calculated Landau level transition energies of Fig.3.5, taking $n' = 0$ for the lowest line in each of the fans emerging from the zero-field edges in Fig.3.5, $n' = 1$ for the next, and so on. The best overall agreement with experimental points is obtained with $D_1 \simeq 0.5$. Formula (3.18) applies in the limit of high fields: a rough estimate of its domain of validity is given by the criterion $\gamma > 1$, where γ is the reduced magnetic field $\gamma = \omega_c^*/2Ry^*$; taking $\mu^{-1} = 1/m^* + \gamma_1$ [24], one finds $B \gtrsim 6$ Tesla.

It must be remarked that the expression (3.18) is derived in the case of simple parabolic bands and thus should not be taken too seriously in the present context: a realistic calculation of exciton binding energies in Quantum Wells should include at the beginning the coupling between Heavy and Light holes [43,63,65].

We then identify the transitions in Fig.3.5 with the corresponding ones in the experimental results: this comparison shows that we could assign every experimental transition to a calculated one, but that consistently *all* theoretical ones were too steep, clearly indicating a too small electron mass. We found that an increase of the electron effective mass at the band-edge by ~ 11 % is necessary to give the correct slopes of the transition lines.

The results of our calculation are reported in Fig.3.9 (excitonic corrections included) together with the observed spectra, for $B > 6$ Tesla. Although the transitions have the right slope, few of them have absolute energy slightly different from the observed ones (typically deviations of $2 \div 5$ meV are encountered). However the strongest lines, originating from the $HH_1 - C_1$ edge, come out at the right energy and with the right slope. We note that the effect of the exciton character of the transitions is essential in obtaining not only the right energy, but also the right slope for the transitions corresponding to the lowest three exciton states. An additional downward shift of $\simeq 9$ meV has been imposed on the lowest $HH_1 - C_1$ and $LH_1 - C_1$ lines to fit approximately the $HH_1 - C_1$ exciton peaks. This value of the zero-field heavy-hole exciton binding energy agrees with the value of 9.4 meV derived from a photoluminescence study of a 80 Å $GaAs/Al_{0.3}Ga_{0.7}As$ QW reported in Ref. [64].

[6] Note that E_B doesn't depend on the reduced mass μ.

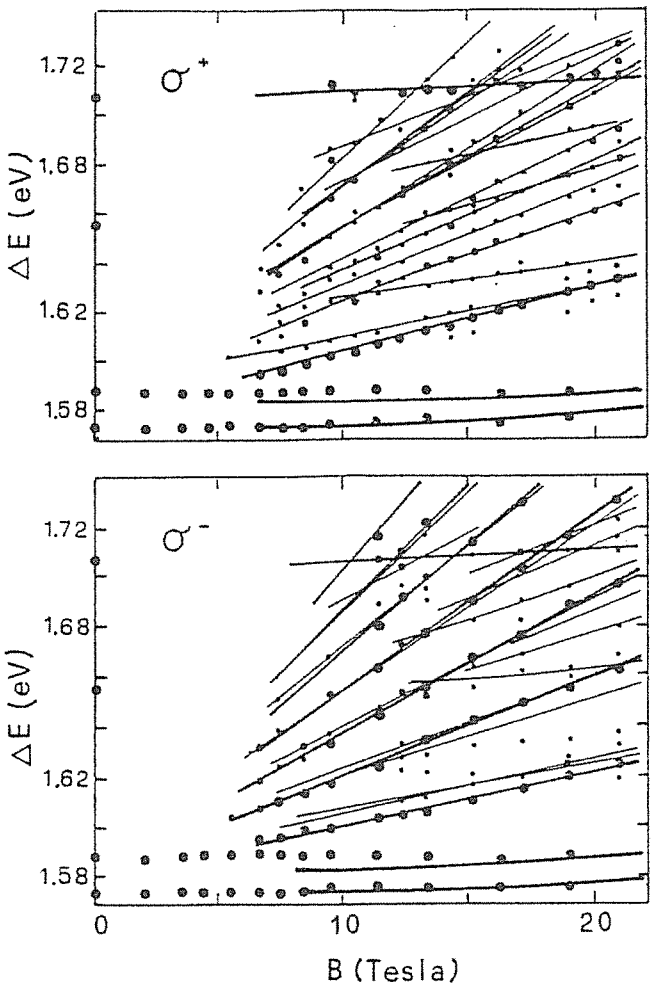

Figure 3.9:
Comparison between the calculated (lines) and the experimental transition energies (dots): excitonic corrections are included, as explained in the text. Large dots correspond to strong transitions, small dots to the weak ones.

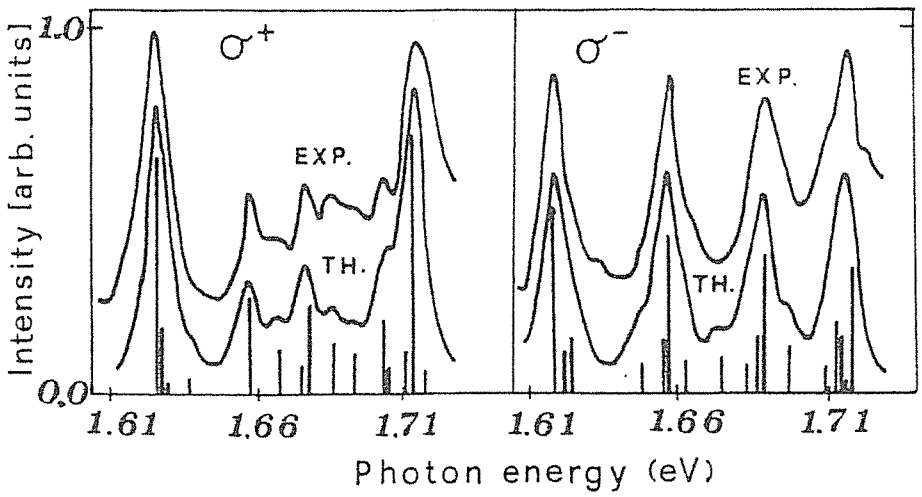

Figure 3.10:
Comparison between the excitation spectra measured at B=19 Tesla and the predicted intensities, for the two circular polarizations σ^+ and σ^- of the incident light. The theoretical curves have been obtained by dressing each of the calculated intensity bars with Lorentzian-shaped profiles 7 meV wide.

In Fig.3.10 the predicted intensities at $B = 19$ Tesla, calculated as explained in Sect.3.4, are compared with the experimental ones, for both polarizations (the two lowest exciton peaks visible in Fig.3.9 are not shown in the figure). In order to mimic the broadening of the observed peaks, we have dressed each of the calculated intensity bars with a Lorentzian-shaped profile 7 meV wide We see from Fig.3.10 that the differences between the observed σ^+ and σ^- spectra come out naturally from the calculation, making the overall agreement satisfactory. It should be remarked that a small change in the relative energy position of transitions originating from different subbands, such as $LH_1 - C_1$ or $HH_2 - C_1$, has a sensible effect on the observed spectra. Since the position of the subbands is extremely sensitive to the values of the material parameters (thickness, Aluminum content, band-offset mainly) an exact knowledge of the latters is required in order to make a successful comparison between theory and experiments.

A surprising fact is that we need to use a value for the electron mass at the edge of the conduction band ($m^* = 0.074$, corresponding to the value $P = 8.85\, eV \cdot \AA$ in (3.7)) higher than the commonly adopted value $m^* = 0.067$ [47]: we have also tried to analyze samples used in different experiments [48,69] and consistently arrived at the same conclusion, i.e. a *higher* electron mass is needed

to fit the experimental data.

At present it is not possible to state unambiguously whether this effect is due to the quantum well, or to a higher non-parabolicity of the bulk or to the approximate treatment of the exciton: we have verified however that the *bulk*-GaAs magneto-absorption spectra [62] are reproduced in detail by a calculation of inter-Landau level transitions when the value $m^* = 0.067$ is used. Both the effect of the exciton and that of enhanced non-parabolicity is to reduce the slope of the transition energies as a function of the field B; therefore the two effects cannot easily be distinguished. The position of the subbands at zero magnetic field is only weakly dependent on the mass used in the range of uncertainty relevant here (for comparison we show in Fig.3.4 this dependence). There are several indications that the *bulk*-GaAs non-parabolicity is indeed stronger than that predicted by the six-band model used here [70,71]: however, a clear distinction between the two effects requires a careful treatment of the effect of the exciton, the complex valence band structure and the magnetic field effect simultaneously.

Chapter 4

Spin-dependent relaxation in Quantum Wells.

4.1 Spin-dependent relaxation in Quantum Wells.

In recent years the problem of thermalization processes in direct-gap semiconductors of the family of III-V compounds has received much attention [72]. Time-resolved photoluminescence experiments on these systems [73,74,75]) have shown that the processes of thermal relaxation from excited states are rather fast, such that the characteristic relaxation time is at least one order of magnitude shorter than the band-to-band recombination time (< 1 ns). These experimental results are found to be in quite good agreement with theoretical predictions based on the consideration of the electron (hole)-phonon interaction [76,77].

On the other hand, it is well established [65] that spin relaxation is a rather slow process whose characteristic time is larger than or comparable with the recombination time. For the bound states in three-dimensional semiconductors the slow spin relaxation processes are not relevant for energy relaxation since in that case there always exist states with different spin components which are degenerate in energy. However, in a 2D structure such as that realized, for instance, in a GaAs Quantum Well, when a magnetic field is applied perpendicularly to the plane of motion, no overlap exists between spin-split states, due to the full quantization of the 2D degrees of freedom in the QW layer. In this case it may be expected that the spin relaxation may be a bottleneck for the energy relaxation.

Recently, photoluminescence experiments were performed on GaAs QW in order to observe spin-relaxation effects[78,79]. In these experiments were studied high-quality GaAs (undoped) multi-Quantum Well samples (of thickness between 45 and 200 $\mathring{A}$), sandwiched between $Ga_{1-x}Al_xAs$ barriers ($x = 0.26 - 0.43$). The luminescence [1] and excitation [2] spectra have been measured at $T = 1.5°K$ and in magnetic fields applied perpendicularly to the QW layers from 0 to $20T$ in the Faraday configuration (see Footnote 4 in Chapter 3), analysing both emitted and exciting light in different circular polarizations (σ^+ and σ^-). The photoluminescence spectra shown in Fig.4.1 have been obtained with a 140 $\mathring{A}$ $GaAs/Ga_{0.67}Al_{0.33}As$ QW, but all samples showed the same behaviour. The single luminescence peak, observed at zero magnetic field at a wavelength $\lambda \sim 8000\,\mathring{A}$, splits at high magnetic fields into two components, designated as peak A and B, which are observed in different polarization of the emitted light (see the inset in Fig.4.1). In particular, the higher energy peak B is found to remain always well observable, even at the lowest excitation power ($< 1\,mW/cm^2$), thus showing that the states involved in these transitions are not in thermal equilibrium, which is in turn an indication that the relaxation time between these states is comparable to the recombination time. When $B \neq 0$, several peaks are observed in the excitation spectra, as the continuum of states splits into discrete electron and hole Landau levels. In Fig.4.1 the luminescence intensities of both these peaks are compared as a function of the energy of the σ^+ polarized exciting light, at $B = 18T$. Since the exciting light is absorbed in the same states in both cases, the difference in the two spectra therefore reflects a selective relaxation to either A or B, and which relaxation path is preferred is a property of the excited state.

In order to explain the pronounced differences between the A and B spectra, one has to identify the nature of the state involved. Strictly speaking, the quasi two-dimensional magneto-excitonic states [65,43] are responsible for the transitions considered here. The lowest two luminescence transitions A and B

[1] In photoluminescence experiments electrons are excited by the absorption of light from their ground-state to higher energy states in the conduction band. After a quick relaxation through (lower lying) intermediate states, they eventually recombine with the holes by emitting photons which can be detected by a spectrometer.

[2] Unlike the case of photoluminescence experiments in which the source of the exciting light is set on a fixed frequency and the spectrometer is tuned, in excitation spectroscopy experiments the light source is tuned whereas the spectrometer is set on the maximum of the luminescence peak: one thus observes the luminescence intensity as a function of the energy of the exciting light.

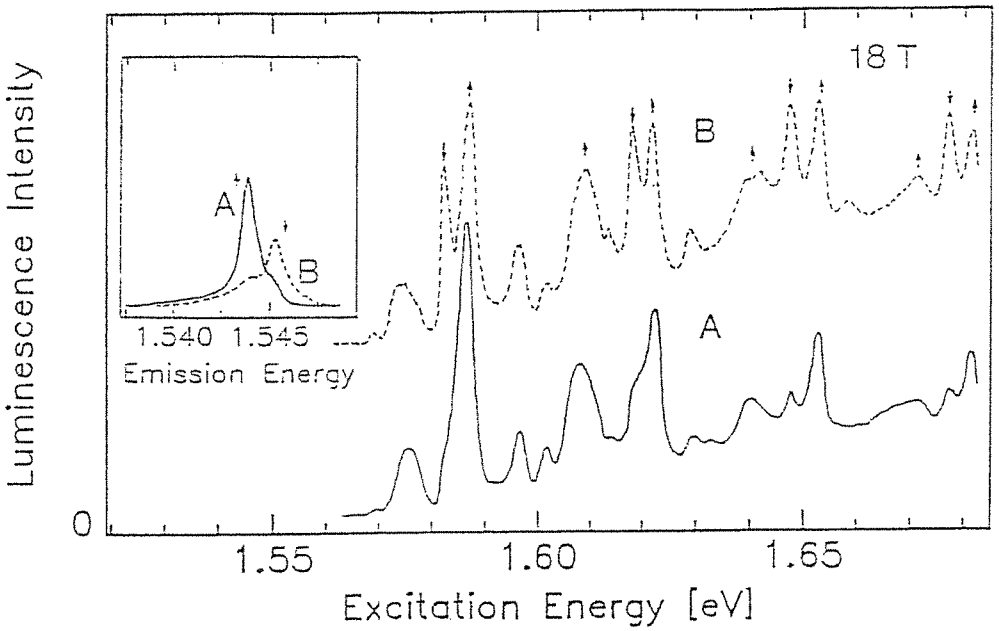

In the inset the σ^+ and σ^- circular polarization components of the luminescence, A and B, respectively. The intensity dependence as a function of the energy of the σ^+ polarized exciting light for each of these luminescence peaks.The arrows indicate the electron spin orientation of the transitions involved.

Figure 4.1:

are at high magnetic fields the two components of the spin-split $1s$ ground state of the Heavy Hole exciton and the higher energy states correspond to the excited states of the magneto-exciton. However, as shown by the results of Chapter 3, at high magnetic fields the observed transitions are closely related to interband transitions between the Landau levels of the holes and those of the electrons [59]. The electronic Landau levels are described by simple Landau "ladders" with each Landau level split into two, well defined, spin components. The hole Landau levels display on the contrary a strong non-linear behaviour [35], due to combined effect of the valence band-edge degeneracy typical of cubic direct-gap semiconductors and of the quantum confinement in the Superlattice potential (compare with the results of Fig.3.1 and Fig.3.2, where the Landau levels for electrons and holes in a GaAs QW are shown).

As a result of spin-orbit coupling, these hole Landau levels cannot be separated into spin-up and spin-down states but, with the exception of the ground state, have always a rather mixed character. Therefore the observed transitions involve electron Landau levels with pure spin-up or spin-down character and hole Landau levels with a mixed spin-orbit character. States which can be excited in one polarization, say σ^+, may involve electron levels with either spin-up or spin-down character. The ground states which give rise to the observed luminescence, however, are purely spin-up in one polarization and spin-down in the other polarization. The hypothesis made in order to explain the differences between the A and B spectra of Fig.4.1 is [78,79] that the excited states involving a conduction band spin-up preferentially relax to that ground state which has the same orientation of the electronic spin, and do not want to change their magnetic moment during the relaxation. The thermalization via the hole levels is thought to occur without difficulties because through the spin-orbit coupling the holes can relax easily by interaction with the lattice or with impurities. The electron, however, can only change its spin through a magnetic interaction which is much less probable.

In order to prove this hypothesis, in Ref.[78] the observed high- field transitions are compared with the theoretical calculations (performed in the way described at length in Chapter 2 and 3) for the interband transitions, which are allowed in this polarization (see Fig.4.2). The theoretical evaluation of transition energies and strengths allows to identify unambiguously the observed transitions and attribute the conduction-band spin component for each of them (arrows in Fig.4.1). It is clearly visible in Fig.4.1 that, in a given excitation spectrum, those peak are enhanced which involve the same spin components of

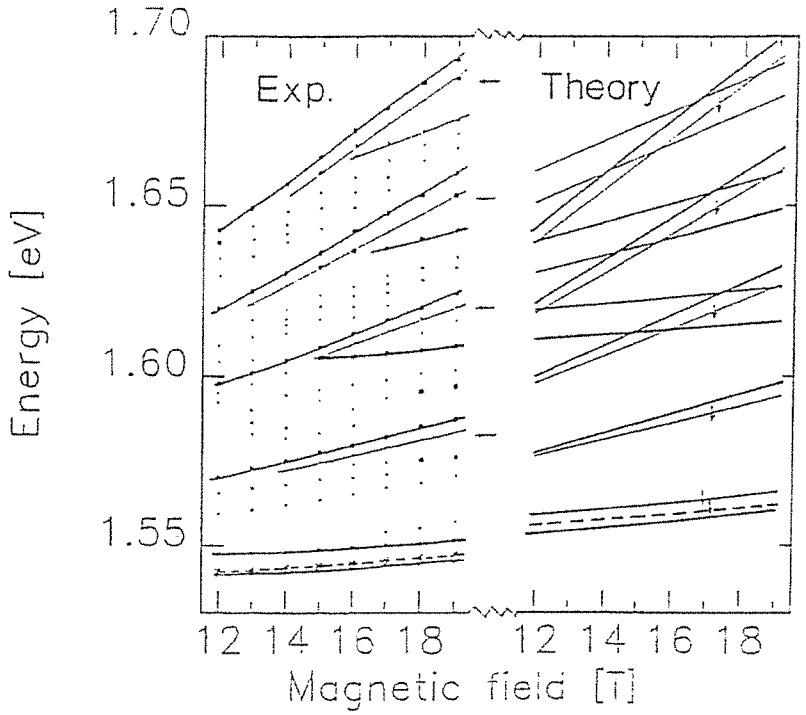

Energy of the maxima in the σ^+ excitation spectra, (detected in the low energy tail of the luminescence), at high magnetic fields (left panel). The size of the data points reflects the intensity of the peaks. Peaks which are enhanced when recording the excitation spectra of the σ^- polarized peak B_2 (the position of which is indicated by the dashed line), are marked. The calculated field dependences of the most intense interband transitions allowed in σ^+ polarization (right panel). The dashed line denotes the σ^- allowed ground state and the transitions having the same conduction band spin orientation ($\downarrow$) as this state are indicated.

Figure 4.2:

conduction band states both in absorption and in emission. This shows that the relaxation of carriers from the excited to the ground state in QW in a magnetic field is much more efficient between states having the same conduction band spin, and that spin-flip processes are relatively improbable. Accordingly, also between the two lowest states of opposite spin, the energy relaxation time ($\tau'_{\uparrow\downarrow}$) is rather long (of the order of the recombination time) and is probably determined by electron spin relaxation time.

The situation is schematically summarized in Fig.4.3, where the relevant thermalization and recombination processes are shown. Note in particular that, due to the fact that the relaxation time $\tau'_{\uparrow\downarrow}$ between the two spin-split components of the ground state is larger than the radiative recombination time τ_{rad} ($\tau_{\uparrow\downarrow} \gtrsim 4\tau_{rad}$, as found in Ref. [80]), it becomes possible to obtain at equilibrium a population inversion for the two spin components of the ground-state, as it is apparent from part (a) of Fig.4.3.

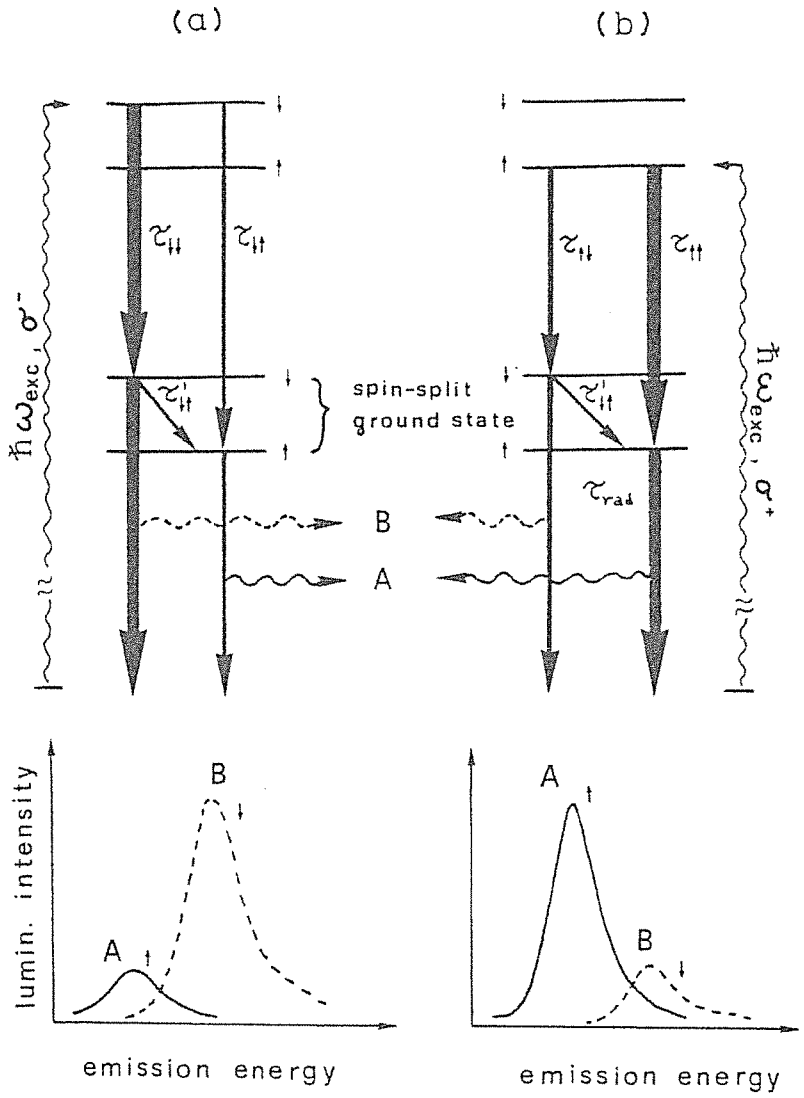

Figure 4.3:
Upper part: schematic picture of the thermalization and recombination processes involved in the photoluminescence experiment described in the text.
Lower part: σ^+ (solid lines) and σ^- (dashed lines) circular polarization components of the luminescence at high magnetic fields.

Chapter 5

Cyclotron resonance in two-dimensional hole gas.

5.1 Cyclotron resonance in a 2D hole gas in doped Quantum Well structures.

In this Chapter we will give a brief account of Cyclotron Resonance (CR) experiments in the Two-Dimensional Hole gas in doped Quantum well structures. The observed spectra are considerably richer than expected from simple Landau theory (see below). We will show how the essential features of these spectra can be accounted for, at least in a qualitative way, by the very unusual dependence on the magnetic field of the hole Landau levels in Quantum well systems [81,84,44,85] (see also Fig.3.1 and the related discussion in Sect.3.3).

Consider the simple, illustrative example of a quasi-free electron in a crystal placed in an external magnetic field B applied along the z-direction. Assuming a parabolic dispersion relation with an effective mass m^*, the energy levels are given by:

$$E_n = \hbar\omega_c(n + \frac{1}{2}) + \frac{\hbar^2 k_z^2}{2m^*} \tag{5.1}$$

where $\omega_c \equiv eB/m^*c$ is the cyclotron frequency, k_z is the electron wave vector in the z-direction and n is an integer. CR follow from transitions between the Landau levels (5.1): the resonance condition of the system when interacting with electromagnetic radiation of frequency ω is just:

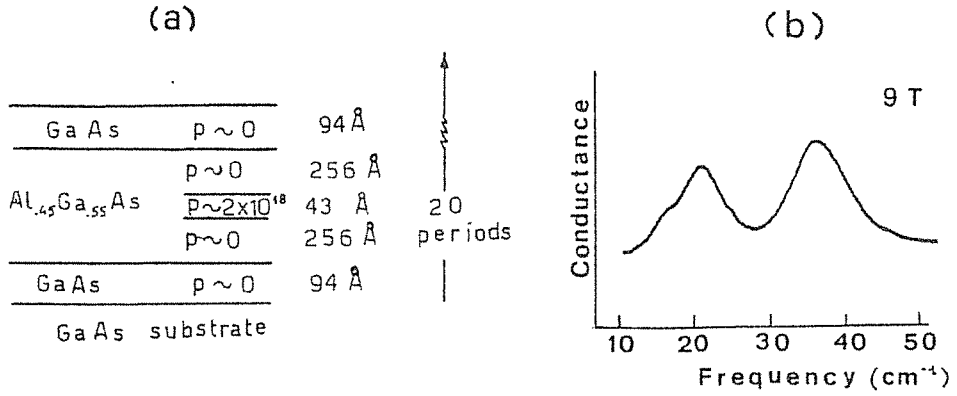

Figure 5.1:
(a) The doping and layering of the Multi-Quantum Well sample (from Ref.[81]) referred to in the text.

(b) Conductance vs. frequency spectrum at $B = 9T$.

$$\omega = \omega_c \tag{5.2}$$

This simple picture of quasi-free electrons is applicable to real systems as long as the carrier density is so low that they occupy the states near the band extremum.

The situation in a Quantum Well is noticeably different. We have shown in Sect.3.3 how the coupling between Light and Heavy hole bands gives rise to Landau levels that are not equally spaced and have a very non-linear magnetic field dependence (see, for instance, Fig.3.1). The unequal level spacing gives rise to a multiplet of cyclotron frequencies at a particular value of the magnetic field instead of the single frequency (5.2) predicted by a parabolic band model. This is actually confirmed by CR experiments: in Fig.5.1b we reproduce, from Ref.[81], the CR spectrum at $B = 9T$ in the 2D-hole gas formed in the $GaAs/AlGaAs$ multiple-QW structure shown in Fig.5.1a: in this structure holes are transferred from the acceptors in the p-doped AlGaAs into the GaAs Quantum Well, where they occupy, for sufficiently low densities, the first quantized level at $B = 0$. For a finite value of the magnetic field, transitions from occupied Landau levels to empty ones give rise to Cyclotron Resonance spectra. The two peaks in Fig.5.1b correspond to effective masses $m^* = 0.41$ and $m^* = 0.23$ (in units of the free electron mass), according to the definition:

$$m^* = e\hbar B/c\Delta E \tag{5.3}$$

Here ΔE is the energy difference between the two Landau levels.

The matrix elements for an optical transition between an initial hole state characterized by a Landau index n to a final state n' are given by a term analogous to the second term in (3.14), and are given by the expression (see Appendix F for a detailed derivation):

$$M_{nn'} \propto (c/eB)^{1/2}(E_{fin} - E_{in})\varepsilon_{\pm} < F_n^{in}|a^{\pm}|F_{n'}^{fin} > \tag{5.4}$$

Here $|F_n^{in,fin} >$ is the envelope function (3.9) solution of the Effective Mass equation $\sum_{j'}(H_{ax})_{jj'}F_n^{j'} = EF_n^j$ (see Sect.3.2 and 3.4 for the notation).

From the definition (3.15) of the scalar product $< F_n^{in}|F_{n'}^{fin} >$ and from the orthogonality of the oscillator states with different index n, one derives immediately the following selection rule:

$$\Delta n = \pm 1 \tag{5.5}$$

where the + (-) sign holds for left (right) circularly polarized light. We underline the fact that the above selection rule pertains to the axial model only [1].

We have performed a calculation of the hole Landau levels, with the methods described in Chapter 2 and 3, for the case of a 94 $\AA$ GaAs-Quantum Well between thick AlGaAs barriers, in the axial approximation and assuming that the band gap difference between GaAs and AlGaAs is shared between conduction and valence band, respectively, according to the 60/40% rule.

Unlike the case of interband transitions treated in Sect.3.4, now we must add to the diagonal terms of the hole Hamiltonian matrix an additional electrostatic potential $V(z)$ arising from the mobile holes in the GaAs Well and from the ionized acceptors in the p-doped AlGaAs layer (see Fig.5.1a) . In principle $V(z)$ should be calculated self-consistently for every value of the field B (see Ref.[84]): usually this is done in the Hartree approximation, where exchange and correlation effects are neglected (this is a good approximation as long as $r_s \ll 1$: we will see that this is not the case here). However, such a calculation usually implies a heavy computational effort. We made here the simpler, "zeroth-order" approximation that consists in solving the Poisson equation in

[1] If one uses the exact Hamiltonian [95] $H = H_{ax} + H_{cub} + H_k + H_G$ (where H_{ax} and H_{cub} have the form (3.7,3.8) and H_k, H_G account for linear k terms and G-terms [26] that come in when the crystal lacks inversion symmetry) the selection rule (5.5) must be relaxed and one has instead $\Delta n = \pm m$, with m odd integer. The terms with $m = 1$ are expected to be strong, while the ones with $m > 3$ come in with H_{cub} and would be absent in the axial approximation.

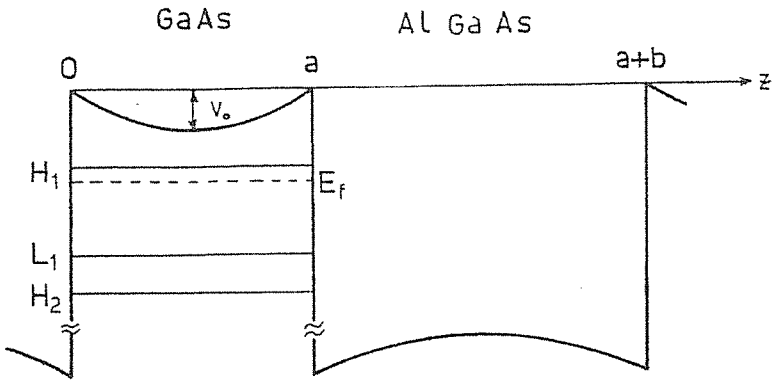

Figure 5.2:
Valence-band energy profile for a 94 Å GaAs-Quantum Well between GaAlAs barriers in the presence of a uniform density of mobile holes in the GaAs layer. The position of the hole subbands is shown, together with the 2-D Fermi-energy level.

the presence of a *uniform* hole density in the heterostructure and assuming that the doped layers are completely depleted. This results in the simple parabolic profile superimposed on the valence-subband square-wave potential, as shown in Fig.5.2. The explicit expression of $V(z)$, measured from the top of the valence band, is:

$$V(z) = (2\pi e^2 N_s/\varepsilon) z(1 - z/a) \tag{5.6}$$

a being the Quantum Well width, ε the dielectric constant of GaAs and N_s is the two-dimensional density of holes. We will use in the following the value $N_s \simeq 4.6 \times 10^{11}\, cm^{-2}$, taken from the experimental results of Ref.[81]. Thus, at the center of the well, $|V| \simeq 8\, meV$. The first hole bound states at $B = 0$ are shown in the figure. The dashed line indicates the position of the 2D Fermi energy: we used here the simple expression valid for parabolic bands $E_F = \pi\hbar^2 N_s/m^*$. Since at sufficiently low carrier densities we expect the highest (Heavy hole) subband only to be populated, we use for m^* the value of the effective HH mass in the z-direction (see Eq.2.22a), $m^*_{HH} = 0.377$. Then $E_F \simeq 2.9\, meV$ (measured with respect to the first quantized level): we see from Fig.5.2 that only the highest subband is indeed occupied.

To deduce the CR absorption spectrum from the calculated hole Landau levels one must consider, in addition to the selection rules, also the occupation of initial and final states: transitions that are allowed by the selection rule (5.5) take place only from a (partially) filled Landau level to a (partially) empty one [84]. The filling factor for a 2D system of N_s free-carriers per unit area in the

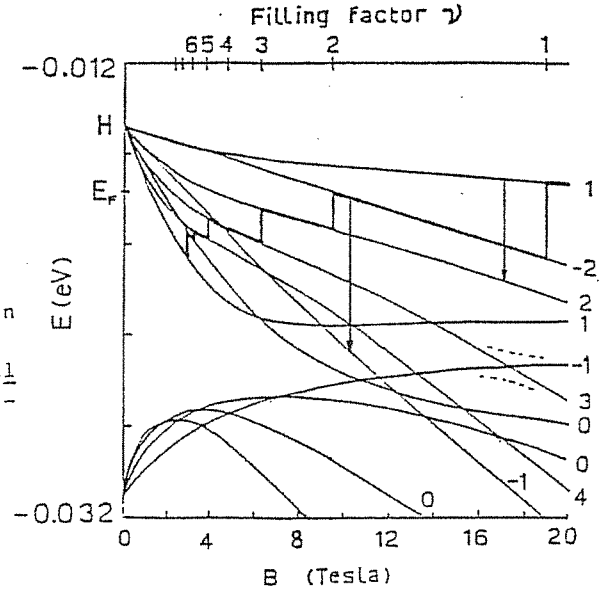

Landau levels in a 94 Å GaAs Quantum Well between thick AlGaAs barriers. The Fermi level position for $N_s = 4.6 \times 10^{11}$ holes/cm^2 is indicated for higher fields by the thick line : its position at B=0 is also indicated. The dashed lines show the calculated splitting of the Landau levels with n=-1 and n=3 due to the anisotropic term in the hole Hamiltonian

Figure 5.3:

presence of a magnetic field is given by [2]:

$$\nu = hcN_s/eB \tag{5.7}$$

Using for N_s the value already quoted, one finds $\nu \simeq 19/B$, B in Tesla. This means that, for instance, the first Landau level is filled at $B = 19\,T$; the second is partially filled between 19 and $9.5\,T$, etc. In Fig.5.3 we show the calculated Landau level structure: the thick line indicates the position of the Fermi level at high fields, as obtained with the simple filling scheme described above. Two possible transitions ($1 \rightarrow 2$ and $-2 \rightarrow -1$) are also shown.

From the results of Fig.5.3 we have calculated the energies of the allowed transitions, for different values of the magnetic field, and taking into account the filling of Landau levels as described above. The resulting transition lines are shown in Fig.5.4, together with the experimental results taken from Ref.[81] [3]: full circles indicate strong peaks while open circles indicate weak features in the observed spectrum.

[2] We used for simplicity the Landau level degeneracy $\zeta = eB/hc$ appropriate to a parabolic band structure.

[3] In Ref.[81] these data are fitted using a simple model that simulate the hole confinement by introducing two adjustable parameters: only a rough semiquantitative agreement with experimental points is achieved.

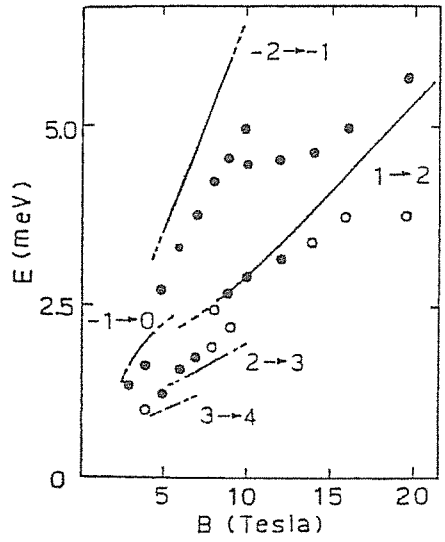

Measured cyclotron frequencies (dots) compared with theory (lines). Solid circles are strong transitions, open circles are weak ones. Theoretical transitions account for occupation effects, as described in the text. The Landau levels involved are also indicated.

Figure 5.4:

The dashed part of the calculated lines means that the corresponding transition takes place to an almost full level or from an almost empty one: these transitions are expected to be weak. One can see that the effective masses that come out from the calculation depend on the magnetic field both because the energy difference ΔE between two given Landau levels varies with B in a non-linear way, and because transitions between different pairs of Landau levels become possible, depending on the particular value of the Fermi level E_F.

We see from Fig.5.4 that a rough semiquantitative agreement with experimental points is obtained. More sophisticated calculations of the energy levels of a 2D-Hole gas in a magnetic field don't do much better ([43,84,44]). A clear interpretation scheme of CR spectra in 2D-hole gas is still lacking. In particular, as it is apparent from Fig.5.4, a large splitting of the experimental cyclotron line, corresponding to the $1 \rightarrow 2$ transition in our scheme, occurs in the extreme quantum regime where only the highest hole Landau level is occupied ($\nu < 1$). This effect has been observed in other CR experiments performed in heterostructures [86] and remains essentially unexplained.

It has been argued [85] that many-body interactions play a larger role in a 2D system of hole than in a 2D electron gas: this can be understood if one recalls the dependence on the effective mass of the reduced Wigner-Seitz radius $r_s = r_0/a_0^*$, $a_0^* = \varepsilon\hbar^2/e^2m^*$ being the effective Bohr radius and $r_0 = (\pi N_s)^{-1/2}$ the mean hole distance. Here $m_H^* = 0.377 \gg m_e^* = 0.067$. In this case $r_s \simeq 5$, indicating that exchange and correlation effects should be, in principle, taken

into account.

Chapter 6

Basic concepts of tunneling.

6.1 One-dimensional tunneling: an elementary review.

In the following, some of the basic concepts of tunneling will be illustrated by studying purely one-dimensional systems [98].

We consider the simple one-dimensional problem where the potential energy consists of square barriers and wells. The Schrödinger equation for a particle of mass m^* is:

$$[p^2/2m^* + V]\Psi = E\Psi \tag{6.1}$$

where $p^2 \equiv -\hbar^2 d^2/dx^2$ and V is a constant in a given region, changing abruptly from one constant value to another. The general solution of Eq.(6.1) can be written as:

$$\Psi(x) = ae^{ikx} + be^{-ikx} \tag{6.2}$$

$$\hbar^2 k^2/2m = E - V \tag{6.3}$$

When $E - V > 0$ the wave functions are plane waves. When $E - V < 0$ one writes in (6.2) $k = iK$ and obtains the exponentially growing and decaying waves characteristic of barrier penetration problems:

$$\Psi(x) = ae^{-Kx} + be^{Kx} \tag{6.4}$$

The overall wave function is constructed out of pieces having the form (6.2) or (6.4) by matching Ψ and $d\Psi/dx$ at the points of discontinuity of V [1].

The conditions of continuity of the logarithmic derivative at a potential step located at the point x_n can be conveniently described using a 2×2 matrix R_n operating on the two dimensional vectors (a_n, b_n) and (a_{n+1}, b_{n+1}) which represents the wave function (6.2) in the region to the left and to the right of x_n respectively. One can write

$$\begin{pmatrix} a_n \\ b_n \end{pmatrix} = R_n \begin{pmatrix} a_{n+1} \\ b_{n+1} \end{pmatrix} \tag{6.5}$$

where

$$R_n = \frac{1}{2k_n} \begin{vmatrix} (k_n + k_{n+1})e^{i(k_{n+1}-k_n)x_n} & (k_n - k_{n+1})e^{-i(k_{n+1}+k_n)x_n} \\ (k_n - k_{n+1})e^{i(k_{n+1}+k_n)x_n} & (k_n + k_{n+1})e^{-i(k_{n+1}-k_n)x_n} \end{vmatrix} \tag{6.6}$$

k_n and k_{n+1} are the particle wave-vectors (either real or imaginary) in the two regions respectively.

The effect of a mass-mismatch at the point x_n (see Footnote) can be simply included by using at each point of discontinuity x_n of the potential an iteration matrix R_n which is obtained from the expression (6.6) with the formal replacement $k_n \rightarrow (1/m_n^*)k_n$, $k_{n+1} \rightarrow (1/m_{n+1}^*)k_{n+1}$ in the pre-factors in front of the exponentials, $m_{n,(n+1)}^*$ being the effective masses to the left (right) of the matching point respectively.

We consider here the simple case of a rectangular barrier of height V_0 and width d, extending from x_1 to x_2 :

$$V(x) = \begin{cases} V_0 & \text{if } x_1 < x < x_2 \\ 0 & \text{otherwise} \end{cases} \tag{6.7}$$

We remark that this is the simplest way to model the electrostatic potential felt by an electron propagating across an epitaxial semiconductor heterostructure like an undoped GaAs/AlGaAs/GaAs system, the discontinuity in the potential being determined by the different line-up of the conduction band-edges of the two materials making up the heterostructure. We will assume in

[1] When the mass m^* is different in regions of different potential energy, as it happens when one dimensional models are used to represent real interface systems, the appropriate boundary condition at a point of discontinuity of the potential is [99] Ψ *and* $(1/m^*)d\Psi/dx$ *continuous*. These are the most general boundary conditions that assure the conservation of the current density along the x-direction at the interface [99].

the following the same effective mass inside and outside the barrier region: this can be justified, in the prototype case of a GaAs/GaAlAs boundary, when the Aluminum concentration in the barrier material is low.

According to (6.5), one connects the wave functions in the regions I and III to the left and to the right of the barrier (6.7) through the relation [2]:

$$\begin{pmatrix} a_1 \\ b_1 \end{pmatrix} = R_1 R_2 \begin{pmatrix} a_3 \\ b_3 \end{pmatrix} \tag{6.8}$$

where R_1 and R_2 are the transfer matrices for the two points of discontinuity x_1 and x_2; they have the same form as (6.6) except that the wave-vector k_2 in R_1 and R_2 is pure imaginary, say $iK \equiv i[2m^*(V_0 - E)/\hbar^2]^{1/2}$, to describe the exponentially decaying waves in the region II inside the barrier. We assume for simplicity that $k_1 = k_3$ $(= k \equiv (2m^*E/\hbar^2)^{1/2})$, i.e. the (constant) potential in region I and III has the same value.

For an electron incident on the barrier (6.7) from the left, with an energy E less than the top of the barrier height V_0, there will be a reflected wave in region I but only a transmitted wave in region III. Hence $b_3 = 0$. Eq.(6.8) then gives

$$a_1 = (R_1 R_2)_{11} a_3 \tag{6.9}$$

Explicit evaluation of the matrix element in (6.9) with the use of (6.6) results in

$$(R_1 R_2)_{11}^{-1} \simeq \frac{4kK\phi e^{-Kd}}{(k^2 + K^2)} \tag{6.10}$$

ϕ is a phase factor which we ignore in the following. In deriving (6.10) we have used the plane-wave solutions (6.2) in region I and III and the tunneling states (6.4) in region II. Moreover, to simplify the formulas, terms such as e^{-Kd} have been neglected in comparison to terms in e^{Kd}. In other words we are considering strongly attenuating barriers only, characterized by having $Kd \gg 1$.

A quantity of physical interest is the ratio of the transmitted current to the incident current j_t/j_i, where $j_i = (\hbar k/m)|a_1|^2$ and $j_t = (\hbar k/m)|a_3|^2$. This ratio is by definition the barrier transmission coefficient T_s. From (6.9) and (6.10) one finds:

$$T_s \simeq \frac{16k^2K^2}{(k^2 + K^2)^2} e^{-2Kd} \tag{6.11}$$

[2]Note that the general problem of any number of square barriers or wells can be succinctly described in terms of a chain of operators of the form (6.6), i.e. the problem of matching the wavefunctions is reduced to a matrix multiplication.

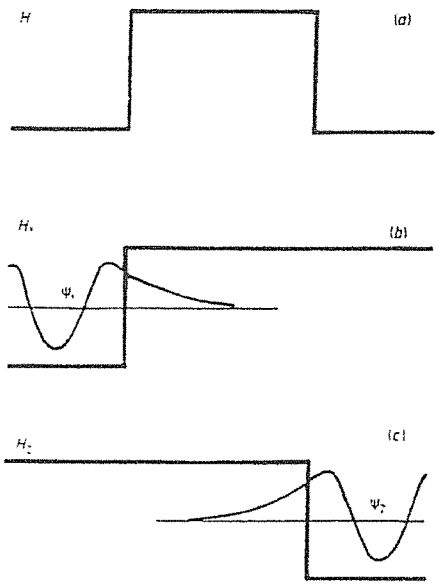

(a) A tunnel junction with a homogeneous barrier. (b), (c) The two electrode–barrier subsystems used in the transfer Hamiltonian description of the junction.

Figure 6.1:

The dominant feature of Eq.(6.11) is the barrier penetration factor e^{-2Kd}. In problems of practical interest this factor may be as small as $10^{-5} - 10^{-10}$.

The smallness of the right hand side of Eq.(6.11) suggests that a perturbation treatment of tunneling would also be appropriate. Starting from this observation, Bardeen[100] developed a useful formalism for the calculation of the tunnel currents. The most spectacular application of this formalism was its use to predict the Josephson effect [101]. We show in the following how the expression (6.11) for the single barrier transmission coefficient can be derived using the Bardeen's approach.

In brief, the method is based on the separation of the tunnel system (in the present case a tunnel junction containing a potential barrier between two "electrodes") into subsystems, each consisting in a single electrode connected to a semi-infinite barrier (see Fig.6.1). These subsystems are described by Hamiltonians H_1 and H_2. The eigenstates of the subsystems Ψ_1 and Ψ_2 and their energies ε_1 and ε_2 are defined by

$$H_1\Psi_1 = \varepsilon_1\Psi_1$$

$$H_2\Psi_2 = \varepsilon_2\Psi_2 \tag{6.12}$$

These states are oscillatory in the positive-energy regions and drop exponentially in the adjacent negative-energy regions, as shown schematically in Fig.6.1. Ψ_1 and Ψ_2 can be easily obtained by matching solutions of the form (6.2) and (6.4) separately at each potential step in Fig.6.1. One assumes that the electron is initially in Ψ_1 and wants to compute its transition rate into state Ψ_2. The transmitted current j_t is calculated using the "golden rule" of first-order time-dependent perturbation theory:

$$j_t = (2\pi/\hbar)|T_{21}|^2\rho_2 \tag{6.13}$$

where T_{21} is the matrix element for the transition $\Psi_1 \rightarrow \Psi_2$ and $\rho_2 = m^*L/2\pi\hbar^2 k$ is the density of states in one dimension, without spin (we used a normalization in a box of length L). Following Ref.[100], one can write T_{21} in terms of the matrix elements of the current density operator between the states Ψ_2 and Ψ_1:

$$T_{21} = -i\hbar j_{21} \tag{6.14}$$

where

$$j_{21} = -\frac{i\hbar}{2m^*}(\Psi_2^*(x)\frac{d\Psi_1}{dx} - \Psi_1^*(x)\frac{d\Psi_2}{dx})|_{x_B} \tag{6.15}$$

The above expression is to be evaluated at any point x_B in the barrier. From the definitions (6.14) and from the explicit expressions of Ψ_1 and Ψ_2 one then obtains easily for the transmission coefficient $T_s \equiv j_t/j_i$ the same expression (6.11) derived from the simple plane-wave matching procedure.

The Transfer Hamiltonian method ignores the part of the wave function which is reflected from the distant electrode-barrier interface and the formalism can only be applied if that part of the wave function is small. This condition is fulfilled when the tunneling probability is small, i.e. for very thick and/or high barriers.

6.2 Resonant tunneling in double-barrier structures.

We turn now to discuss briefly another textbook example of square-barrier model, i.e. the Double-Barrier (**DB**) structure. This consists, in the simplest case, in two equal tunneling barriers of width d and height V_0 separated by a well of width a, as shown in the left part of Fig.6.2. A practical realization of a

DB structure consists for instance of an undoped GaAs layer (well) sandwiched between undoped $Ga_xAl_{1-x}As$ layers (barriers). Usually, carriers are injected and collected from n or p -doped GaAs buffers which enclose the DB structure. A thorough review of semiconductor hetero-structures and their properties is contained in Chapter 1 of this thesis.

If we assume a wave incident from the left and transmitted to the right, the ratio T_d of the transmitted to incident current is given by a simple generalization of Eq.(6.9), i.e.:

$$T_d \equiv j_t/j_i = |a_5|^2/|a_1|^2$$
$$a_1 = (R_1R_2R_3R_4)_{11}a_5 \tag{6.16}$$

The explicit expression for T_d is fairly complicated (see, for instance, Ref.[112]). We note however that, neglecting in this expression terms which are exponentially small in Kd, one can write:

$$T_d(E) \simeq \frac{C_0}{C_1 + C_2e^{4Kd}} \tag{6.17}$$

where C_0,C_1 and C_2 are numbers of order of 1, slowly varying functions of the energy E of the incident particle. For $C_2 \neq 0$, $T_d \simeq exp[-4Kd] \simeq T_s^2$ (see Eq.(6.11)), i.e. the transmittivity of the DB structure is such as if no well was present between the two barriers (*non-resonant* tunneling). However, if for particular energies, say E_i, C_2 vanishes, one has $T_d = C_0/C_1 \sim 1$, giving rise to a strong enhancement of the transmittivity of the structure (*resonant* tunneling). From the explicit expression for T_d one sees that the condition $C_2 \simeq 0$ for resonant tunneling is:

$$(k^2 - K^2)sin(ka) \simeq 2kKcos(ka) \tag{6.18}$$

which is the usual condition which determines the bound-state energies E_r in a square well (i.e., as if the two confining barriers were infinitely extended in space) [102]. Thus resonant tunneling (**RT**) through a Double Barrier occurs when the energy of the incident particle matches that of an unoccupied discrete state in the Quantum well. A schematic plot of the transmission coefficient T_d for a simple double-barrier potential is shown in Fig.6.2. The width ΔE_r of the resonance peak at energy E_r is approximately given by [154]

$$\Delta E_r \simeq 2(ln2)^{1/2}E_r exp(-2K_r d) \tag{6.19}$$

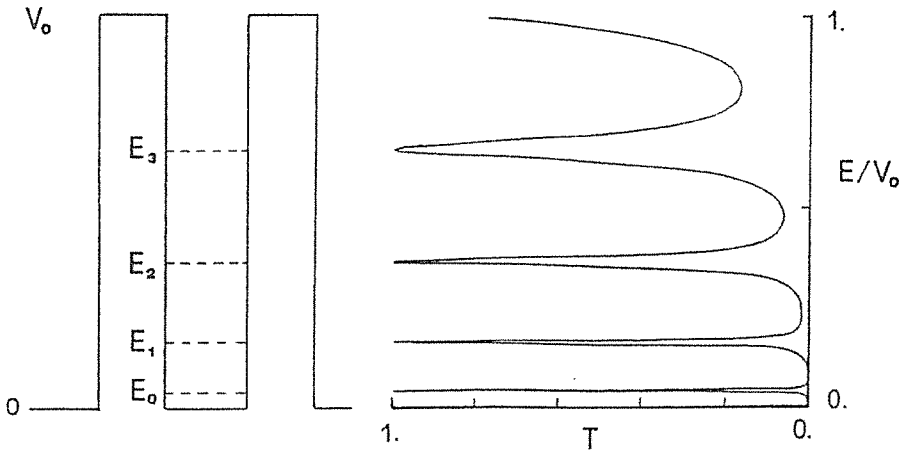

Figure 6.2:
Left: potential profile of an ideal Double-Barrier structure. The dashed lines indicate the position of the quasi-stationary states in the well.
Right: Transmission coefficient T_d of the Double Barrier.

where $K_r = [2m^*(V_0 - E_r)/\hbar^2]^{1/2}$.

Calculations of Resonant Tunneling through multiple barriers were presented in the pioneering work of Tsu and Esaki[103], followed by the observation of RT through a double barrier[104]. The static and high frequency transport through multiple barriers have been recently under intense experimental (see, for instance, Ref. [105,106,107]) and theoretical [107,108,110,109] investigations.

The recent revival of interest in RT and perpendicular transport in semiconductor hetero-structures is in large part motivated by the impressive progress achieved in epitaxial growth techniques, which has made possible to realize high-quality semiconductor hetero-structures. For comprehensive reviews on Resonant Tunneling and perpendicular transport, see, for instance, Ref.[117] and Ref.[119].

As it is well known, resonant tunneling results in Negative Differential Resistance (**NDR**) characteristics in the current-voltage curve of the DB when a bias is applied across the structure [104]. In Fig.6.3 we show a schematic plot of the expected I-V characteristic of a DB diode consisting of two degenerate doped electrodes separated by a double-barrier structure. One sees from the Figure (insets *a*, *b* and *c*) that at very low bias the current is basically zero, until the applied voltage reaches the value V_0 such that the energy of the quantum state inside the well coincides with the Fermi energy E_F of the left electrode.

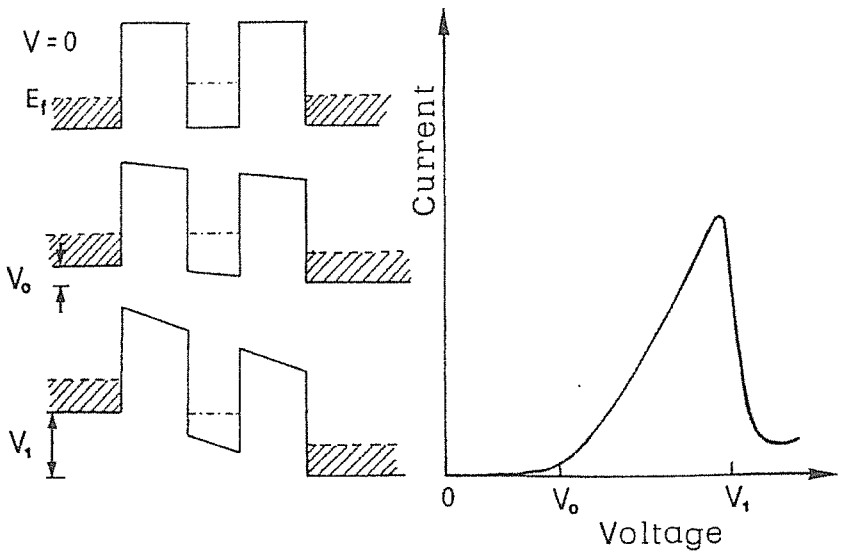

Figure 6.3:
Current-Voltage characteristic (schematic) for the Double-Barrier shown in the left part of the Figure. E_F indicates the position of the Fermi level of the doped semiconductor electrodes enclosing the DB structure.

At this point resonant tunneling proceeds, with the current increasing steadily with voltage up to a maximum value and then drops suddenly at a potential V_1 where the quantum state is below the conduction band edge of the injecting electrode and there is no localized state in the well available for tunneling. The total voltage width $V_1 - V_0$ is roughly twice the electrode Fermi energy E_F.

The description of resonant tunneling in the previous pages is usually referred to as *coherent* RT. The electron wavefunction produces interfering Fabry-Perot-like reflections from the first and second barrier: the electron waves leaking out in both directions cancel the reflected waves and enhance the transmitted ones, leading to an overall (almost) unity resonant transmission coefficient [107]. This coherent resonant-tunneling mechanism results, in turn, in NDR features in the observed tunnel current, as explained above.

However, as first pointed out by Luryi[110], the presence of negative differential resistance in the I-V characteristic of a DB hetero-structure is no direct proof that that the electronic wave function remains coherent during the whole tunneling process. A two-step process, in which the electrons hops from one electrode to the other, tunneling *sequentially* through the barriers via an intermediate quantum state, can also give rise to negative resistance [110]. The

basic principle of sequential tunneling is illustrated in Fig.6.4.

The intuitive view that the total tunnel current would be smaller in sequential tunneling than in coherent tunneling, has been recently disputed in Ref.[111] and Ref.[112], where the equivalence of the two mechanism was asserted. At first sight it seems impossible to reconcile the two points of view, since in the sequential tunneling model, where the hopping from one electrode into the well is controlled by the single barrier transmission coefficient T_s (see Eq.(6.11)), the current is expected to show the same exponential dependence on the "opacity" of the barrier Kd, i.e. $\sim exp(-2Kd)$. On the other hand, in coherent resonant tunneling the overall transmission coefficient is given by (6.17). However, although at resonance the transmission coefficient T_d is almost unity, the total tunnel current through the DB structure is given by an integral of the transmission coefficient over the range of energies of the incident electrons (see Eq.(L.6) in Appendix L) and thus the exponential narrowing of the resonance peak with Kd as given by Eq.(6.19) results in the same dependence $\sim exp(-2Kd)$ of the current expected in the sequential tunneling model.

Although the two models lead in principle to the same predictions for the tunnel current across the structure, in the practical realizations of DB heterostructures the phase coherence of the tunneling electrons can be destroyed by scattering events in the well region (impurity scattering, phonon scattering, etc.), which randomize the momentum of the electrons parallel to the layers constituting the hetero-structures. In this case no resonant behavior occurs but the electrons can still tunnel in and out of the well *sequentially*. However, the equivalence between the two models has been shown to hold also in the presence of intra-subband scattering (i.e. scattering in the direction parallel to the Quantum Well layer) when the incoming distribution in energy δE of the electrons is broader than the width ΔE of the quasi-two-dimensional level in the well [111] (this is true for instance when electrons are injected into the well from a thermalized heavily doped electrode, which is the situation most frequently encountered in experiments.). In the opposite case, i.e. when $\delta E < \Delta E$, one should compare [113] the characteristic time τ_0 for the build-up of the resonance, given by [107]

$$\tau_0 \sim \hbar/\Delta E \tag{6.20}$$

with τ_{sc}, where τ_{sc} is the lifetime for lateral scattering in the well region. If $\tau_{sc} \gg \tau_0$, then one expects *coherent* resonant tunneling; if if on the other hand $\tau_{sc} \ll \tau_0$, the *sequential* process should prevail.

Both mechanisms have been observed in experiments. Quite recently [114]

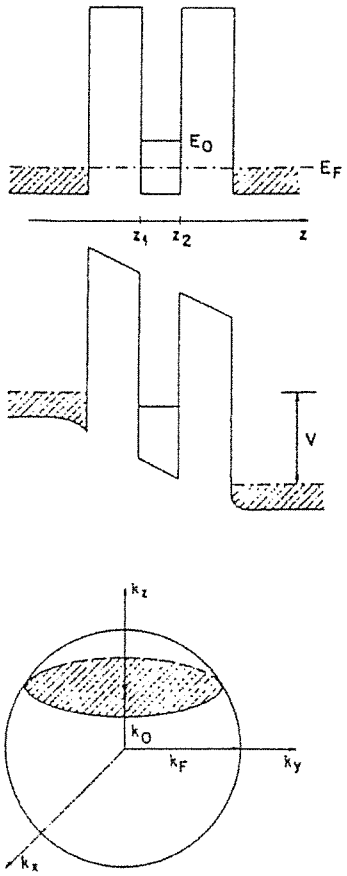

Illustration of the operation of a double-barrier resonant-tunneling diode. The top part shows the electron energy diagram in equilibrium. The middle displays the band diagram for an applied bias V, when the energy of certain electrons in the emitter matches unoccupied levels of the lowest subband E_n in the QW. The bottom illustrates the Fermi surface for a degenerately doped emitter. Assuming conservation of the lateral momentum during tunneling, only those emitter electrons whose momenta lie on a disk $k_z = k_n$ (shaded disk) are resonant. The energy separation between E_0 and the bottom of the conduction band in the emitter is given by $\hbar^2 k_0^2/2m$. In an ideal DBD at zero temperature the resonant tunneling occurs in a voltage range during which the shaded disk moves down from the pole to the equatorial plane of the emitter Fermi sphere. At higher V (when $k_0^2 < 0$) resonant electrons no longer exist.

Figure 6.4:

the *coherent* tunneling of photoexcited electrons through an a-symmetrical double-barrier superlattice was evidenced and unambiguously differentiated from the sequential tunneling process. On the other hand, the *sequential* resonant tunneling of electrons was observed in multi-Quantum Well structures, as reported in Ref.[115].

Roughly speaking, the maximum operating frequency (and thus the ultimate speed) of a device based on RT is limited essentially by the "well storage" time τ_0 [106].

One can estimate the lifetime τ_0 of the resonance associated with a quasi 2-D level of energy E_r inside the well by using the following heuristic argument. Suppose that at $t = t_0$ some fraction Q_0 of the electron charge is trapped in the well region (of width a). Let's denote with Δt the time between two successive impacts upon the confining barriers of this trapped charge (which is assumed to move as a classical particle with momentum $k_r = (2m^*E_r/\hbar^2)^{1/2}$, i.e. $\Delta t = m^*a/\hbar k_r$. After each collision, the wave packet has a probability T_s to tunnel out (either to the right or to the left of the barriers), T_s being the *single* barrier transmission coefficient (6.11). After the time $t = n\Delta t \ \ (n \gg 1)$ the trapped charge is reduced to

$$Q_t = Q_0(1 - T_s)^n \sim Q_0(1 - nT_s) = Q_0(1 - \frac{t}{\Delta t}T_s) \simeq Q_0 e^{-t/\tau_0} \qquad (6.21)$$

where

$$\tau_0 = \Delta t/T_s = (m^*a/\hbar k_r)(1/T_s) \qquad (6.22)$$

We note that if we use in (6.22) the WKB expression for the single barrier transmission coefficient $T_s \simeq exp(-2K_r d)$, we obtain the result (6.20), i.e. $\tau_0 = \hbar/\Delta E$, where ΔE is the width of the resonance evaluated in the same approximation[3].

Very recently the tunneling escape rate from a Quantum Well in Double Barrier hetero-structures where determined by time-resolved photoluminescence experiments [118] and found to agree fairly well with the lifetime as given by (6.20).

[3]We recall that the WKB approximation for the transmission coefficient T_d of a DB structure made of two equal barriers of thickness d separated by a distance a is given by [116] $T_d \simeq (\Delta E/2)^2/[(E - E_r)^2 + (\Delta E/2)^2]$, where $\Delta E = (\hbar^2 k_r/m^*a)exp(-2K_r d)$.

Chapter 7

Time-dependent tunneling in a transverse magnetic field.

7.1 Introduction.

Studies of electron tunneling in the presence of a transverse magnetic field are of great current interest [130,132,133,134,135,136]. Particularly, the recent availability of ultra-low semiconductor barriers of thickness comparable with the semi-classical radius $l_B \equiv (\hbar c/|e|B)^{1/2} \sim 256/\sqrt{B}\,\mathring{A}$ (B in $Tesla$) [130,131] is raising new questions concerning the way in which the field can influence the tunneling dynamics.

In the following, we perform a numerical study of the three-dimensional time-dependent tunneling of a localized electron wavepacket through a thick barrier in the presence of a transverse magnetic field. Although the system studied is highly idealized, our results provide an intuitive picture of the packet evolution which should become useful for later applications in the more complex context of, e.g., tunneling with dissipation, tunneling in hetero-structures, etc.

7.2 Model.

The simplest way to describe an electron tunneling through semiconductor heterostructures is to resort to an Effective Mass approach, in which all references to the microscopic structure of the host semiconductors are condensed in effective masses and band-edge energies[138]. The effect of a magnetic field, when

the magnetic length l_B is much larger than the crystal periodicity, can be included in a standard way. The Hamiltonian of a (spinless) particle, of effective mass m^* and charge e, subject to a constant and uniform transverse magnetic field $\mathbf{B} = B\hat{\mathbf{z}}$, can be written as

$$\hat{H} = \frac{1}{2m^*}(\mathbf{p} - \frac{e}{c}\mathbf{A})^2 + V_b(x) \tag{7.1}$$

where $\mathbf{A}$ is the vector potential and $V_b(x)$ represents a simple square potential barrier of width d and height V_0 centered at x_c :

$$V_b(x) = \begin{cases} V_0 & \text{if } |x - x_c| \leq d/2 \\ 0 & \text{otherwise} \end{cases} \tag{7.2}$$

This is the simplest way to describe the barrier potential felt, for instance, by an electron propagating across an epitaxial semiconductor hetero-structure like an undoped GaAs/AlGaAs/GaAs system, the discontinuity in the potential being determined in this case by the different line-up of the conduction band-edges of the two material making up the structure (see Chapter 1 of this thesis for a general discussion of the electronic properties of semiconductor heterostructures). We note that, in writing (7.1), we have implicitly assumed the same effective mass inside and outside the barrier region: this can be justified, for instance, in the case of a GaAs/GaAlAs boundary with a low Al concentration, in which case $m^* \simeq 0.067\, m_0$ (m_0 being the bare electron mass).

The two most common choices of gauge for studying the motion in the field $\mathbf{B}$ are either the Landau, $\mathbf{A} \equiv \mathbf{A_L} \equiv (0, Bx, 0)$, or the symmetric gauge, $\mathbf{A} \equiv \mathbf{A_S} \equiv \frac{1}{2}(-By, Bx, 0)$, where $\mathbf{A_S} = \mathbf{A_L} - \frac{1}{2}B\nabla(xy)$. In both cases the motion along z reduces to free particle motion, $\sim \exp ik_z z$, which can be factorized out. For each k_z we are thus left with a 2-D hamiltonian, namely

$$H_L = \frac{1}{2m^*}p_x^2 + \frac{1}{2m^*}(p_y - \frac{eB}{c}x)^2 + V_b(x) \tag{7.3a}$$

in the Landau gauge or

$$H_S = \frac{1}{2m^*}(p_x + \frac{eB}{2c}y)^2 + \frac{1}{2m^*}(p_y - \frac{eB}{2c}x)^2 + V_b(x) \tag{7.3b}$$

in the symmetric one. Eq.(7.3b) can be rewritten as:

$$H_S = \frac{1}{2m^*}(p_x^2 + p_y^2) + \frac{1}{8}m^*\omega_c^2(x^2 + y^2) - \frac{1}{2}\omega_c L_z + V_b(x) \tag{7.4}$$

where $L_z \equiv xp_y - yp_x$ is the z-component of the angular momentum and $\omega_c \equiv eB/m^*c$ is the cyclotron frequency. Note that when $V_b = 0$, H_S as given by (7.4) is the Hamiltonian of a 2-D isotropic harmonic oscillator of frequency $\omega_c/2$ [139]. The energy spectrum of (7.1)- which is of course independent of the choice of the gauge - is shown in Fig.I.1 in Appendix I, for a particular set of parameters m^*, V_0, d and B which will be used in the following in the study of time-dependent tunneling. This spectrum can be most easily calculated using the Landau gauge, since in this case also the motion along y reduces to free-particle motion, leading to an effective one-dimensional hamiltonian. The characteristic features of such spectrum are discussed in details in Appendix I.

In order to study the dynamics of tunneling in the presence of B, we need to solve the time-dependent Schrödinger equation associated with either H_L or H_S using a wavepacket description of the initial electron state. For this we use the standard two-dimensional Gaussian wavepacket

$$\Psi_0 \equiv \Psi(\mathbf{R}; t = 0) = (2\pi\sigma^2)^{-1/2} e^{-\mathbf{R}^2/4\sigma^2} e^{i\mathbf{k}_0 \cdot \mathbf{R}} \tag{7.5}$$

which for the sake of simplicity we assume to be centered at the origin of our gauge. The choice of a gaussian wavepacket is convenient since it allows a simple comparison with both limiting cases of zero field with $V_b \neq 0$, and $B \neq 0$ with $V_b = 0$. We remark that in the symmetric gauge the packet which evolves from (7.5) in the case $V_b = 0$ does always maintain the circular shape of the initial state (see Sect.7.7). The same would of course apply to the Landau gauge (or any other gauge) after multiplication of Ψ_0 by a suitable phase factor and all calculations could equally well be carried out there. In the Landau gauge in particular, calculations would be somewhat simpler because the Hamiltonian (7.3a) contains, beyond the kinetic energy operator, one additional non-local term (xp_y) instead of the two (xp_y and yp_x) which appear in (7.3b). However, the difference is not very relevant at the numerical level. Here we choose the symmetric gauge where the evolution of (7.5) corresponds more closely to our physical intuition of a particle moving along a cyclotron orbit in a transverse field, as shown in Fig.7.4 in Sect.7.6.

7.3 Solving the time-dependent Schrödinger equation.

Recently, a large amount of dynamical simulations of quantum systems using spectral grid methods have been performed (for recent reviews see, for instance, Ref.[140] and Ref.[141]). A typical procedure based on such methods requires basically three steps: (i) the wave function at time $t = 0$ is represented on a discrete spatial grid, whose size and shape have to be adapted to the particular physical problem; (ii) the Hamiltonian operator $\hat{H}$ and its action on the wave function $\hat{H}\Psi$ are calculated; (iii) a time propagation scheme is constructed which transforms the initial wave function Ψ_0 into the final one $\Psi(t)$. These points are discussed in some detail below.

(i) Because of the finite size of the grid, the initial wave function must be localized in space. We choose here the popular Gaussian wavepacket, given by (7.5). This represents a particle localized about the origin with a r.m.s. deviation σ and localized in momentum space about $\mathbf{k}_0$ with a r.m.s. deviation $1/\sigma$, as can be seen from the expression of its Fourier transform

$$\tilde{\Psi}_{k_0}(\mathbf{k}) = (2\sigma^2/\pi)^{1/2} e^{-\sigma^2(\mathbf{k}-\mathbf{k}_0)^2} \tag{7.6}$$

Boundary conditions on the grid are an important issue. Since we use the Fourier method to calculate spatial derivatives, we are restricted to periodic boundary conditions. For a problem, like the one associated with the Hamiltonian (7.4), where the spectrum is discrete (i.e., only bound states) all unwanted interferences of a wave function with its own periodically repeated tail can be eliminated by expanding the grid size. The price is that a portion of the grid is devoted only to the elimination of these interferences.

When choosing the size of the "box" where the motion of the wavepacket takes place, one should also take into account the fact that a Gaussian packet of width σ_0, moving in free space, spreads in the course of time, according to the law [143] $\sigma(t) = \sigma_0(1 + \hbar^2 t^2/4m^{*2}\sigma_0^4)^{1/2}$: the smaller the initial uncertainty in position σ_0, the larger the uncertainty in momentum and the more rapidly the packet spreads. This poses also a limit to the time duration of the simulation and in particular for the study of tunneling problems, it can make difficult to calculate the wavepacket transmission coefficients for low values of the energy of the incident packet, due to the longer time required for the "asymptotic" separation of the transmitted and reflected parts to take place (see Sect.7.5).

One should also take care to place the initial packet sufficiently far from the front of the barrier in order to minimize the production of high-frequency harmonics due to the truncation of the wavepacket at the interface [127].

The grid must be dense enough to sample the highest momentum components of the wave function: the interval Δ_i $(i = x, y)$ between grid points is determined by the maximum momenta $P_{i,max}$ which can occur in each of the two spatial directions, through $\Delta_i = \pi/P_{i,max}$. The choice of the mesh thus depends critically on the particular values of the initial parameters (energy and spread of the packet, shape of the potential, etc.). As a crude rule of thumb, one could take $\Delta_i \lesssim \pi/(k_{0i} + 1/\sigma)$.

When using Fourier transform techniques, it is more convenient, from the computational point of view, to model a discontinuous potential like (7.2), whose Fourier transform has a slow convergence rate with the size of the grid in k-space, with a a "softer" potential profile. We used in our calculations a combination of Fermi functions of the form

$$V_b(x) = V_0\Big[\frac{1}{exp[(x - x_c - d/2)/\delta] + 1} - \frac{1}{exp[(x - x_c + d/2)/\delta] + 1}\Big] \qquad (7.7)$$

with a suitably chosen value for the grading parameter δ (see Sect.7.5).

(ii) The strategy is to calculate the action on Ψ of each operator in the Hamiltonian $\hat{H}$ *locally* in coordinate space. Both the kinetic energy and angular momentum operator in the Hamiltonian (7.4) are non-local, i.e. they contain derivatives with respect to the coordinates. However, one can use the property of the Fourier transforms that a derivative in direct space becomes a multiplication by ik in reciprocal space. The use of the Fast Fourier Transform (**FFT**) algorithm immensely improves the numerical efficiency of these operations, as a result of the scaling properties of the FFT algorithm which are of order $NlnN$, N being the number of points in the grid.

(iii) Once the initial wave function Ψ_0 has been set-up on the grid, the next step consists in propagating this wave function in time. Whenever the Hamiltonian of the system doesn't contain explicitly the time, the general solution of the Schrödinger equation at any time t can be obtained from the knowledge of the wave function Ψ_0 at $t = 0$ using $\Psi(t) = \hat{U}\Psi_0 \equiv exp(-i\hat{H}t/\hbar)\Psi_0$. The Chebychev scheme [137], that we adopt in our calculations, is based upon a suitable polynomial expansion of the time-evolution operator $\hat{U}$. This scheme has proven to be more efficient and accurate than other methods. When combined with the Fourier method for calculating the kinetic energy operator and

other non-local operators in the Hamiltonian [144], the Chebychev method has the advantage of a slow increase in numerical effort with the increase in the size of the problem (for a critical comparison between this and other commonly used time-dependent methods, see Ref.[141] and in particular the Table II therein, where the scaling properties of different approaches are compared). One drawback of the Chebychev scheme is that it cannot be used with Hamiltonians which have an explicit time-dependence. The basic ingredients of the method are contained in Appendix K.

7.4 Testing the method for a simple tunneling problem.

We used, as a numerical test of the Chebychev approach in solving the time-dependent Schrödinger equation, the archetypal scattering problem of a wavepacket from an ideal square potential barrier of the form (7.2). The stationary states of this problem have been discussed in Section 6.1.

In this test-calculation a Gaussian wavepacket of the type (7.5) is scattered by a simple square barrier, which is placed in the center of a "box" of side $L = 6000\,\mathring{A}$. We show in the panels of Fig.7.1 the charge density $|\Psi(t)|^2$ (represented by means of contours of equal height [1]) at different times, for a typical choice of the packet and barrier parameters (see the Figure caption). The dash-dot line represents the classical trajectory that the packet would have traced in the absence of the barrier. One sees clearly (panel 3) that the transmitted packet appears to the right of the barrier *before* the maximum of the incident wavepacket reaches the left edge of the barrier. The resulting delay in the transmission is a well-known fact [123,145] and in the limiting case of (infinitely) extended wavepacket it is described in terms of the stationary-phase time introduced by Wigner[146]. We postpone the discussion of the delays introduced by the barrier, without and with magnetic field, to Sect.7.9. Curiously enough, the fourth panel of Fig.7.1 shows quite clearly that a "specular" image of the transmitted packet appears among the wiggles of the reflected packet to the left of the barrier. Note also the appreciable deviation of the transmitted packet from its initial circular shape.

[1] Since the barrier considered here is rather thick, a logarithmic scale is used in drawing the contour plots of Fig.7.1 in order to enhance the weak features associated with the tiny transmitted wavepacket.

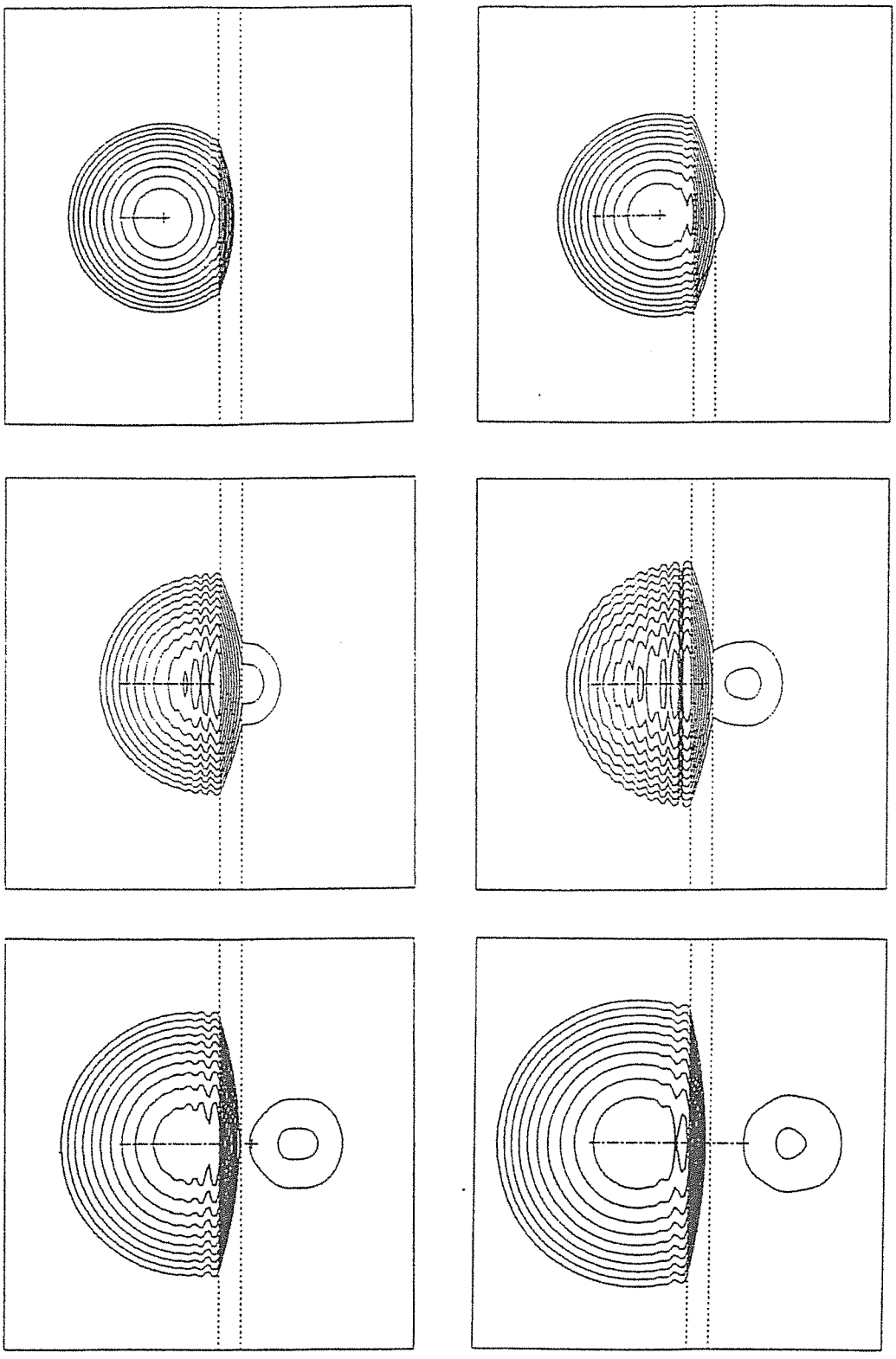

Figure 7.1:
Logarithmic contour plots of the charge density $|\Psi(t)|^2$ for the scattering of a gaussian wavepacket of width $\sigma = 210\,\mathring{A}$ by a square barrier of height $V_0 = 0.06\,eV$ and thickness $d = 328\,\mathring{A}$. At $t = 0$ the wavepacket is to the left of the barrier moving towards it with an energy $E_0 = 0.021\,eV$. The first snapshot is taken at $t = 0.2 \times 10^{-12}\,s$ and the subsequent ones are taken every $0.1 \times 10^{-12}\,s$. The dash-dot line shows the wavepacket trajectory in the absence of the barrier.

We want to compare the effective transmission coefficients, as obtained numerically from our time-dependent simulations, with the corresponding exact values, for several energies of the incident wavepacket E_0, either lower and higher than the top of the barrier V_0. The exact wavepacket transmission coefficient can be calculated as follows.

For a single Fourier component of wave vector k, the transmission coefficient T for a square-barrier may be found exactly by standard wave-function matching across the barrier boundaries and is given by [102]:

$$T = \frac{4k^2K^2}{4k^2K^2 + (K^2 - k^2)^2 sin^2(Kd)} \tag{7.8}$$

where $k = \sqrt{2m^*E_0/\hbar^2}$ and $K = \sqrt{2m^*|V_0 - E_0|/\hbar^2}$ are the wave vectors outside and inside the barrier region respectively. The above expression for T is valid if $E_0 > V_0$: when $E_0 < V_0$, the replacement $K \longrightarrow iK$ has to be made in (7.8). The effective transmission probability T_{eff} for the wavepacket can be found using its Fourier representation

$$\Psi(x; t = 0) = \frac{1}{\sqrt{2\pi}} \int_{-\infty}^{+\infty} \tilde{\Psi}_{k_0}(k) e^{ikx} dk \tag{7.9}$$

where $\tilde{\Psi}_{k_0}(k)$ is the one-dimensional version of (7.6). At time t, an expression for the transmitted part can be obtained by propagating independently each of the plane waves in (7.9) according to $e^{ikx} \longrightarrow \sqrt{T(k)} e^{i\Delta\phi(k)} e^{-ikd} e^{ikx}$, ($\Delta\phi(k)$ being the phase increase across the barrier), and by appending to these stationary-state solutions the appropriate time factor, i.e.

$$\Psi_{trans}(x, t) = \frac{1}{\sqrt{2\pi}} \int_{-\infty}^{+\infty} \tilde{\Psi}_{k_0}(k) \sqrt{T(k)} e^{i\Delta\phi(k)} e^{-ikd} e^{ikx} e^{-iE(k)t/\hbar} dk \tag{7.10}$$

Here $E(k) = \hbar^2k^2/2m$ and $T(k)$ is understood to be zero when $k < 0$. If we *define* the wavepacket transmission coefficient T_{eff} as

$$T_{eff} = \int_{-\infty}^{+\infty} |\Psi_{trans}(x, t = +\infty)|^2 dx \tag{7.11}$$

one finds immediately:

$$T_{eff} = \int_{-\infty}^{+\infty} |\tilde{\Psi}_{k_0}(k)|^2 T(k) dk \tag{7.12}$$

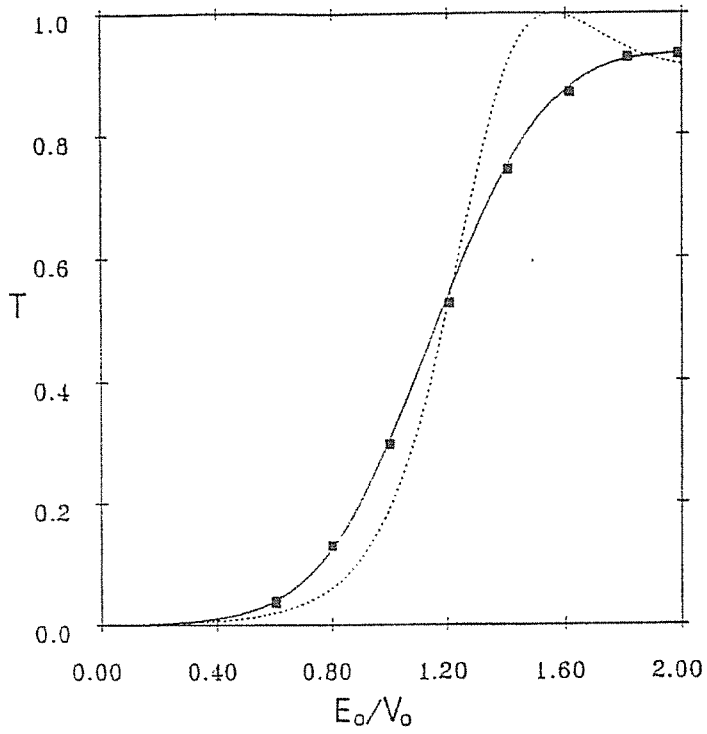

Figure 7.2:

Dotted line: plane-wave transmission coefficient (Eq.(7.8) in the text);
solid line: exact transmission coefficient (calculated form Eq.(7.12) in the text) for a packet with $\sigma = 100\ \mathring{A}$;
squares : numerical results from our calculations, for the same wavepacket.

We compare in Fig.7.2 our results (indicated with squares) with the exact T_{eff} from Eq.(7.12)(solid line): the agreement appears to be very good. We also show in the Figure, with a dotted line, the plane wave result (7.8), to which T_{eff} is expected to coalesce in the limit of an infinitely extended wavepacket. The numerical results in Fig.7.2 are obtained by following the time-development of the packet as it moves into and out of the barrier region, ultimately splitting into a reflected Ψ_{refl} and a transmitted packet Ψ_{trans}. In particular, the numerical transmission coefficient is calculated by integrating the squared modulus of the transmitted wave function as in Eq.(7.11). We have done a single-step calculation for each value of E_0/V_0 using a time t long enough to have a complete separation of the incident packet into well defined transmitted and reflected parts, still contained within L. The calculations are performed using a 256-points grid, out of which 10 are used to discretize the barrier. The latter has the form (7.7), with $\delta \sim 2\,\mathring{A}$. We use $L = 2700\,\mathring{A}$, corresponding to a grid spacing $\Delta X \simeq 10\,\mathring{A}$. The width of the wavepacket is $\sigma = 100\,\mathring{A}$ and the barrier is $100\,\mathring{A}$ thick and $0.1\,eV$ high. The energy at the end of each run is conserved to better than $1/10^7$ and the same deviations of the norm of the propagated wave functions from unity are found. Roughly an order-of-magnitude higher errors are found using a 128-points grid.

7.5 Choice of the wavepacket width.

The use of localized wavepackets implies a finite-width distribution of momenta about the average initial value k_0. Since the Fourier components of energy higher than the top of the barrier will propagate through the latter as free particles, eventually masking the effects due to "pure" tunneling, we must require the portion of the transmitted packet whose plane wave components have energies above the top of the barrier ("over-the-barrier" part T_{over}) to be much smaller than the "under-the-barrier" part T_{under} . In one dimension these are defined as (compare with Eq.(7.12))

$$T_{over} = \int_{k_M}^{+\infty} T(k)|\tilde{\Psi}_{k_0}(k)|^2 dk \quad , \; T_{under} = \int_0^{k_M} T(k)|\tilde{\Psi}_{k_0}(k)|^2 dk \qquad (7.13)$$

where $k_M = \sqrt{2m^* V_0/\hbar^2}$ and k_0 is the wave vector of the incident packet. It is easy to show that the condition $T_{over} \ll T_{eff} \equiv (T_{over} + T_{under})$ implies, in the

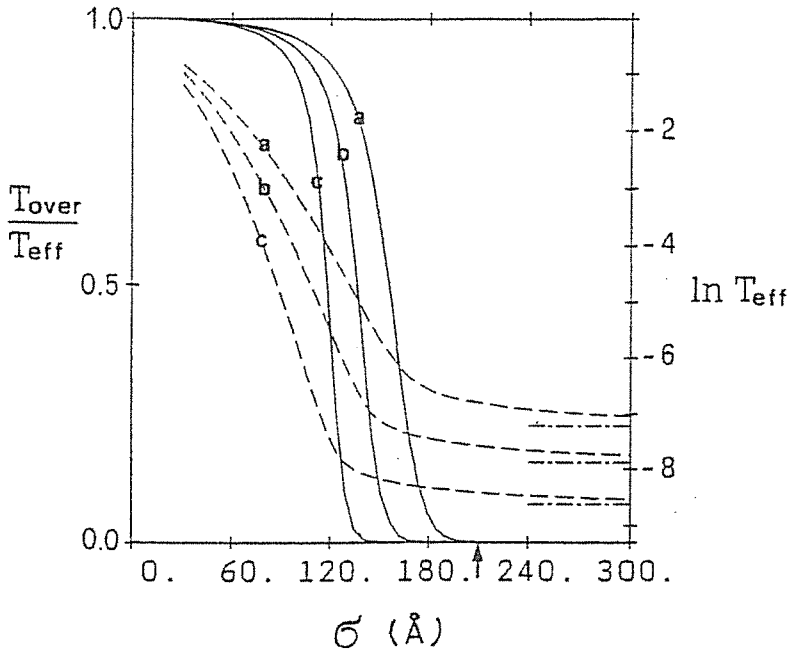

Figure 7.3:
Ratio T_{over}/T_{eff} (solid lines) and transmission coefficient T_{eff} (dashed lines) vs. wavepacket width σ, for three different values of the incident energy (a) $E_0/V_0 = 0.1$, (b) $E_0/V_0 = 0.2$ and (c) $E_0/V_0 = 0.3$. The dash-dot lines show the plane-wave transmission coefficient for the same energies. The barrier parameters are the same of Fig.7.1 and Fig.I.1. The arrow shows the value of σ which is used in subsequent calculations.

case of a very "opaque" barrier $dk_M \gg 1$, that

$$\sigma^2(k_M - k_0)^2 \gtrsim d(k_M^2 - k_0^2)^{1/2} \tag{7.14}$$

This is a severe constraint which poses, for fixed barrier parameters and incident energy E_0, a lower limit to the possible values of the width σ of the incident wavepacket. We show in Fig.7.3 with solid lines the value of the ratio T_{over}/T_{eff}, calculated directly from (7.13), versus σ for three values of the incident a-dimensional energy E_0/V_0. The arrow indicates the value of the wavepacket width which we used in our two-dimensional calculations in the following Sections. It appears from Fig.7.3 that, although for small values of σ the transmitted part is dominated by the over-the-barrier contribution, there is a quite sharp transition to the domain of "pure" tunneling in which the ratio T_{over}/T_{eff} is almost zero.
The dependence of T_{eff} on σ is also shown in the figure (with dashed lines)

for the same values of E_0/V_0: one can sees that in the region of pure tunneling the effective transmission coefficient is well approximated by the plane-wave expression (7.8), shown with dash-dot lines.

7.6 Free motion of a wavepacket in a transverse magnetic field.

Since the Hamiltonian (7.4), in the absence of the barrier, is a quadratic form in the coordinates (x, y) and the conjugate momenta (p_x, p_y), the Ehrenfest equations for the time dependence of the average values $< x >$, $< y >$, $< p_x >$ and $< p_y >$ coincide with the classical Hamilton's canonical equations. The latter can be solved exactly (as shown in Appendix J) and one finds, as expected on classical grounds, that the resulting average trajectory of the wavepacket in the $x - y$-plane is periodic (of period $2\pi/\omega_c$) and runs through a circular path (whose center and radius are determined by the initial values x_0, y_0, p_{0x}, p_{0y}).

As far as the shape of the wavepacket during its motion is concerned, we found that a gaussian wavepacket of the form (7.5), of width σ_0, while tracing its circular trajectory under the action of the magnetic field, executes a symmetrical "breathing" oscillation of period $T = 2\pi/\omega_c$. However, when $\sigma_0 = l_B$ ($l_B = (\hbar c/eB)^{1/2}$ being the magnetic radius) the packet *coheres*, i.e. it doesn't spread during its motion. This is simply because in that case it represents the stationary-state solution of the 2D-harmonic oscillator Hamiltonian to which (7.4) reduces in the absence of the barrier potential $V_b(x)$. If $\sigma < l_B$, the wavepacket spreads in half a period to a maximum value $\sigma_{T/2}$, such that $\sigma_0\sigma_{T/2} = l_B^2$. During the remaining half-period it shrinks back to σ_0. In the opposite case, when $\sigma > l_B$, the wavepacket will shrink to $\sigma_{T/2} = l_B^2/\sigma_0$ during the first semi-period and then it will recover its initial size σ_0 at time t=T. We found that this periodic oscillations in width follow the simple law:

$$\sigma(t) = \sigma_0\Big[cos^2(\frac{\omega_c t}{2}) + (l_B/\sigma_0)^4 sin^2(\frac{\omega_c t}{2})\Big]^{1/2} \qquad (7.15)$$

We quote, for comparison, the exact result for the time-development of a *one-dimensional* Gaussian wavepacket $\Psi_0 \sim exp(-x^2/4\sigma_0^2)$ subject to an harmonic potential $V = \frac{1}{2}m^*\omega_c^2 x^2$. In this case, the probability density at time t is described by $|\Psi(t)|^2 \propto exp[-x^2/2\sigma^2(t)]$, where [147]

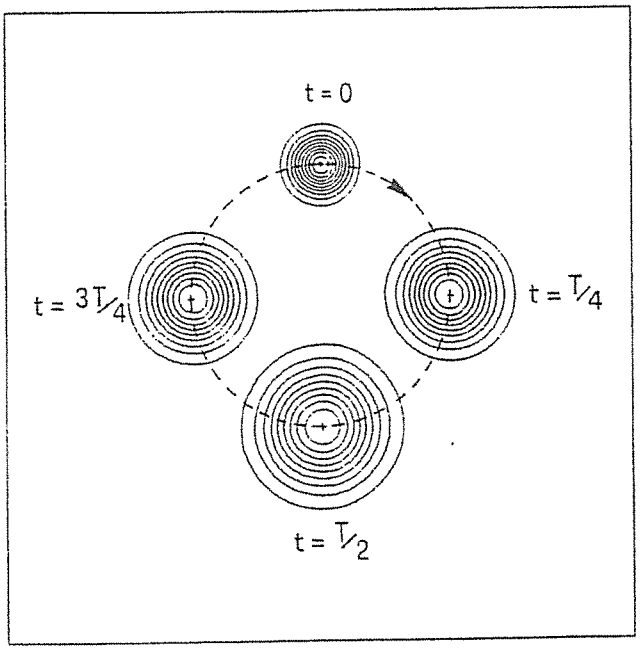

Figure 7.4:
Time evolution of a gaussian wavepacket of width σ less than the magnetic length l_B at $B = 1\,T$ ($\sigma = 180\,\mathring{A}$, $l_B = 256\,\mathring{A}$). At $t = 0$ the packet is placed in the origin with momentum parallel to the horizontal axis. The period is $T = 2\pi/\omega_c = 2.4 \times 10^{-12}\,s$. The dashed line shows the wavepacket trajectory as obtained from the equations of motion of Appendix J.

$$\sigma(t) = \sigma_0\Big[cos^2(\omega_c t) + (l_B/2\sigma_0)^2 sin^2(\omega_c t)\Big]^{1/2} \tag{7.16}$$

We show in Fig.7.4 the free motion of a wavepacket with $\sigma = 180\,\mathring{A}$ in a magnetic field $B = 1$ Tesla ($l_B = 256\,\mathring{A}$) during a period of the motion. The dashed line shows the packet trajectory, as obtained from the solutions of the equations of motion (Eq.(J.2) in Appendix J).

7.7 Tunneling in a transverse magnetic field.

We present in this Section some results from our numerical simulations of the model system described in Sec.7.2. In particular, we consider the case of the scattering from a rather thick barrier of wavepackets with $\sigma \sim d \sim l_B$. In the following we will focus mainly on the time-behavior of two quantities, the

charge density $|\Psi(t)|^2$ and the current density j. The latter is given by [148]:

$$\mathbf{j}(t) = \frac{e\hbar}{m^*} Im\Big[\Psi(t)^* \nabla \Psi(t)\Big] - \frac{e^2}{m^* c} \mathbf{A} |\Psi(t)|^2 \qquad (7.17)$$

The results presented in the following refer to the case of a circular gaussian wavepacket of width $\sigma = 210 \mathring{A}$ which is scattered by a square barrier ($d = 328 \mathring{A}$, $V_0 = 0.06\, eV$) in a magnetic field of strength $B = 1$ Tesla ($l_B = 256\, \mathring{A}$). The wavepacket is placed at $t = 0$ in the origin, to the left of the barrier (which is indicated with dotted lines in the figures) and the momentum k_0 is such that the energy is $E_0 = 0.35\, V_0$. The spread in energy of the packet is roughly $\Delta E = \hbar^2 k \Delta k / m^* \simeq 10\, meV$, where $\Delta k \sim 1/\sigma$. All the calculations are performed on a 256×256-points square grid of side $L = 6000\, \mathring{A}$.

We show in the sequence of plots of Fig.7.5, Fig.7.6 and Fig.7.7 the charge $|\Psi(t)|^2$ and the current density j at different times. The charge density is represented by means of contours of equal height while the current density is represented in modulus and direction on a 18×18 grid covering the square window drawn in each panel of Fig.7.5. Since we used a relatively thick barrier, the part of the wave function which finally tunnels out of it is very small ($10^{-5} \div 10^{-7}$ of the total wave function). The very weak features associated with that transmitted part are enhanced in Fig.7.5, Fig.7.6 and Fig.7.7 using a logarithmic scale both for $|\Psi|^2$ and j: for example, values corresponding to adjacent contour lines of Fig.7.5 and Fig.7.7 differ roughly by one order of magnitude.

From the sequence of Fig.7.5 we see that, as the packet impinges on the barrier, becomes heavily deformed, and finally gives rise to a large reflected and a tiny transmitted packet. These two packets, both different from Gaussian, subsequently evolve with opposite curvatures, as required by their oppositely directed $< k_x >$. The trajectories of the transmitted and reflected parts (drawn with dashed and dotted lines in the last panel of Fig.7.5) are obtained by best-fitting with a circular path the average values $< x >$ and $< y >$ as obtained from the numerical wave functions. In practice we calculated $< x >$ and $< y >$ at different times between $t = 0.7$ and $t = 1.2 \times 10^{-12}\, s$, when the separation between the transmitted and reflected packets already took place. The dash-dot line represents the path that the particle would have traced in the absence of the barrier, as obtained from the solution of the equations of motion (see Appendix J). The current pattern inside the packet-barrier collision area is shown in Fig.7.6. One notable feature of this pattern is the generation of strong downwards currents at and below the barrier edge. This currents, associated

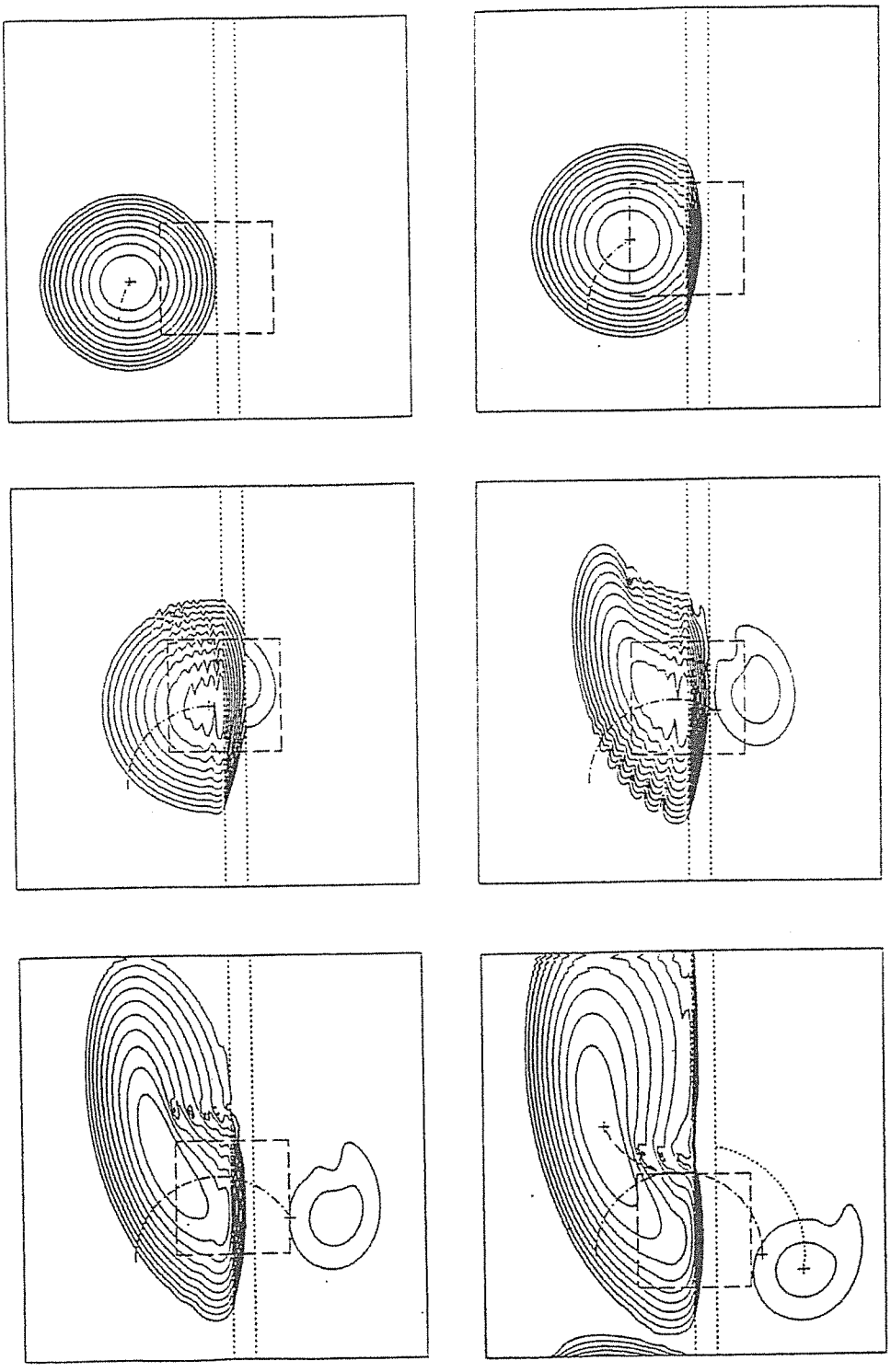

Figure 7.5:
Logarithmic contour plots of the charge density $|\Psi(t)|^2$ for the scattering of a gaussian wavepacket by a thick barrier in a magnetic field $B = 1\,T$. The barrier and packet parameters are the same of Fig.7.1. The snapshots are taken every $0.2 \times 10^{-12}\,s$. In the last panel the best-fit trajectories of the transmitted (dotted line) and the reflected (dashed line) part are shown. The dash-dot line is the trajectory in the absence of the barrier. The square windows refer to Fig.7.6.

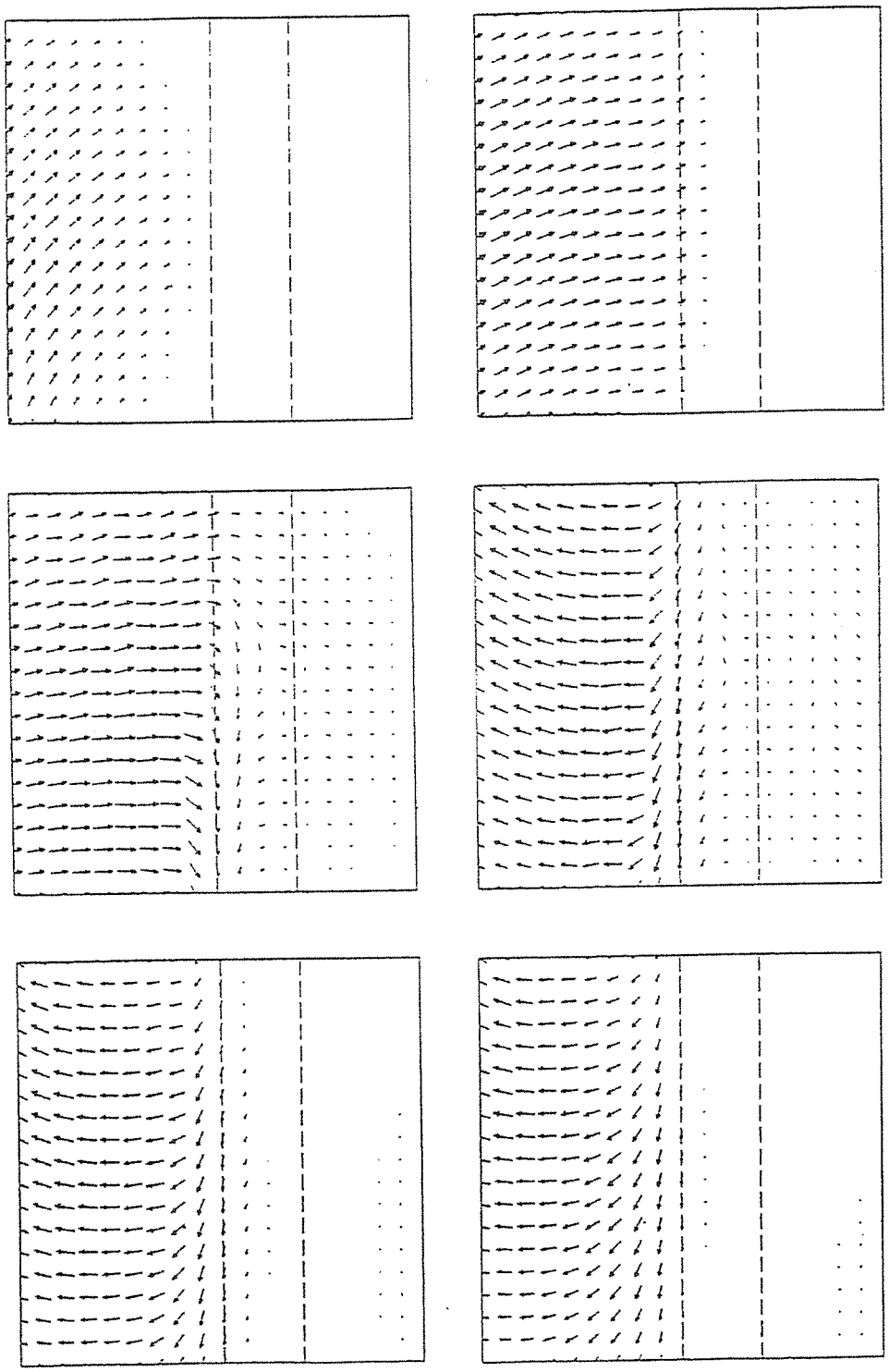

Figure 7.6:
Current density $\mathbf{j}(x, y)$ for the scattering process shown in Fig.7.5. The current is represented in magnitude and direction on a 18×18 grid covering the windows drawn with dashed lines in each panel of Fig.7.5.

with the diamagnetic term in Eq.(7.17) persist in fact for a longer time, giving rise to the large y-spreading of the packet visible in Fig.7.5 and 7.7.

From the radii of curvature of the best-fit trajectories we immediately obtain, using Eq.(J.3) in Appendix J, the average momentum of the reflected and of the transmitted wavepackets. We compare these values with the *zero-field* exact results for the average values $<k>_{refl}$ and $<k>_{trans}$, defined as

$$<k>_{trans} \equiv \frac{<\Psi_{trans}|k|\Psi_{trans}>}{<\Psi_{trans}|\Psi_{trans}>} = \frac{\int k|\tilde{\Psi}_{k_0}(k)|^2 T(k)dk}{\int |\tilde{\Psi}_{k_0}(k)|^2 T(k)dk} \qquad (7.18a)$$

and

$$<k>_{refl} \equiv \frac{<\Psi_{refl}|k|\Psi_{refl}>}{<\Psi_{refl}|\Psi_{refl}>} = \frac{\int k|\tilde{\Psi}_{k_0}(k)|^2 [1-T(k)]dk}{\int |\tilde{\Psi}_{k_0}(k)|^2 [1-T(k)]dk} \qquad (7.18b)$$

where k_0 is the momentum of the incident wavepacket. We note in passing that, from (7.18a), (7.18b) and (7.12), one can derive the relation

$$k_0 = <k>_{trans} T_{eff} + <k>_{refl} (1 - T_{eff}) \qquad (7.19)$$

which is a generalized "momentum-conservation" equation for a tunneling process.

By evaluating explicitly (7.18a) and (7.18b), one sees that the zero-field momentum $<k>_{trans}$ is always higher than k_0, while $<k>_{refl}$ is lower: this is because the plane-wave transmission [reflection] coefficient for a single barrier is a monotonically increasing [decreasing] function of the momentum and thus displaces the distribution of velocities of the transmitted [reflected] packets to higher [lower] momenta[123]. For very thick barriers this "filtering" effect is significant only for the transmitted part (if $T_{eff} \ll 1$ one has, from (7.19), $<k>_{refl} \sim k_0$) and the thicker the barrier the higher the displacement of $<k>_{trans}$ towards higher momenta. In our case we find, using Eq.7.18a and 7.18b, $<k>_{trans} \simeq 1.20\, k_0$ and $<k>_{refl} \simeq k_0$. These numbers should be compared with the average momenta at $B \neq 0$ obtained from the radii of curvature of the wavepackets, $<k>^B_{trans} \simeq (1.30 \pm 0.04)\, k_0$ and $<k>^B_{refl} \simeq (0.95 \pm 0.04)\, k_0$ [2]. We see that, as an effect of the magnetic field, there is an additional shift in $<k>^B_{trans}$ and $<k>^B_{refl}$ with respect to the zero-field values. This can be explained qualitatively in a semi-classical picture by noting that, due to the Lorentz force, the effective path of the tunneling particle is larger than in the

[2]The error bars have been estimated assuming that the measured $<x>$ and $<y>$ are affected by an uncertainty roughly equal to half the grid spacing.

absence of the field and thus the particle "sees" a thicker effective barrier. It is difficult to make this explanation work quantitatively, however. For instance, by using the effective B-dependent thickness (7.23), which accounts well for the transmission coefficient (see next Section), we would get only $< k >^{B}_{trans} \simeq 1.21$.

The same scattering process of Fig.7.5 is followed, in the sequence of logarithmic plots of Fig.7.7, for much longer times, allowing for multiple reflections from the barrier. Although the packet has spread out very much along y, its maximum appears to be following closely the classical trajectory. During its motion, the wavepacket collides repeatedly with the barrier. At each collision, a new small transmitted wavepacket is generated. Eventually, both the reflecting and the transmitted packets reach the top and bottom boundaries where, because of the lack of $y-$periodic boundary conditions due to the presence of the "magnetic potential" in (7.4), their behavior become unphysical.

We have calculated for each of the configurations in Fig.7.7 the total current, as the integral over the grid of the current density (7.17), i.e.

$$J_i \equiv \int j_i(\mathbf{R}) d\mathbf{R} \qquad (i = x, y) \tag{7.20}$$

The time dependence of J_i/e is shown in Fig.7.8. At $t = 0$ the current is directed along the positive y-axis, by our choice of the initial velocity. The arrow indicate the direction of increasing time. The total current shows a "spiraling" behavior with time, and the spiral gradually converges to a final point that we identify with $J_x = 0$, $J_y \simeq e(2/\pi)\omega_c R_c$ (indicated with a cross on the vertical axis of Fig.7.8). This is the value of the current associated with the classical "skipping" orbit (shown with a dash-dot line in Fig.7.7) obtained by repeated reflections from the barrier edge of the trajectory of the incident wavepacket in the absence of the barrier. A simplified description of the stationary-state edge-currents arising near an interface in a transverse magnetic field is given in Appendix I.

7.8 Dependence of the transmission coefficient on the field strength.

We have performed a set of calculations, for several values of the applied magnetic field B and fixed wavepacket parameters, in order to investigate the dependence of the wavepacket transmission coefficient T_{eff} (defined in (7.11)) on

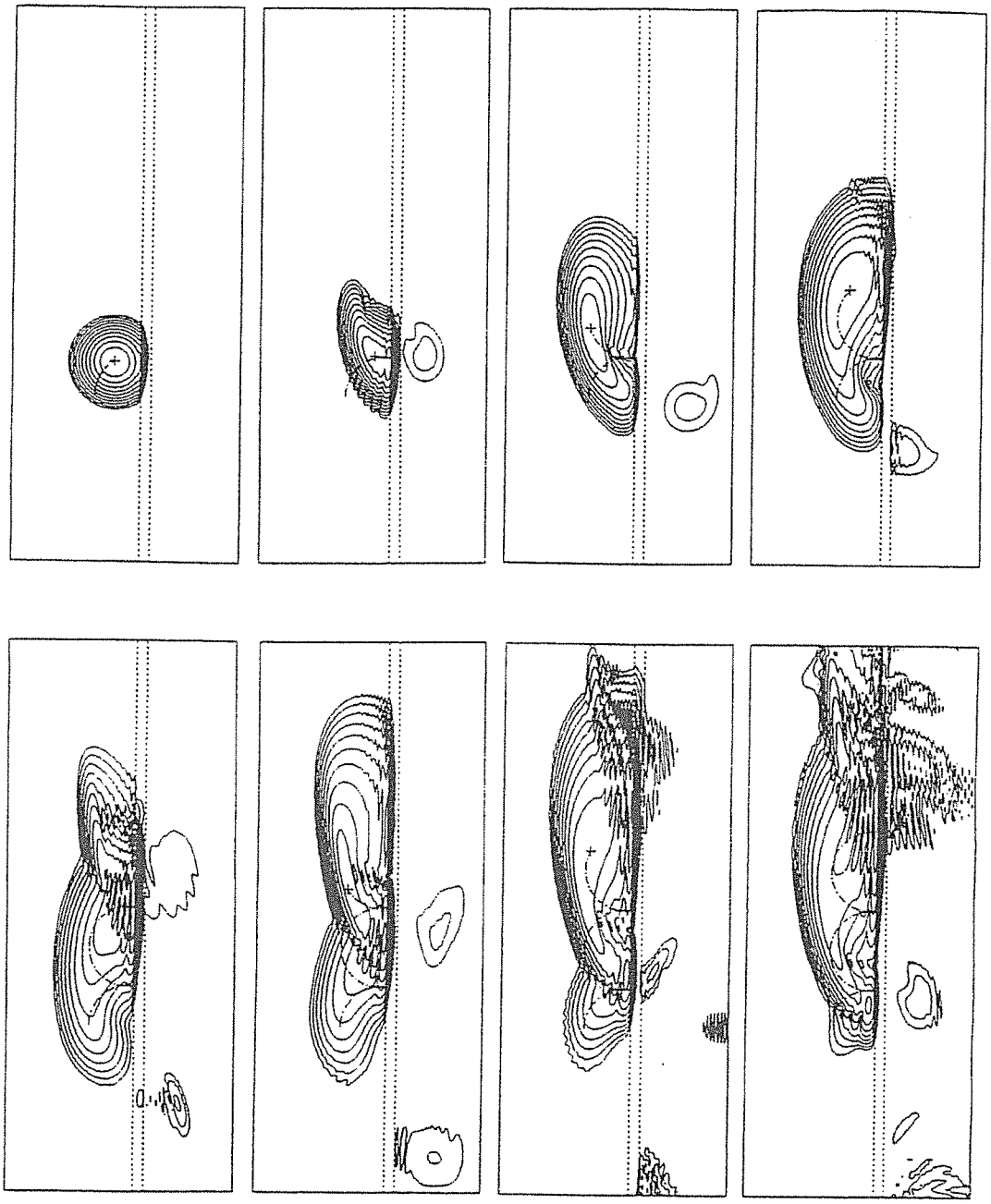

Figure 7.7:
Same scattering process of Fig.7.5, followed for longer times: the snapshots now are taken every $0.4 \times 10^{-12}\,s$. The semi-classical "skipping" trajectory drawn with a dash-dot line is obtained from the wavepacket trajectory in the absence of the barrier by repeated reflections upon the latter. The same logarithmic scale of Fig.7.5 has been used for the contour lines.

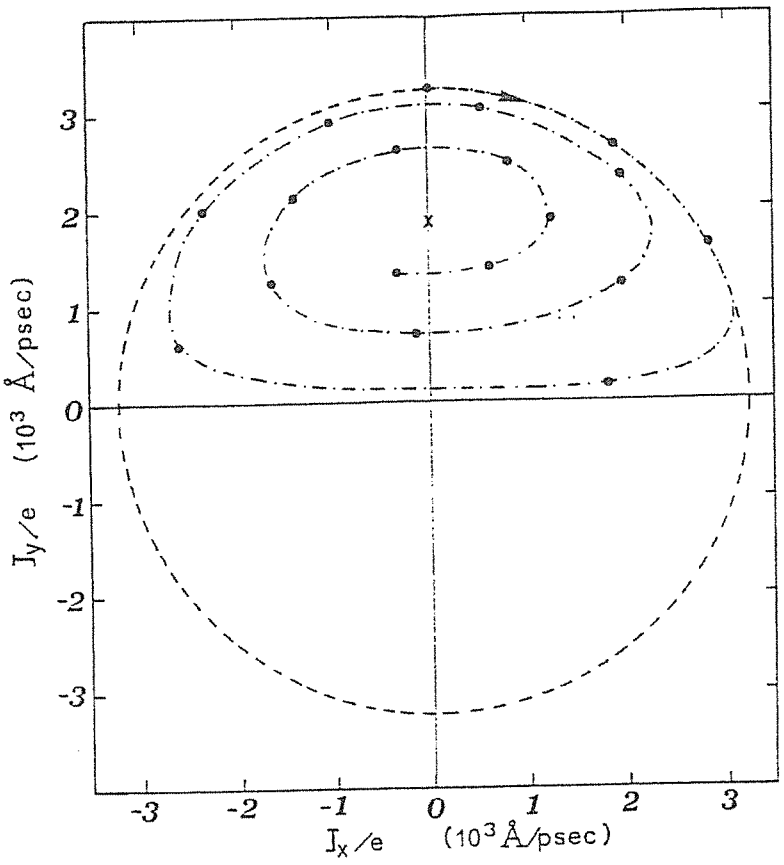

Figure 7.8:
Average velocity J/e (dots) for the scattering process of Fig.7.7: the values are calculated every $0.2 \times 10^{-12}\,s$. The dashed line is the expected trajectory of the packet if the barrier was absent. The arrow indicates the direction of increasing time. The cross on the vertical axis is the value of the "drift" velocity $v_d \simeq (2/\pi)\omega_c R_c$, obtained from the semi-classical skipping orbit of Fig.7.7.

the field strength. Our calculated T_{eff} are shown in Fig.7.9 as a function of B^2, for the case of a wavepacket of width $\sigma = 90\,\AA$ scattered by a square barrier of thickness $d = 94\,\AA$ and height $V_0 = 0.17$ eV. These results are obtained, like in the one-dimensional calculations of Sect.7.4, by propagating the initial wavepacket for a time long enough to have a separation of the incident wavepacket into well defined reflected and transmitted parts and then by integrating numerically the squared modulus of the transmitted part of the wavefunction. The simulations were performed on a 128×128 grid. The arrow shows the zero-field exact transmission coefficient calculated from (7.12).

The observed exponential dependence of T_{eff} on B^2 (see squares on Fig.7.9) can be quantitatively understood within a simple semi-classical approach as follows (we use here the notations of Appendix I). If we assume that the magnetic field effects are confined within the barrier region, and using the zeroth-order WKB expression for the transparency of a potential barrier, we can write

$$T_{eff}(B) \simeq T_{WKB} = exp[-2\int_{x_c-d/2}^{x_c+d/2}\sqrt{2m^*[V_{eff}(x)-E]/\hbar^2}dx] \qquad (7.21)$$

where V_{eff} is given in Eq.(I.3) of Appendix I and E is the average energy of the wavepacket. Expanding the integrand to first order in $m^*\omega_c^2(x-X_0)^2/2(V_0 - E)$, one finds:

$$T_{eff}(B) \simeq T_0 exp[-\frac{e^2B^2l^3}{12c^2\hbar^2K}] \equiv exp[-2Kd_{eff}] \qquad (7.22)$$

where $T_0 \simeq exp(-2Kd)$ is the zero-field WKB transmission coefficient, $K = \sqrt{2m^*(V_0-E)/\hbar^2}$ and $l^3 \equiv d^3 + 12d(X_0 - x_c)^2$. The "cyclotron-orbit center" coordinate X_0 is defined as $X_0 \equiv \hbar k_y c/eB$. The last line of Eq.(7.22) defines an effective barrier thickness d_{eff} as

$$d_{eff} = d + \frac{e^2B^2l^3}{24c^2\hbar^2K^2} \qquad (7.23)$$

Thus the presence of the magnetic field gives rise to a larger effective barrier width, whose origin is qualitatively illustrated in Fig.7.10. The extra "magnetic potential" $(1/2)m^*\omega_c^2(X_0 - x)^2$ in the effective potential V_{eff} in Eq.(I.3) effectively modifies the one-dimensional barrier shape. Thus modified, the barrier is generally higher than for B = 0, whence the reduced transmission relative

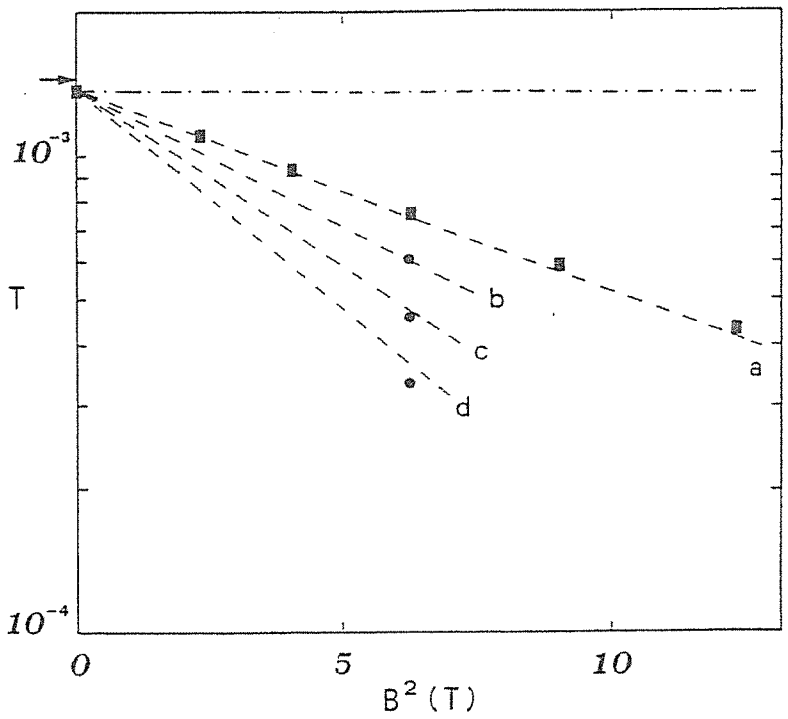

Figure 7.9:
Transmission coefficient vs. B^2 for a $\sigma = 90\,\mathring{A}$ wavepacket of energy $E_0 = 0.06\,eV$. The barrier parameters are $V_0 = 0.17\,eV$, $d = 94\,\mathring{A}$. The wavepacket is initially centered at the origin with $\mathbf{k}_0$ parallel to the x-axis.
(a) $|X_0 - x_c| = 440\,\mathring{A}$; (b) $|X_0 - x_c| = 511\,\mathring{A}$; (c) $|X_0 - x_c| = 581\,\mathring{A}$; (d) $|X_0 - x_c| = 652\,\mathring{A}$.
Dashed lines: WKB results.
Squares and dots: numerical results from our calculation.
The dash-dot line is the WKB result for $x_c = X_0$. The arrow indicates the zero-field exact transmission coefficient calculated from Eq.(7.12).

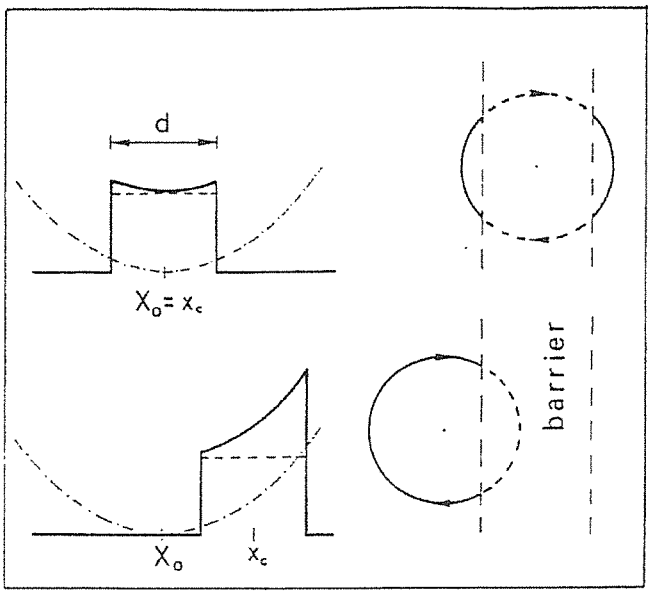

Figure 7.10:
Qualitative sketch of the effective potential barrier in a transverse magnetic field (solid line) for two different values of $X_0 - x_c$: the magnetic field is assumed to be zero outside the barrier region. In the right part of the figure the associated semi-classical orbits are schematically shown. With dash-dot line is indicated the magnetic potential $m^*\omega_c^2(x - X_0)^2/2$ and with dashed lines the bare potential barrier.

to B = 0 ("barrier magnetoresistance"). The barrier enhancement is minimum when the orbit center X_0 coincides with the barrier center x_c, and increases on either sides.

In order to compare our numerical results with the WKB formula (7.22) we must assign a value to X_0. It seems natural in the present context to identify X_0 with the center of the wavepacket orbit in the absence of the barrier. In Fig.7.9 we show with dashed lines the WKB predictions from Eq.(7.22), where we used for T_0 the observed zero-field effective transmission coefficient. The dependence of our calculated transmission coefficient T_{eff} on $(X_0 - x_c)$ is also shown in Fig.7.9 (black dots): for very large $(X_0 - x_c)$ the packet barely "touches" the barrier and very little transmission results (see also Fig.7.10). On the other hand, the transmission is maximum when the orbit center coincides with the middle of the barrier, $X_0 = x_c$. From Fig.7.9 one sees that our numerical results are well explained by the simple WKB formula (7.22), except for a small discrepancy for large $(X_0 - x_c)$, where the approximation used to derive (7.22) becomes poor.

A WKB expression for the tunnel current across a single potential barrier obtained using an expression similar to (7.22), averaged over X_0, was used in Ref.[130] to model successfully the experimentally observed reduction of the tunnel current in a single-barrier GaAs/GaAlAs diode placed in a transverse magnetic field.

7.9 Time delay of the tunneling packet.

Consider the single-barrier scattering of Fig.7.1. If the wavepacket is characterized by a narrow momentum distribution, a time delay for this scattering process can be calculated by following the peak of the packet via the method of the stationary phase [146,145]. According to this approach, the time it takes for the peak of the transmitted wavepacket to appear, measured from the moment the peak of the incident packet strikes the barrier, is given by (see also Appendix N):

$$\tau_\varphi = (\frac{m^*}{\hbar k})\frac{d\Delta\Phi}{dk} \simeq 2m^*/\hbar k K \qquad (7.24)$$

where $\Delta\Phi$ is the phase increase across the barrier and the latter equality is approximately valid in the thick barrier limit $Kd \gg 1$ [123]. k and K are the wavevectors outside and inside the barrier respectively. Expression (7.24) is

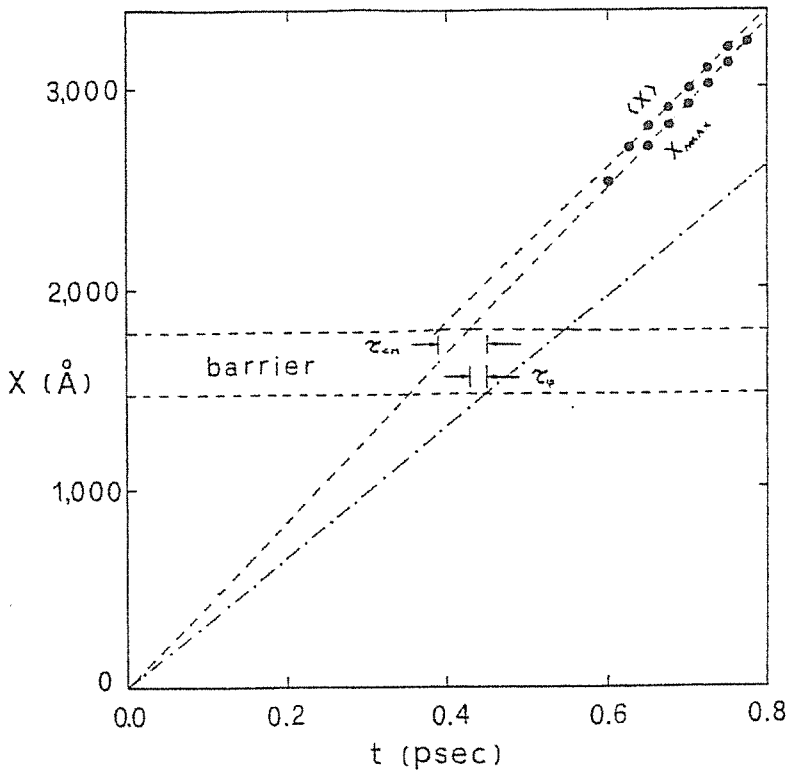

Figure 7.11:
Position of the transmitted wavepacket vs. time for the scattering process of Fig.7.1. The dash-dot line indicates the free-wavepacket motion $x = \hbar k_0 t/m^*$. The dashed lines are straight-line fits to the position of the maximum x_{max} and the center-of-mass $< x >$ of the transmitted wavepacket respectively. The arrows show the calculated phase delay τ_φ and τ_{CM}.

known as the "Wigner delay time"[146].

By extrapolating the *peak* positions of the transmitted packet of Fig.7.1 backwards to the right side of the barrier, as on Fig.7.11, we indeed obtain for this transmission time a number very close to τ_φ. The calculated time-delay $\tau_\varphi^{calc} \sim 0.02 \times 10^{-12}\, s$ is indicated by the arrows in Fig.7.11 and it compares favourably with the corresponding Wigner time $\tau_\varphi \simeq 0.023 \times 10^{-12}\, s$. The latter value is obtained using in (7.24) for k the initial momentum k_0 of the wavepacket.

One sees from Fig.7.11 that the velocity of the outgoing packet is slightly enhanced with respect to that of the incident packet by the usual "filtering" effect, i.e. the higher energy packet components are more effectively transmitted

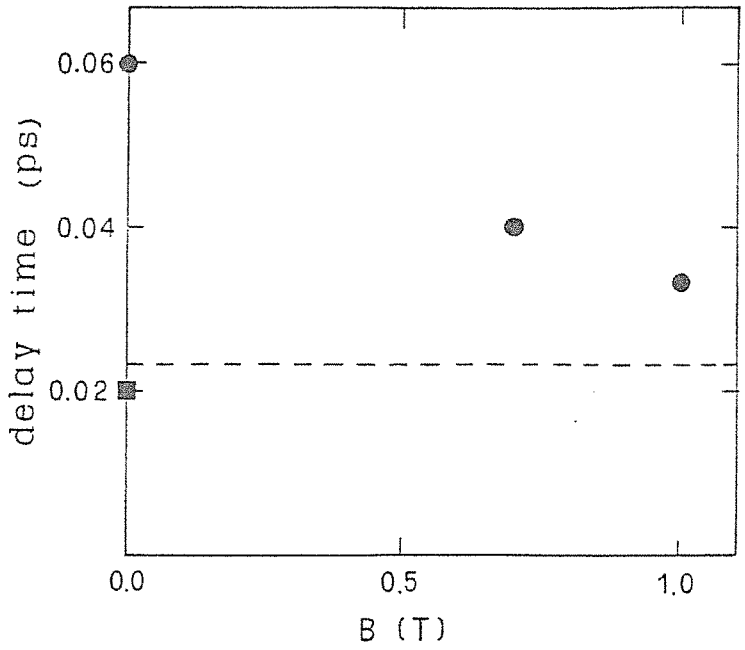

Figure 7.12:
Time delay vs. magnetic field strength B.
Dots: calculated center-of-mass delay time τ_{CM}.
Square: calculated zero-field phase-delay time τ_{φ}^{calc}.
The dashed line indicates the phase-delay time τ_{φ} as given by Eq.(7.24) in the text.

by the barrier than those of lower energy.

Another effect of the barrier is to cause a distinct deviation of the packet from its gaussian shape, as it is apparent from the last panel of Fig.7.1. As a result, the packet Center of Mass (CM) does not coincide with its maximum, and follows a different trajectory [149]. By extrapolating backwards the center of mass trajectory, one obtains a different packet delay time τ_{CM}, which turns out to be larger than τ_{φ} (see Fig.7.11). The time τ_{CM} is now thickness-dependent, whereas τ_{φ} was not. From Fig.7.11 one finds $\tau_{CM} \simeq 0.06 \times 10^{-12}\, s$. The necessity of introducing this time τ_{CM} in the present context stems particularly from the fact that we found essentially impossible, in the presence of the magnetic field, to fit a meaningful trajectory for the transmitted packet *maximum*, as needed for a comparison with τ_{φ}. As Fig.7.12 shows, the time τ_{CM} is field-dependent, and decreases as B increases. The figure suggests that for larger field values τ_{CM} might tend towards τ_{φ} from above. This result seems to indicate that, although at low fields the transmitted wavepacket is heavily

deformed, at larger fields the transmitted packet recovers its original gaussian shape [3] (note that when $V_b = 0$, as in Sect.7.6, the gaussian shape of the packet is always preserved during the motion).

7.10 Time-dependent resonant tunneling.

In this Section we present some results on the dynamics of an electron wavepacket tunneling through a Double-Barrier (DB) potential which contains a resonant level.

We show in the sequence of contour plots of Fig.7.13 the time-behavior of the charge-density $|\Psi(\mathbf{R},t)|^2$ for a wavepacket moving from the left towards a DB (shown with dashed lines in the Figure) composed of two equal square barriers of height $V_0 = 0.1\,eV$ and thickness $d = 35\,\mathring{A}$, separated by a distance $a = 47\,\mathring{A}$. The wavepacket has an average energy $E = 0.057\,eV$ equal to that of the "quasi-local" resonant level inside the well. In this case resonant tunneling is expected, as explained in Sect.6.2, i.e. a strong enhancement of the transmission, due to the Fabry-Perot-like interfering reflections of the electron wavefunction in the DB region. The plane-wave transmission coefficient for the DB described above is shown in Fig.7.14 vs. the incident energy.

One sees from the sequence of Fig.7.13 that a large fraction of the incident wavepacket is quickly trapped between the two barriers, giving rise to a high peak in the charge density in this region. In the meantime a double-peaked reflected wavepacket is formed, moving to the left in the Figure, and a transmitted packet emerges from the right edge of the double-barrier, moving to the right [4].

The subsequent decay of the trapped peak is quite slow with respect to the time scale required for the separation of the incident packet into well defined transmitted and reflected parts. The way in which an incoming packet of width σ splits into reflected and transmitted parts depends on σ (see, for instance,

[3] A gaussian transmitted packet would of course imply $\tau_{CM} = \tau_\varphi$.

[4] A general feature of wavepacket tunneling through a DB structure is the appearance of two reflected Gaussian-like pulses (see the last panel of Fig.7.13) which move with slightly different velocities. This can be understood by noticing that the reflection of the packet is governed by $R \equiv 1 - T$ which (see Fig.7.14) has a deep notch at the resonant energy. This divides the initial momentum distribution into two components, each of which gives rise to a separate pulse, as it is indeed observed. In particular, the leftmost peak in the last panel of Fig.7.13 is the faster of the two.

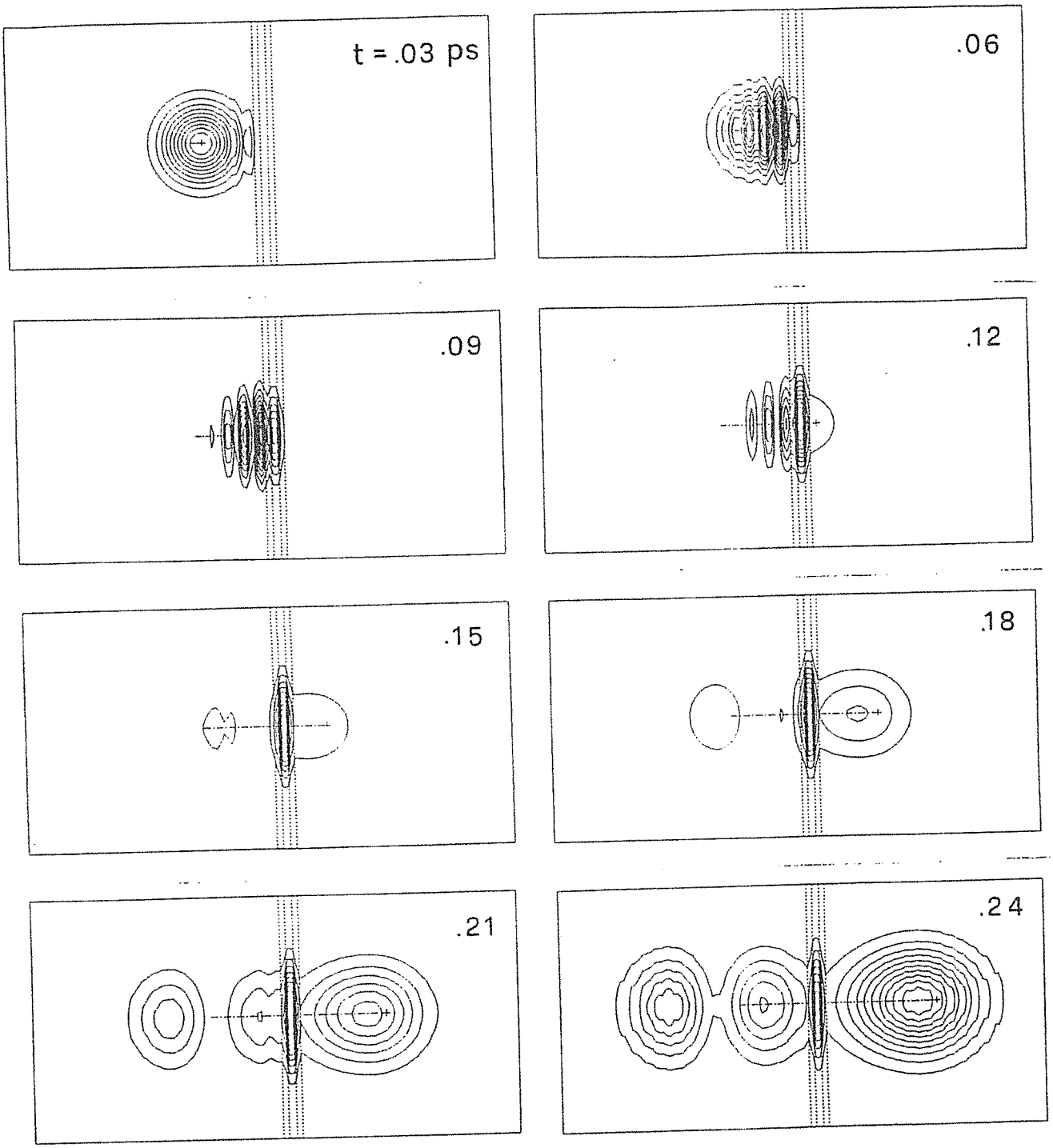

Figure 7.13:
Contour plots of the charge density $|\Psi(t)|^2$ for the scattering of a gaussian wavepacket of width $\sigma = 150\,\mathring{A}$ by a Double Barrier structure composed of two equal barriers of height $V_0 = 0.1\,eV$ and thickness $d = 35\,\mathring{A}$, separated by a distance $a = 47\,\mathring{A}$. At $t = 0$ the wavepacket is moving from the left towards the DB with energy $E_0 = 0.057\,eV$ at resonance with the single quasi-stationary state of the well. The energy spread of packet $\delta E \simeq \hbar^2 k_0/m^*\sigma \sim 0.025\,eV$ is comparable with the intrinsic width Γ of the DB resonance, which is shown in Fig.7.14. The dash-dot line shows the wavepacket trajectory in the absence of the double-barrier.

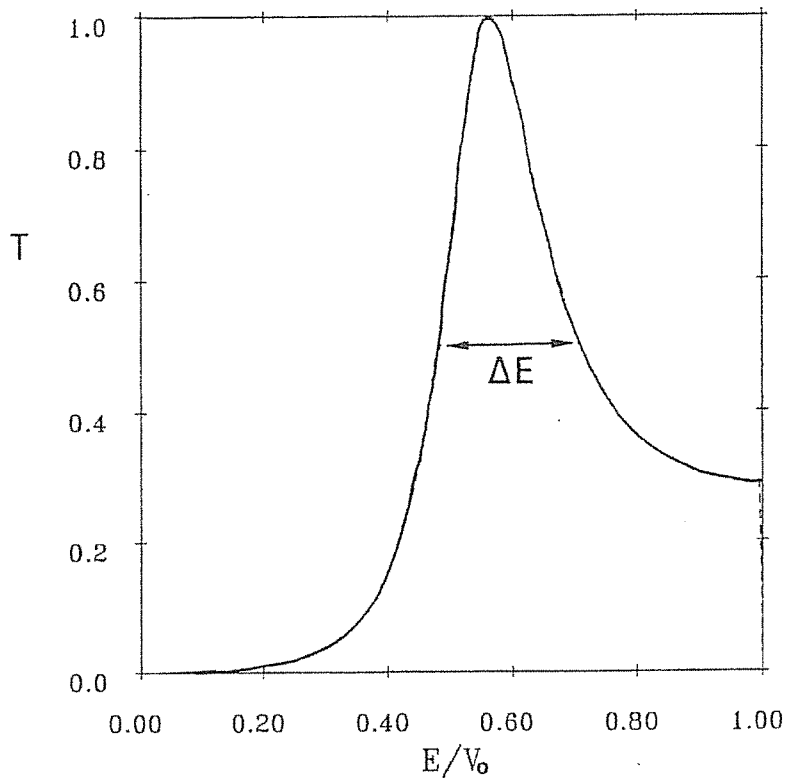

Figure 7.14:
Transmission coefficient for the double-barrier of Fig.7.13 vs. incident energy. The width ΔE of the resonance as obtained by our time-dependent calculations is shown.

Eq.(7.12) which gives the part of the packet that is transmitted through a single barrier). However, the decay of the charge Q which is trapped into the quasi-stationary state in the well is determined by the DB parameters only and follows the exponential law (6.21), i.e.

$$Q(t) = Q_0\, e^{-t/\tau_0} \tag{7.25}$$

where $\tau_0 = \hbar/\Delta E$ and ΔE is the width of the peak in the DB transmission coefficient (see Sect.6.2 for an heuristic derivation of Eq.(6.21)). From the fit of our numerical values for $Q(t)$, we have calculated $\hbar/\tau_0$ for the process of Fig.7.13. Our estimate for this quantity is compared in Fig.7.14 with the natural width of the peak in the DB transmission coefficient.

7.11 Resonant tunneling in a transverse magnetic field.

The effect of a magnetic field $B = 2.5\,T$ on the process of Fig.7.13 is shown in the sequence of snapshots of Fig.7.15 (see, for comparison, the single barrier scattering of Fig.7.5). As at $B = 0$, a rather large fraction of the tunneling packet is quickly trapped within the two barriers and subsequently decays outside. We are interested here in the effect of the magnetic field on the lifetime τ_0 of the resonant level inside the well.

The decay of the resonant peak is found to follow the exponential law (7.25) also in the presence of the magnetic field, from which the lifetime of the resonant level $\tau_0(B)$ can be extracted. According to the simplified approach described in Appendix L, where the magnetic field is assumed to be confined within the DB region, a monotonic increase of $\tau_0(B)$ is expected, due to the narrowing of the resonance with increasing magnetic field (see Fig.L.1). As explained in this Appendix, this approximation might be expected to hold in the case of real DB heterostructures, if electrons are injected and collected from a heavily doped semiconductor emitter and collector respectively, where the Landau levels are expected to be smeared out by disorder. However, if the carrier mean free path outside the barrier could be made comparable or longer than a few Larmor radii, then the full magnetic level structure outside the DB region would have to be taken into account and the results of Appendix L should have to be revised. In fact, the values of $\tau_0(B)$ as calculated from our time-dependent simulations (based on the full level structure) show a non-monotonic behavior with the field B, as shown in Fig.7.16: the dots are our numerical results, while the dashed line is only a guide to the eyes.

The observed oscillations in $\tau_0(B)$ can be understood by considering the stationary states of a DB in the presence of a transverse magnetic field. In the two panels on the left of Fig.7.17 we show the calculated stationary states in a magnetic field of 3 and $4\,T$ respectively, as a function of the cyclotron orbit center X_0 (these levels are calculated as explained in Appendix I). The value $B \sim 4\,T$ is one of the special values of the magnetic field at which a minimum in the lifetime τ_0 is observed (see Fig.7.16). The resonant level is clearly visible in Fig.7.17 as the flat level at about 60 meV (the arrows show where the resonant level lies at $B = 0$). We show in the right part of Fig.7.17 the square moduli of the wavefunctions for this particular level, for $X_0 = 0$ (i.e. the cyclotron

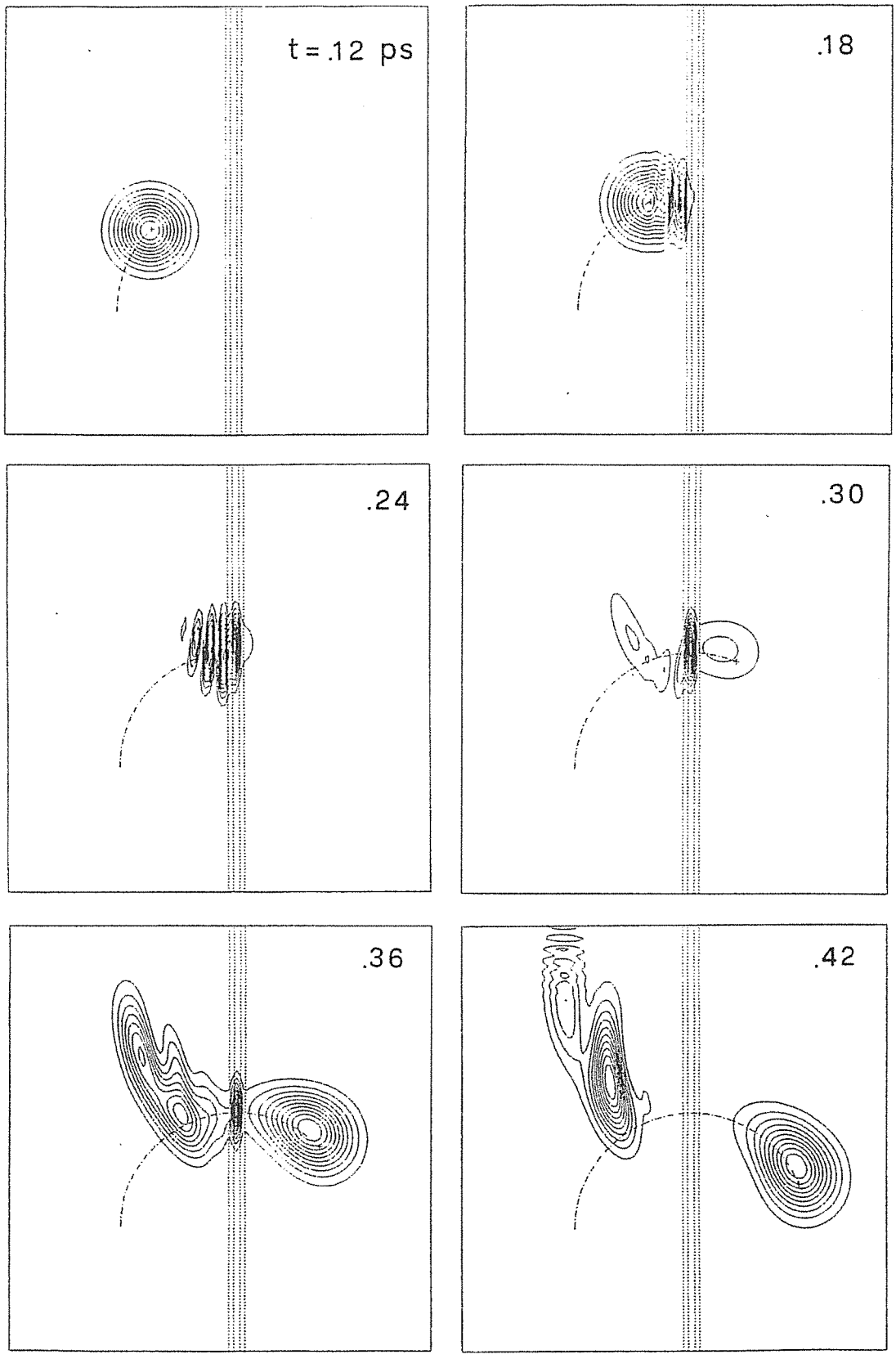

Figure 7.15:
Contour plots of the charge density $|\Psi(t)|^2$ (same barrier and packet parameters as in Fig.7.13), in a magnetic field $B = 2.5\,T$.

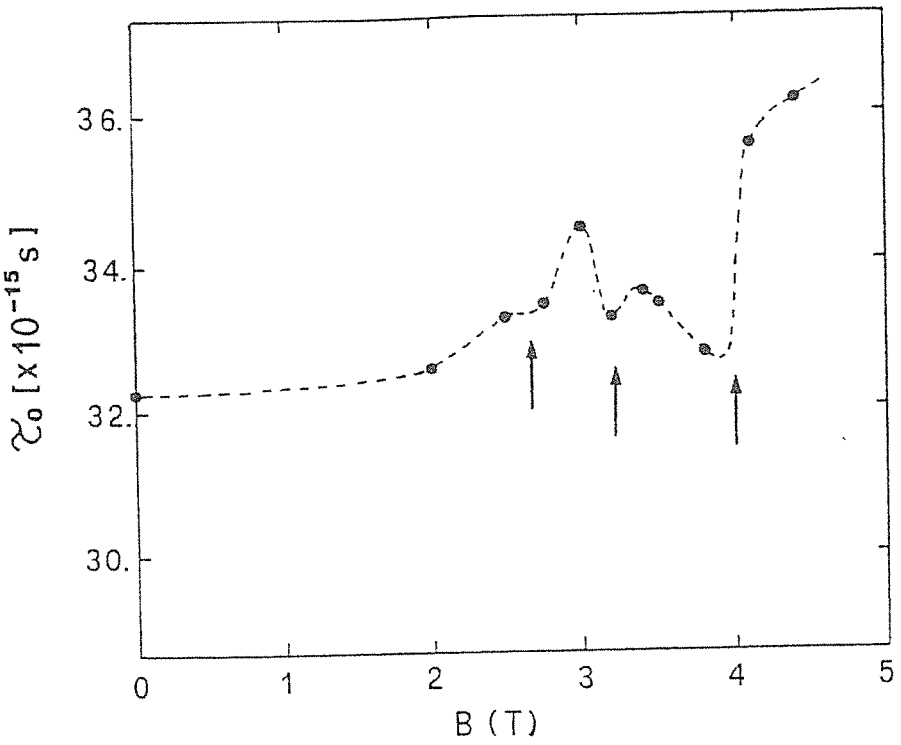

Figure 7.16:
Lifetime of the resonance as a function of the magnetic field. The dots are the results from our simulations, while the dashed line is only a guide to the eyes. The arrows are drawn at field values where a crossing between interfacial Landau levels ("skipping orbit" levels) and the quasi-local level in the well occur (see Fig.7.18 and the text).

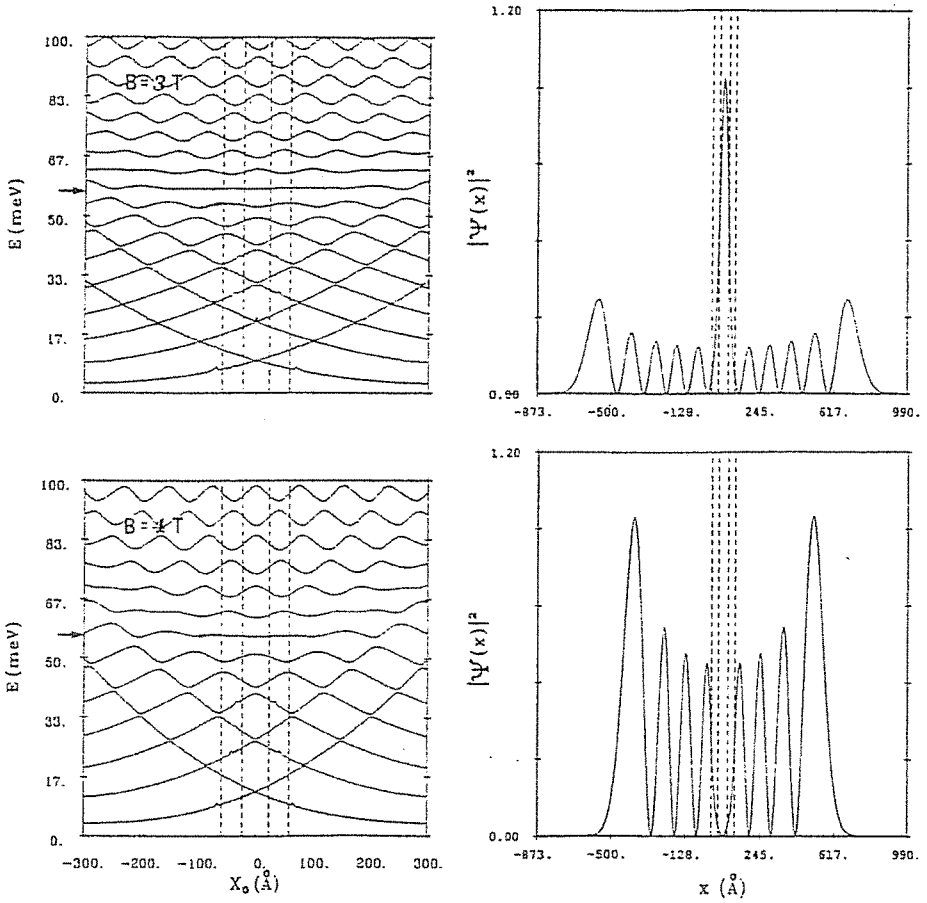

Figure 7.17:

Left: Eigenvalue spectra of the Double-Barrier in a magnetic field as a function of the cyclotron orbit center X_0, for $B = 3$ and $4\,T$. The arrows indicate where the resonant level is at $B = 0$.

Right: probability density for the wavefunction of the flat level at about $60\,meV$, at $X_0 = 0$ (for the same two values of the magnetic field). The double-barrier position is indicated with dashed lines.

Note that at $3\,T$ (i.e. between two minima in τ_0 in Fig.7.16) the wavefunction has a peak in the well region, while at $4\,T$ (i.e. at a minimum of τ_0) it has a dip there.

orbit center is right in the middle of the well). From Fig.7.17 one sees that, although at $B = 3\,T$ a large fraction of the charge is localized in the well region, at $B = 4\,T$ the electron is essentially localized outside the DB region.

Roughly speaking, one can think of the level structure of Fig.7.17 as obtained by coupling the set of interfacial Landau levels near the confining barriers with the localized state inside the well (these levels are shown with solid and dashed lines, respectively, in the upper part of Fig.7.18, together with the effective potential profile from which they arise[5]). The dispersion with the field of these levels is shown in Fig.7.18: note that the position of the resonant level is almost field-independent. When the resonant level does not match any of the "skipping-orbit" levels outside the barrier, its associated wavefunction is largely localized within the barriers (as it happens, e.g., at $B = 3\,T$, see Fig.7.17). On the other hand, for those particular values of the field for which a crossing occurs (as, e.g., at $B \sim 4\,T$), the hybridization between the two levels gives rise to a state characterized by the electron charge being localized mostly outside the barrier region: this corresponds to fast escape of the particle from the quasi-bound level by resonant tunneling into the skipping orbits. According to the above picture, at each crossing a reduction in the lifetime of the resonant level is to be expected. In Fig.7.18 three values of B for which a crossing takes place are visible and in fact we see that these values (indicated with arrows in Fig.7.16) do indeed roughly coincide with the observed dips in $\tau_0(B)$.

As discussed above, the observability of this phenomenon should be possible once sufficiently long mean free paths $\lambda \gg l_B$ are attainable outside the barrier.

[5]The interfacial Landau levels of Fig.7.18 are just the quantized version of the classical "skipping orbits" outside a reflecting barrier, as discussed in Appendix I.

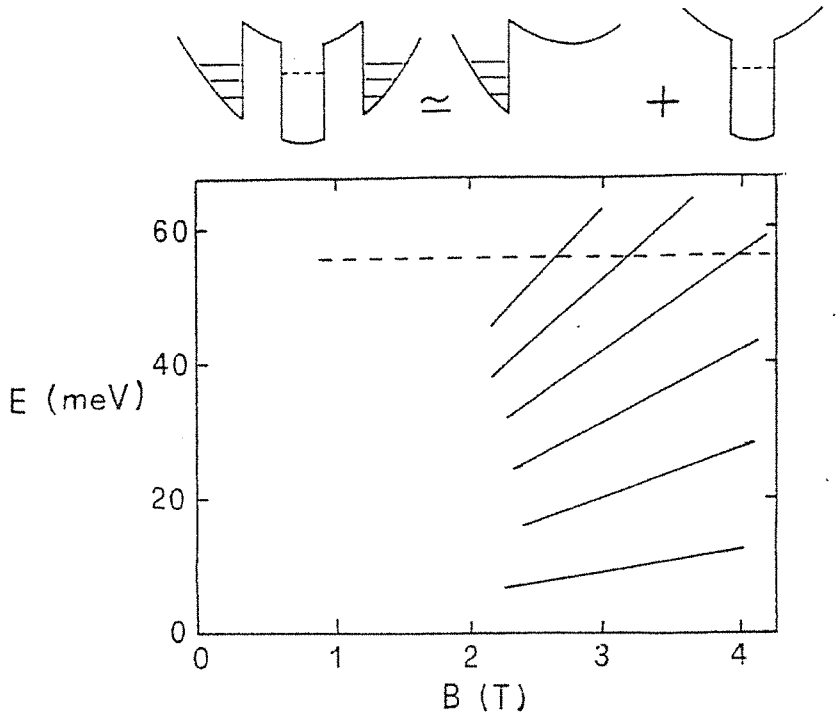

Figure 7.18:
Dispersions with the magnetic field of the interfacial "skipping orbits" Landau levels (solid lines) and of the resonant level in the well (dashed line). The two sets of levels, which are assumed to be uncoupled, arise from the effective potential profiles sketched in the upper part of the Figure. The three values of B where a crossing between the two sets of levels occur are reported in Fig.7.16 with arrows. At these values of B, the skipping orbit frequency and the resonance frequency resonate, and enhanced tunneling between them is to be expected. Tunneling into resonant skipping orbits is the explanation for the minima of τ_0 vs. B of Fig.7.16.

Appendix A

The Effective Mass Equation.

This Appendix contains a simple derivation of an Effective Mass (**EM**) equation as it is used, for instance, in the theory of shallow impurity states in semiconductors [138].

The starting point will be Eq.(2.1) in the text, i.e.:

$$[p^2/2m + V_c(\mathbf{r}) + U(\mathbf{r}) - E]\Psi(\mathbf{r}) = 0 \qquad (A.1)$$

Here V_c is the periodic potential of the perfect crystal and m is the free electron mass. We assume that the additional potential $U(\mathbf{r})$ is slowly varying and weak (in the sense precisely stated below), thus acting as a small perturbation. In such a case, the unperturbed states are the eigenfunctions of the equation:

$$[p^2/2m + V_c(\mathbf{r})]\Psi_{n\mathbf{k}}(\mathbf{r}) = E_n(\mathbf{k})\Psi_{n\mathbf{k}}(\mathbf{r}) \qquad (A.2)$$

i.e. Bloch waves extending over the entire lattice:

$$\Psi_{n\mathbf{k}}(\mathbf{r}) = u_{n\mathbf{k}}(\mathbf{r})exp(i\mathbf{k}\cdot\mathbf{r}) \qquad u_{n\mathbf{k}}(\mathbf{r}+\mathbf{R}) = u_{n\mathbf{k}}(\mathbf{r}) \qquad (A.3)$$

Here the functions $u_{n\mathbf{k}}(\mathbf{r})$ have the periodicity of the crystal potential $V_c(\mathbf{r})$. The wavevector $\mathbf{k}$ lies in the first Brillouin zone and n is a band index running over a complete set of bands.

For $U \neq 0$ we expand the solution of (A.1) in Bloch waves:

$$\Psi(\mathbf{r}) = \sum_{\mathbf{k}} \Phi_n(\mathbf{k})\Psi_{n\mathbf{k}}(\mathbf{r}) \qquad (A.4)$$

This gives the following set of coupled linear equations in $\Phi_n(\mathbf{k})$:

$$[E_n(\mathbf{k}) - E]\Phi_n(\mathbf{k}) + \sum_{\mathbf{k},\mathbf{k}'} < \Psi_{n\mathbf{k}}|U|\Psi_{n'\mathbf{k}'} > \Phi_{n'}(\mathbf{k}') = 0 \qquad (A.5)$$

The potential matrix elements in (A.5) are given by:

$$\begin{aligned} < \Psi_{n\mathbf{k}}|U|\Psi_{n'\mathbf{k}'} > &= \int \Psi^*_{n\mathbf{k}}(\mathbf{r})U(\mathbf{r})\Psi_{n'\mathbf{k}'}(\mathbf{r})d\mathbf{r} \\ &= \int exp[-i(\mathbf{k}-\mathbf{k}')\cdot\mathbf{r}]U(\mathbf{r})u^*_{n\mathbf{k}}(\mathbf{r})u_{n'\mathbf{k}'}(\mathbf{r})d\mathbf{r} \qquad (A.6) \end{aligned}$$

We shall consider in the following states with energy close to the band extremum $\mathbf{k} = 0$: in III-V semiconductor compounds, both the top of the valence band and the bottom of the conduction band are located at this point. Thus one can then use the approximation:

$$u_{n\mathbf{k}}(\mathbf{r}) \simeq u_{n0}(\mathbf{r}) \qquad (A.7)$$

Now, $u^*_{n0}(\mathbf{r})u_{n'0}(\mathbf{r}) = \sum_{\mathbf{G}} A_{nn'}(\mathbf{G})exp(i\mathbf{G}\cdot\mathbf{r})$, because of the periodicity in the direct lattice. Thus:

$$\begin{aligned} < \Psi_{n\mathbf{k}}|U|\Psi_{n'\mathbf{k}'} > &= \sum_{\mathbf{G}} A_{nn'}(\mathbf{G}) \int exp[-i(\mathbf{k}-\mathbf{k}'-\mathbf{G})\cdot\mathbf{r}]U(\mathbf{r})d\mathbf{r} \\ &= \sum_{\mathbf{G}} \hat{U}(\mathbf{k}-\mathbf{k}'-\mathbf{G})A_{nn'}(\mathbf{G}) \qquad (A.8) \end{aligned}$$

Here $\hat{U}(\mathbf{k})$ is by definition the Fourier transform of the external potential $U(\mathbf{r})$.

At this point we make use of the basic assumption that $U(\mathbf{r})$ is slowly varying on the length scale of the unit cell: this means that its Fourier transform is appreciably different from zero only when the argument is much smaller compared with a reciprocal lattice vector $\mathbf{G}$. Since we assumed that $\mathbf{k},\mathbf{k}'$ are very near the zone center, we can then ignore in the expansion (A.8) all the terms with $\mathbf{G} \neq 0$:

$$< \Psi_{n\mathbf{k}}|U|\Psi_{n'\mathbf{k}'} > \simeq \hat{U}(\mathbf{k}-\mathbf{k}')A_{nn'}(0) \qquad (A.9)$$

Furthermore, the orthogonality condition between Bloch functions requires:

$$(1/\Omega)\int_{cell} u^*_{n0}(\mathbf{r})u_{n'0}(\mathbf{r})d\mathbf{r} = A_{nn'}(0) = \delta_{nn'} \qquad (A.10)$$

the integration been performed over the lattice primitive cell of volume Ω. In deriving (A.10) we used the fact that, for any non-vanishing reciprocal lattice vector $\mathbf{G}$,

$$\int_{cell} exp(-i\mathbf{G}\cdot\mathbf{r}) = 0 \qquad (A.11)$$

Eqn.(A.5) finally reduces to:

$$[E_n(\mathbf{k}) - E]\Phi_n(\mathbf{k}) + \sum_{\mathbf{k}'} \hat{U}(\mathbf{k}-\mathbf{k}')\Phi_n(\mathbf{k}') = 0 \qquad (A.12)$$

In the small region around the extremum $\mathbf{k} = 0$, $E_n(\mathbf{k})$ can be expanded in powers of k:

$$E_n(\mathbf{k}) \simeq E_n(0) + (1/2)\sum_{\alpha,\beta} \frac{\partial^2 E_n(\mathbf{k})}{\partial k_\alpha \partial k_\beta} k_\alpha k_\beta \qquad (A.13)$$

In the case of a simple, isotropic, non-degenerate band extremum (e.g. the conduction band minimum of GaAs at the Γ-point), Eq.(A.13) reduces to:

$$E_n(\mathbf{k}) = E_n(0) + \hbar^2 k^2/2m^* \qquad (A.14)$$

m^* being the effective mass at the bottom of the band and $E_n(0)$ the band-edge energy (see Appendix B).

Eq.(A.12) can be finally written in real space by using the Fourier transform ($\mathbf{FT}$) of Φ_n:

$$F_n(\mathbf{r}) = \sum_{\mathbf{k}} \Phi_n(\mathbf{k}) exp(i\mathbf{k}\cdot\mathbf{r}) \qquad (A.15)$$

(note that the summation $\sum_{\mathbf{k}}$ has been tacitly extended over all k-space: this makes little difference because of the assumption that $F_n(\mathbf{k})$ is a strongly peaked function), and recalling that, in general

$$E(\mathbf{k})\Phi(\mathbf{k}) \longrightarrow \mathbf{FT} \longrightarrow E(-i\nabla)\Phi(\mathbf{r}) \qquad (A.16)$$

One finally finds the following Schrödinger-like equation in r-space:

$$[-\frac{\hbar^2}{2m^*}\nabla^2 + U(\mathbf{r})]F(\mathbf{r}) = [E - E_n(0)]F_n(\mathbf{r}) \qquad (A.17)$$

Eq.(A.17) is the Effective Mass Equation familiar from the theory of shallow impurities in semiconductors. From (A.4),(A.7),(A.15) one obtains the total wavefunction in this approximation:

$$\Psi(\mathbf{r}) \simeq F_n(\mathbf{r}) u_{n0}(\mathbf{r}) \qquad (A.18)$$

The slowly varying function $F_n(\mathbf{r})$ in (A.18) is usually called "Envelope Function".

Appendix B

The k · p method.

The k · p method is a powerful subsidiary tool to be used for the empirical determination of band structure (see, for instance, Ref.[25]). This method, coupled with the use of symmetry, shows that the band structure in the vicinity of a point in k-space depends on a small number of parameters (band gaps and effective masses) which may be determined by experiments.

Consider the one-particle problem of an electron moving in a periodic potential $V_c(\mathbf{r})$. The eigenvalue equation is:

$$H\Psi \equiv [p^2/2m + V_c(\mathbf{r})]\Psi = E\Psi \qquad , \qquad V_c(\mathbf{r}+\mathbf{R}) = V_c(\mathbf{r}) \qquad (B.1)$$

$\mathbf{R}$ being an arbitrary lattice vector. The wave function Ψ can be written in the Bloch form :

$$\Psi \equiv \Psi_{n\mathbf{k}}(\mathbf{r}) = u_{n\mathbf{k}}(\mathbf{r})exp(i\mathbf{k}\cdot\mathbf{r}) \qquad (B.2)$$

Substituting Eq.(B.2) in Eq.(B.1), one obtains:

$$[p^2/2m + (\hbar/m)\mathbf{k}\cdot\mathbf{p} + \hbar^2k^2/2m + V_c(\mathbf{r})]u_{n\mathbf{k}}(\mathbf{r}) = E_n(\mathbf{k})u_{n\mathbf{k}}(\mathbf{r}) \qquad (B.3)$$

Eqn.(B.3) can be written in the form :

$$[H_{\mathbf{k}0} + (\hbar/m)(\mathbf{k}-\mathbf{k}_0)\cdot\mathbf{p} + (\hbar^2/2m)(k^2-k_0^2)]u_{n\mathbf{k}}(\mathbf{r}) = E_n(\mathbf{k})u_{n\mathbf{k}}(\mathbf{r}) \qquad (B.4)$$

where

$$H_{\mathbf{k}0} \equiv p^2/2m + (\hbar^2/2m)\mathbf{k}_0 \cdot \mathbf{p} + \hbar^2 k_0^2/2m + V_c(\mathbf{r}) \qquad (B.5)$$

is such that

$$H_{\mathbf{k}0} u_{n\mathbf{k}_0} = E_n(\mathbf{k}_0) u_{n\mathbf{k}_0} \qquad (B.6)$$

When k is near $\mathbf{k}_0$, the terms added to $H_{\mathbf{k}0}$ in the left hand side of Eq.(B.4) can be treated by ordinary perturbation theory. This gives, to second order in ($\mathbf{k}$-$\mathbf{k}_0$) and for a non degenerate band,:

$$E_n(\mathbf{k}) = E_n(\mathbf{k}_0) + \frac{\hbar}{m}(\mathbf{k}-\mathbf{k}_0)\cdot \mathbf{p}_{nn} + \frac{\hbar^2}{2m}(k^2 - k_0^2) + (\frac{\hbar}{m})^2 \sum_{n'} \frac{|(\mathbf{k}-\mathbf{k}_0)\cdot \mathbf{p}_{nn'}|^2}{E_n(\mathbf{k}_0) - E_{n'}(\mathbf{k}_0)} \qquad (B.7)$$

where

$$p_{nn'} \equiv \int_{cell} u^*_{n\mathbf{k}_0}(\mathbf{r})\, \mathbf{p}\, u_{n'\mathbf{k}_0}(\mathbf{r}) d\mathbf{r} \qquad (B.8)$$

Consider the case in which $\mathbf{k}_0$ is an extremum: then the term linear in k in the above equation is missing and we can always choose axis so that the quadratic terms in Eq.(B.7) have no cross-product terms. Eq.(B.7), for the particular case $\mathbf{k} = 0$, becomes:

$$E_n(\mathbf{k}) = E_n(0) + (\hbar^2/2)\sum_i k_i^2/m_i^* \qquad (B.9)$$

$$1/m_i^* = 1/m + (2/m^2)\sum_{n'} \frac{|\mathbf{i}\cdot \mathbf{p}_{nn'}|^2}{E_n(0) - E_{n'}(0)} \qquad (B.10)$$

where $\mathbf{i}$ is a unit vector in the direction of the i-th principal axis. Eq.(B.10) shows in particular that the interaction with bands of lower (higher) energy tends to reduce (increase) the effective mass. To the same order of approximation, it is possible to express $u_{n\mathbf{k}}(\mathbf{r})$ in terms of the $\mathbf{k} = 0$ functions $u_{n0}(\mathbf{r})$:

$$u_{n\mathbf{k}}(\mathbf{r}) \simeq u_{n0}(\mathbf{r}) + (1/m)\sum_{n'} \frac{\mathbf{k}\cdot \mathbf{p}_{nn'}}{E_n(0) - E_{n'}(0)} u_{n'0}(\mathbf{r}) \qquad (B.11)$$

It is clear that the above approximations are good as long as the band considered is non-degenerate and separated by *large* gaps from all other bands. From (A.4),(A.15),(B.11) one sees that the total electronic wave function in the Envelope Function approximation is (see Eq.(2.17)):

$$
\begin{aligned}
\Psi(\mathbf{r}) &= \sum_{\mathbf{k}} \Phi_n(\mathbf{k})\Psi_{n\mathbf{k}}(\mathbf{r}) \\
&= \sum_{\mathbf{k}} \Phi_n(\mathbf{k}) exp(i\mathbf{k}\cdot\mathbf{r})\{u_{n0}(\mathbf{r}) + \frac{1}{m}\sum_{n'\neq n} \frac{\mathbf{k}\cdot\mathbf{p}_{nn'}}{[E_n(0) - E_{n'}(0)]} u_{n'0}(\mathbf{r}) \\
&= F_n(\mathbf{r})u_{n0}(\mathbf{r}) + (1/m)\sum_{n'\neq n} \frac{-i[\nabla F_n(\mathbf{r})]\cdot p_{nn'}}{E_n(0) - E_{n'}(0)} u_{n'0}(\mathbf{r}) \qquad (B.12)
\end{aligned}
$$

The correction term proportional to the gradient of the envelope function is essential if one is interested in investigating the derivative of the wave function $\Psi(\mathbf{r})$; this is the case when the effect of the boundary conditions for the Effective Mass equation at the sharp boundary between two different semiconductor must be taken into account.

Appendix C

Three-band k · p model Hamiltonian.

The following matrix represents the $\mathbf{k} \cdot \mathbf{p}$ model Hamiltonian describing the interaction of the s-like spin-degenerate conduction band ($s\uparrow$ and $s\downarrow$) with the upper spin-orbit $J = 3/2$ partner in the valence band (Γ_6 and Γ_8 states in Fig.2.1b in the text) in a direct- gap semiconductor. The four degenerate $\mathbf{k} = 0$ valence band-edge states are labelled by $J_z = \pm 1/2$, $J_z = \pm 3/2$ while $s\uparrow$ and $s\downarrow$ denote the spin-degenerate conduction band-edge states. The lower half of the matrix is obtained by hermitean conjugation.

	$s\uparrow$	$3/2$	$-1/2$	$s\downarrow$	$1/2$	$-3/2$
$s\uparrow$	H_{11}	$\sqrt{3}H_{12}$	H_{12}^*	0	H_{15}	0
$3/2$		H_{22}	H_{23}	0	H_{25}	0
$-1/2$			H_{33}	$-H_{15}$	0	$-H_{25}$
$s\downarrow$				H_{11}	H_{12}	$\sqrt{3}H_{12}^*$
$1/2$					H_{33}	H_{23}
$-3/2$						H_{22}

(C.1)

where

$$
\begin{aligned}
H_{11} &= E_c + \frac{k^2}{2m^*} \\
H_{22} &= E_v - \frac{1}{2}(\gamma_1 - 2\gamma_2)k_z^2 - \frac{1}{2}(\gamma_1 + \gamma_2)(k_x^2 + k_y^2) \\
H_{33} &= E_v - \frac{1}{2}(\gamma_1 + 2\gamma_2)k_z^2 - \frac{1}{2}(\gamma_1 - \gamma_2)(k_x^2 + k_y^2) \\
H_{12} &= \frac{i}{\sqrt{6}}P(k_x + ik_y) \\
H_{15} &= -i\sqrt{\frac{2}{3}}Pk_z \\
H_{23} &= \frac{\sqrt{3}}{2}\gamma_2(k_x^2 - k_y^2) - i\sqrt{3}\gamma_3 k_x k_y \\
H_{25} &= \sqrt{3}\gamma_3(k_x - ik_y)k_z
\end{aligned}
$$

In the above matrix elements E_c and E_v denote the conduction and valence band-edges respectively. The material parameters γ_1, γ_2, γ_3 and P (see Sect.2.4) for GaAs are listed in Table II.

Appendix D

Boundary conditions for the Envelope-Function : coupled bands.

It is straightforward to generalize to the many-band case the boundary conditions (2.7,2.10). They become ([34,13]):

$$F_j^A(-\varepsilon) = F_j^B(+\varepsilon) \qquad (D.1)$$

$$\sum_{j'=1}^{N} \{P_{jj'}^z - i \sum_{\alpha=1}^{3} (D_{jj'}^{z\alpha} + D_{jj'}^{\alpha z}) \nabla_\alpha\} F_{j'} \qquad \textit{continuous at } z = 0 \qquad (D.2)$$

($j = 1, 2, ..., N$) (see Eq.2.13 and what follows it for the exact meaning of the symbols). Here N is the number of bulk-bands which contribute with comparable weight to the formation of the wavefunctions. It is important to stress the fact that the second condition, which is the analogous of Eq.(2.7) for the simple band case, is derived by using for the wavefunction the expression (2.17), correct to first order in a $\mathbf{k} \cdot \mathbf{p}$ expansion. One must also assume the validity of (2.12) for the N bands of interest.

Let's specialize these boundary conditions for the case of an ideal planar interface between lattice matched semiconductor A and B and assume that the Hamiltonian H has the form (C.1) in Appendix C appropriate to a six-band model. The potential $U(\mathbf{r})$ in the Effective Mass Equation (2.16) depends only

on z and k_x, k_y are thus good quantum numbers. This means that one can write:

$$F_j^{A,B}(\mathbf{r}) = exp(ik_x x + ik_y y)F_j^{A,B}(z) \qquad (D.3)$$

so that Eq.(D.2) reads:

$$\sum_{j'=1}^{6}\{P_{jj'}^{z} + \sum_{\alpha=x,y}(D_{jj'}^{z\alpha} + D_{jj'}^{\alpha z})k_\alpha - 2iD_{jj'}^{zz}\frac{\partial}{\partial z}\}F_{j'} \qquad continuos \qquad (D.4)$$

An additional simplification stems from the fact that the matrix elements $P_{jj'}$ are the same in the two materials (because the u_n 's functions are the same). Eq.(D.4) thus further simplifies to:

$$\sum_{j'=1}^{6}\{\sum_{\alpha=x,y}(D_{jj'}^{z\alpha} + D_{jj'}^{\alpha z})k_\alpha - 2iD_{jj'}^{zz}\frac{\partial}{\partial z}\}F_{j'} \qquad continuos \qquad (D.5)$$

To determine the eigenfunctions and eigenvalues of the system of differential equations (2.16) with the boundary conditions (D.1,D.5), a standard method of band structure theory has been used [87]. One defines an "interface functional" I embodying the boundary conditions, such that if $\Phi = (F^A, F^B)$ is a solution with energy E of Eq.(2.16):

$$H\Phi = \begin{pmatrix} H^A & 0 \\ 0 & H^B \end{pmatrix} = E\begin{pmatrix} F^A \\ F^B \end{pmatrix} \qquad (D.6)$$

and if F^A, F^B satisfy the proper boundary conditions at the $A-B$ interface, then the functional

$$E[\Phi] = \frac{<\Phi|H + I|\Phi>}{<\Phi|\Phi>} \qquad (D.7)$$

is stationary with respect to arbitrary variations $\delta\Phi$ of the wavefunction $\Phi = (F^A, F^B)$ (that is, the variational principle is valid also for trial wavefunctions that do not satisfy the boundary conditions) and furthermore $E <\Phi|\Phi>=<\Phi|H + I|\Phi>$. Once the interface functional is known, one can take two suitable sets of basis functions in A and B, with the periodicity of the superlattice, into which to expand F^A, F^B respectively. The explicit expression of the functional I is

$$<\Phi|I|\Phi> \;=\; (i/2)\{< F^A|\bar{J}(0)|F^A > - < F^B|\bar{J}(0)|F^B >$$

$$+ < F^B|\bar{J}(0)|F^A > - < F^A|\bar{J}(0)|F^B >\} \qquad (D.8)$$

$\bar{J}(0)$ being the current operator averaged over the unit cell (see Eq.2.8). The eigenproblem can thus be solved through a standard matrix diagonalization, making in addition easier to implement self-consistent calculations when charge transfer across the interface is expected.

Appendix E

Low-field dispersion of the Hole Landau levels in a Quantum Well.

We show in the following how the anomalous low-field dispersion with the magnetic field of the LH_1 subband in Fig.3.1 can be understood simply in terms of the interaction between LH_1 and the second HH_2 subband.

The bulk valence-band top is described by the 4×4 Luttinger Hamiltonian that can be obtained from the matrix Hamiltonian (3.7) by removing rows and columns 1 and 4 and using renormalized material parameters (2.19). The envelope functions are given by an expression similar to (3.9) but with the first and fourth component missing.
Let's consider for simplicity the case $n = -1$. Thus, as it is apparent from the form of the Hamiltonian (3.7), only $HH \downarrow$ and $LH \uparrow$ states enter into the wavefunction (see the left side of Table III for the labeling of states). If we let the a, a^+ operators appearing in the Hamiltonian matrix act on the harmonic oscillator functions ϕ_n in the four components envelope function, the following 2×2 matrix is obtained :

$$H = \begin{vmatrix} A & R \\ R & D \end{vmatrix} \qquad (E.1)$$

where

$$A = -(\gamma_1^L + 2\gamma_2^L)\frac{k_z^2}{2} - \frac{eB}{2c}(\gamma_1^L - \gamma_2^L - \kappa^L)$$

$$D = -(\gamma_1^L - 2\gamma_2^L)\frac{k_z^2}{2} - \frac{3eB}{2c}(\gamma_1^L + \gamma_2^L - \kappa^L)$$

$$R = -\gamma_3\sqrt{6eB/c}k_z$$

and k_z is the wave vector component parallel to the QW axis.

In the absence of the linear- k_z coupling, the A and D terms would give the dispersion relation of a purely Light and Heavy hole respectively, characterized by effective masses in the z-direction $m^*_{HH,LH} = (\gamma_1^L \mp 2\gamma_2^L)^{-1}$: let $C_{LH,m}(z)$,$C_{HH,m'}(z)$ represent the corresponding eigenfunctions, when the QW boundary conditions are taken into account (m and m' thus being discrete quantum numbers). In $(E.1)$ k_z has to be replaced by $-i\partial/\partial z$, according to the usual prescription of the Effective Mass theories [32]; we seek for a solution F of the associated EM equations $\sum_{i,j} H_{ij}F_j = EF_i$ of the form :

$$F = \begin{vmatrix} \alpha C_{LH,m}(z) \\ \beta C_{HH,m'}(z) \end{vmatrix} \qquad (E.2)$$

The EM equations can be recasted in the form of a system of two algebraic equations in the unknown coefficients α and β: solutions of the system exist if

$$det \begin{vmatrix} < C_{LH,m}|A - E|C_{LH,m} > & < C_{LH,m}|R|C_{HH,m'} > \\ < C_{LH,m}|R|C_{HH,m'} >^* & < C_{HH,m'}|D - E|C_{HH,m'} > \end{vmatrix} = 0 \qquad (E.3)$$

In a symmetric QW potential C_{LH},C_{HH} are either even or odd with respect to the reflection $z \rightarrow -z$; since $R \propto -i\partial/\partial z$, the off-diagonal matrix elements in $(E.3)$ are different from zero only if the two states have different parity: thus the first $(m = 1)$ LH_1 state will interact essentially with the second $(m' = 2)HH_2$ state.

Let $E_\pm(B)$ represent the two roots of Eq.$(E.3)$ for this choice of the C_{LH} and C_{HH} states, the upper sign referring to the solution with highest energy. The inverse effective masses in the (k_x, k_y)-plane, for the two levels, are proportional to:

$$\left.\frac{dE_\pm}{dB}\right|_{B=0} = -\frac{e}{2c}\left[2\gamma_1^L + \gamma_2^L - 2\kappa^L + sign[E_{0,LH_1} - E_{0,HH_2}](\gamma_1^L + 2\gamma_2^L - \kappa^L) \mp \frac{12|<k_z>|^2\gamma_3^{L\,2}}{|E_{0,LH_1} - E_{0,HH_2}|}\right] \qquad (E.4)$$

where E_{0,LH_1}, E_{0,HH_2} are the zero-field confinement energies of the two holes:

$$E_{0,LH_1} = \frac{1}{2}(\gamma_1^L + 2\gamma_2^L) < C_{LH,1}|\frac{\partial^2}{\partial z^2}|C_{LH,1}>, \quad E_{0,HH_2} = \frac{1}{2}(\gamma_1^L - 2\gamma_2^L) < C_{HH,2}|\frac{\partial^2}{\partial z^2}|C_{HH,2}> \qquad (E.5)$$

and $< k_z >$ is defined as

$$< k_z > \equiv < C_{LH,1}| - i\frac{\partial}{\partial z}|C_{HH,2} > \qquad (E.6)$$

Let's consider the simplest case of an infinite square well potential of width L; then $C_{LH,1} = \sqrt{2/L}\, sin(\pi z/L)$, $C_{HH,2} = \sqrt{2/L}\, sin(2\pi z/L)$ and

$$E_0(LH_1) = -\frac{1}{2}(\gamma_1^L + 2\gamma_2^L)(\pi/L)^2,\ E_0(HH_2) = -\frac{1}{2}(\gamma_1^L - 2\gamma_2^L)(2\pi/L)^2$$

$$< k_z > = 8i/3L \qquad (E.7)$$

Substituting $(E.7)$ in $(E.4)$ and using the material parameters appropriate for $GaAs$ [93], i.e. $\gamma_1^L = 6.85$, $\gamma_2^L = 2.1$, $\gamma_3^L = 2.9$, $\kappa^L = 1.2$, it turns out that $dE_-/dB|_0 > 0$, i.e. the upper $n = -1$ level has an initial electron-like dispersion.

It must be noted that this state is the HH_2 in the infinite square well, whereas the finite barriers have the effect to push the LH_1 edge above it (see Fig.3.1 in the text).

Appendix F

Matrix elements for intra-band optical transitions.

The second term in Eq.(3.14) in the text can be rewritten in the following form:

$$M^{(2)}_{n,n'} = \sum_i < F^i_n|\mathbf{p}\cdot\epsilon|F^i_{n'} > \simeq m_0 \sum_{ij} < F^i_n|(\hat{\mathbf{v}}\cdot\epsilon)_{ij}|F^j_{n'} > \qquad (F.1)$$

(see Eq.(3.15) for the notation). Here, instead of the first-principle scalar interaction $\mathbf{p}\cdot\epsilon$, the matrix interaction term $m_0\hat{\mathbf{v}}\cdot\epsilon$ has been used [95]; the velocity operator $\hat{\mathbf{v}}$ is defined in terms of the Hamiltonian (3.7) as

$$(\hat{v}_\alpha)_{ij} \equiv \frac{\partial(H_{ax})_{ij}}{\partial k_\alpha} \qquad (F.2)$$

and is also a 6×6 matrix acting on the Envelope-Functions F_n defined in (3.9). For circularly polarized light, $\epsilon_z = 0$; then $\epsilon\cdot\mathbf{v} = \epsilon_+ v_- + \epsilon_- v_+$, where $\epsilon_\pm \equiv (\epsilon_x \pm i\epsilon_y)/\sqrt{2}$ and

$$\begin{aligned} v_\pm &= (v_x \pm iv_y)/\sqrt{2} = \frac{1}{\sqrt{2}}\left(\frac{\partial H_{ax}}{\partial k_x} \pm i\frac{\partial H_{ax}}{\partial k_y}\right) \\ &= (c/eB)^{1/2}\frac{\partial H_{ax}}{\partial a^\mp} = \mp(c/eB)^{1/2}[a^\pm, H_{ax}] \qquad (F.3) \end{aligned}$$

In deriving $(F.3)$ the usual definition of the creation and annihilation operators $a^\pm = (c/2eB)^{1/2}(k_x \pm ik_y)$ have been used [50] (see also Eq.(3.5)in the text). Thus:

$$M^{(2)}_{n,n'} = (c/eB)^{1/2}(E_F - E_I)\epsilon_\pm \sum_i < F^i_n|a^\mp|F^i_{n'} > \qquad (F.4)$$

E_I,E_F being the energies of the initial and final levels. From the definition (3.9) of the envelope functions $|F_n>$ and from the orthogonality of the oscillator states with different index n, one derives immediately the selection rule $\Delta n = \pm 1$, where the $+$ $(-)$ sign holds for left (right) circularly polarized light. We underline the fact that the above selection rule pertains to the axial model only: if one uses the exact Hamiltonian (3.6), including the cubic part (3.8) and the terms that come in when the crystal lacks inversion symmetry [26], the previous selection rule must be relaxed and one has instead $\Delta n = \pm m$ with m odd integer [82]. The matrix element (F.4) has been used in this form in connection with the interpretation of Cyclotron-Resonance experiments in 2-D hole gas in $GaAs/AlGaAs$ heterostructures [44].

Appendix G

Excitons in Quantum Wells and Superlattices.

G.1 Excitons in Quantum Wells and Superlattices.

Excitons are bound electron-hole pairs and are the lowest electronic excited states in non-metallic crystals [89]. In the case of a semiconductor with simple, isotropic valence and conduction bands with extrema at k = 0, and assuming a weak binding limit, the exciton spectrum is given by the solutions of an hydrogen-like Effective Mass equation and has the well-known form (see, for instance, Ref. [25]):

$$E_n = -Ry^*/n^2 \qquad n = 1, 2, ... \tag{G.1}$$

(the zero of energy is taken at the bottom of the conduction band). Ry^* is the effective Rydberg:

$$Ry^* = e^4\mu/2\hbar^2\varepsilon^2 \tag{G.2}$$

where μ is the reduced electron-hole mass and ε the dielectric constant of the host material. Excitons in optical spectra appear as sharp line structures just below the band gap, in contrast to the broad transitions into the continuum [19].

In QW structures, the exciton is modified because of the confinement of

carriers in the potential wells [1]. If the layer thickness is smaller than the exciton Bohr radius, the exciton shrinks in one dimension: the electron and hole are forced to move closer to each other and the Coulomb binding energy increases. In the extreme case of a perfectly 2D exciton, this binding energy becomes [90]

$$E_B^{(2D)} = -4Ry^* \qquad (G.3)$$

The theoretical limit (G.3) is never reached in real systems, due to finite barrier effect[67]: it has been shown ([66,57]) that the binding energy in a Quantum Well first increases with decreasing layer thickness L_z and decreases in very narrow wells, the barrier height being kept constant. The reason for this behavior is fairly simple: as L_z is reduced the exciton wavefunction is compressed in the QW, leading to increased binding. However, beyond a certain value of L_z, the spilling of the wavefunction in the adjacent $AlGaAs$ layers becomes more important and this makes the binding energy go closer and closer to the bulk $AlGaAs$ value.

In a $GaAs/GaAlAs$ SL, when the width of the $GaAlAs$ barriers decrease (small period SL), neighbouring wells become coupled and the electron-hole pair progressively looses its 2D character, since both particles are allowed to move to some extent in the direction perpendicular to the layers. The exciton binding energies in small period $GaAs/Ga_{0.7}Al_{0.3}As$-SL has been determined by means of photoluminescence excitation spectroscopy [96] and it has been found that the (Heavy Hole) exciton binding energy tends to the $GaAs$-bulk value when the period of the Superlattice approaches zero.

In bulk $GaAs$ one observes experimentally a single exciton resonance. The reduced symmetry of the QW structures, however, removes the Light and Heavy hole band degeneracy, and a two-exciton system results: in absorption experiments a double peak is observed [2]. Fig.G.1 reproduces early optical measurements on $GaAs/GaAlAs$ QW's for three different values of the well width L_z (from Ref. [19]). The exciton peak shifts towards higher energies and splits into a LH and a HH component as the well becomes narrower and the system becomes two-dimensional (bottom figure). Note also the different structure of

[1] In the following we restrict ourselves to the most relevant case in which both electrons and holes are confined within the same layer, as it happens for instance in the $GaAs/AlGaAs$ systems.

[2] The increase of the exciton binding energy in a QW allows the observation of exciton photoluminescence lines at room temperature.

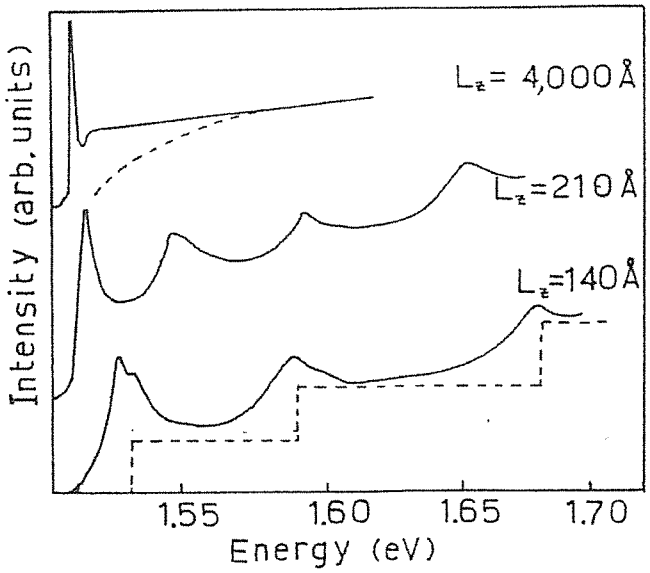

Figure G.1:
Absorption spectra at $2°K$ of a 4000, 210 and 140 $Å$- thick GaAs layer between $Al_{0.2}Ga_{0.8}As$ barriers (after Ref.[19]). Dashed lines: schematic 3-D (top figure) and 2-D (bottom figure) density of states.

the background spectrum due to transitions to the continuum, which reflects directly the different dimensionality of the systems: the dashed lines show, respectively in the top and bottom figure, the schematic Density Of States for 3D (proportional to $\sqrt{E}$) and for 2D systems, for simple parabolic bands: in the 2D case, each of the two-dimensional subbands gives rise to a DOS that is independent of the energy and equal to $m^*/\pi\hbar$, so that the cumulative DOS for a series of bands will have the staircase-like form shown in Fig.G.1. For a recent review on the optical properties of semiconductor QW, including excitonic effects, see [97].

G.2 2-D exciton in a transverse magnetic field.

Consider the following Effective Mass equation describing the relative motion of an electron-hole pair in the presence of an external magnetic field parallel to the z-axis [25]:

$$\{\frac{1}{2m_e^*}[\mathbf{p}-(e/2c)\mathbf{B}\wedge\mathbf{r}]^2+\frac{1}{2m_h^*}[\mathbf{p}+(e/2c)\mathbf{B}\wedge\mathbf{r}]^2-\frac{e^2}{\varepsilon r}\}\Phi(\mathbf{r})=E\Phi(\mathbf{r}) \quad (G.4)$$

It is a common practice to introduce a dimensionless parameter γ to indicate the relative strengths of the magnetic field effect and Coulomb interaction:

$$\gamma=\hbar\omega_c/2Ry^* \quad (G.5)$$

Here $\hbar\omega_c \equiv \hbar eB/\mu c$ is the cyclotron effective energy. Many attempts have been made to solve Eq.(G.4) by perturbation theory ($\gamma \ll 1$), using the adiabatic approximation ($\gamma \gg 1$) and using variational methods (see Ref.[25] and references therein).

Consider now the case of a hypothetical Two-Dimensional hydrogenic exciton in a uniform magnetic field: this problem is somewhat related to the problem of excitons in Quantum Wells, due to the quasi-2D behavior induced by quantum confinement. For this 2D case Eq.(G.4) reduces to the following differential equation [68]:

$$-\frac{\hbar}{2\mu}[\frac{1}{r}\frac{d}{dr}(r\frac{d}{dr})+\frac{m^2}{r^2}]R(r)+(\frac{e^2B^2r^2}{8c^2\mu}-\frac{e^2}{\varepsilon r})R(r)=E'R(r) \quad (G.6)$$

where R is the radial part of the electron-hole wavefunction. Here m is a magnetic (integer) quantum number and the energy E' is related to E in Eq.(G.4) by:

$$E'=E-\frac{eB}{2\mu c}(m_e^*-m_h^*/m_e^*+m_h^*) \quad (G.7)$$

We will consider only the case $m=0$. This corresponds to the "allowed case" of the optical excitation spectrum, which is the most important from the experimental point of view [25]. We will quote only some limiting expressions of the eigenvalue spectrum of Eq.(G.6), obtained in a WKB approximation [68]. In particular, the strong-field asymptotic formula (G.11) has been used in Section 3.4 to correct for excitonic effects the results of magneto-optical calculations therein.

(a) For vanishing magnetic field (*exciton* case):

$$E = -\frac{1}{(n+1/2)^2} \quad , \quad n = 0, 1, 2, ... \qquad (G.8)$$

(b) For vanishing Coulomb interaction (*Landau level* case):

$$E = 2\gamma(n + 1/2) \qquad (G.9)$$

(c) In the *weak* magnetic field limit ($\gamma \ll 1$):

$$E = -\frac{1}{(n+1/2)^2} + \frac{5}{8}(n + 1/2)^4\gamma^2 \qquad (G.10)$$

(d) In the *strong* magnetic field limit ($\gamma \gg 1$):

$$E = (2n + 1)\gamma - \frac{3\gamma^{1/2}}{(2n+1)^{1/2}} \qquad (G.11)$$

In the formulas listed above, energies are measured in effective Rydbergs Ry^*. The square root dependence of Eq.(G.11) can be obtained easily by treating the Coulomb term $e^2/\varepsilon r$ as a perturbation acting on the free-particle states $|n>$ that are solutions of the 2D harmonic-oscillator equation to which Eq.(G.6) reduces when the Coulomb interaction term $-e^2/\varepsilon r$ is absent. The first order correction to the unperturbed Landau level spectrum can be written as

$$<n|\frac{e^2}{r}|n> \simeq \frac{e^2}{a_n} = (\frac{\mu\omega_c}{\hbar})\frac{e^2}{(2n+1)^{1/2}} \qquad (G.12)$$

where a_n is the mean orbit radius for a 2D oscillator of frequency ω_c: thus excitonic effects are expected to be less important for large values of the quantum number n. In the high field limit $\gamma \gg 1$, if one neglect the second term in (G.11), the usual Landau level free-particle behavior is recovered.

We report in Fig.G.2 the calculated levels, solutions of Eq.(G.6), for field strengths up to $\gamma = 1$ (the figure is taken from Ref. [68]). The lowest level ($n = 0$) looks independent of the magnetic field up to $\gamma \sim 1$, but in higher magnetic field region it goes parallel to the corresponding free Landau level, after crossing the $E = 0$ line at $\gamma \simeq 12.5$.

In Ref.[68] the relative intensities for optical excitations in the states $m = 0$, which are proportional to the squared modulus $|R(r = 0)|^2$, are also calculated as a function of the quantum number n for several values of the reduced field γ and found to be essentially independent of the quantum number n ($n > 2$).

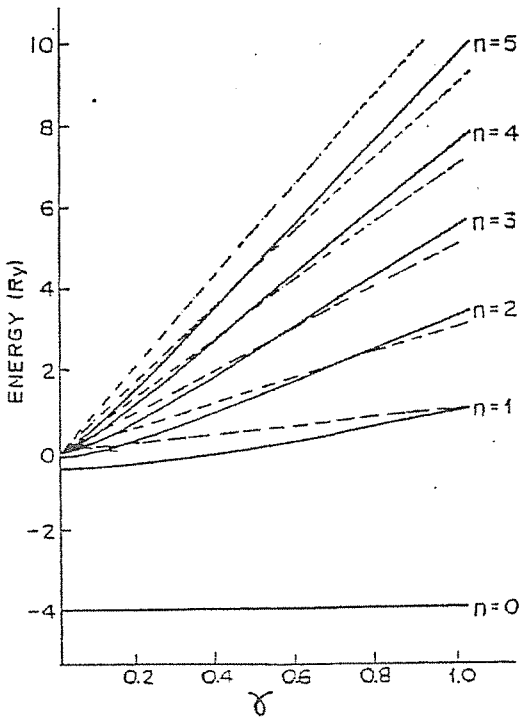

Figure G.2:
Energy eigenvalues as functions of the magnetic field strength γ. The broken lines denote the free Landau levels.

In a recent paper[65] a theory of magneto-excitons in $GaAs$ QW's (valid in the weak and intermediate magnetic fields, $B < 10\,T$) was formulated, in which the valence band mixing associated with the Γ -point band structure of $GaAs$ was explicitly taken into account. The complementary theory for high fields was developed in Ref.[43]. In particular, in Ref.[43] all the observable optical transitions are found to involve bound excitons and the exciton lines are significantly different in energy from the unbound electron-hole pair lines. Moreover, due to the LH and HH mixing at finite fields, excitonic states cannot be attributed a purely Light or Heavy hole character. This effect is brought about mainly by the magnetic field which mixes the hole levels. This mixing is correctly accounted for by our calculations in Sect.3.4 even if our treatment of the Coulomb interaction is more approximate. One striking point of disagreement with our results is that, in σ^- polarization, the second transition line of lowest energy is attributed to the $3dHH$ exciton, rather than to the $1sLH$ one.

Appendix H

Numerical values of some characteristic quantities.

We give in the following the numerical values of several useful quantities. m^*, μ, when appearing in the third member of each expression,are in unit of the free electron mass m. ε is the semiconductor static dielectric constant ($\varepsilon_{GaAs} = 12.54$). The areal density N_s is in units of $10^{11}\, cm^{-2}$. The dimensionality parameters D_1 and D_2 in (H.9) and (H.10) are given by [68]

$$D_1 = \begin{cases} 1/4 & (3D\ case) \\ 1 & (2D\ case) \end{cases}$$

$$D_2 = \begin{cases} 1 & (3D\ case) \\ 3/16 & (2D\ case) \end{cases}$$

Effective Böhr radius:

$$a_0^*[\mathring{A}] = \varepsilon\hbar^2/e^2m^* = 5.292 \times 10^{-1}\, \varepsilon/m^* \qquad (H.1)$$

Dimensionless Wigner-Seitz radius:

$$r_s = (\pi N_s)^{-1/2}/a_0^* = 3.371 \times 10^2 N_s^{-1/2}\ m^*/\varepsilon \qquad (H.2)$$

2D Fermi Energy, one subband occupied:

$$E_F[meV] = \pi\hbar^2 N_s/m^* = 2.380 \times 10^{-1} N_s\ /m^* \qquad (H.3)$$

Size of the lowest cyclotron orbit:

$$l_B[\mathring{A}] = (\hbar c/eB)^{1/2} = 2.566 \times 10^2/(B[T])^{1/2} \qquad (H.4)$$

Landau level Filling factor:

$$\nu = 2\pi\hbar c N_s/eB = 4.136 N_s/B[T] \qquad (H.5)$$

Effective Rydberg:

$$Ry^*[meV] = \mu e^4/2\hbar^2\varepsilon^2 = 1.361 \times 10^4 \mu/\varepsilon^2 \qquad (H.6)$$

Effective cyclotron energy:

$$\hbar\omega_c^*[meV] = \hbar eB/m^* c = 1.158 \times 10^{-1} B[T]/m^* \qquad (H.7)$$

Reduced cyclotron energy:

$$\gamma = \hbar\omega_c^*/2Ry^* = 4.254 \times 10^{-6}(\varepsilon/\mu)^2 B[T] \qquad (H.8)$$

Exciton binding energy:

$$E_b[meV] = 3Ry^* D_1[\hbar eB/2(2n+1)\mu Ry^*]^{1/2} = 6.690\, D_1\, [B[T]/(2n+1)]^{1/2} \qquad (H.9)$$

Exciton diamagnetic shift:

$$\Delta E[meV] = D_2\varepsilon^2\hbar^4 B^2/4\mu^3 c^2 e^2 = 1.942 \times 10^{-5} D_2 B^2[T]/\mu^3 \qquad (H.10)$$

Appendix I

Landau levels and interface currents.

The stationary states of the Hamiltonian (7.1) can be conveniently calculated by using the Landau gauge for the vector potential, $\mathbf{A_L} = \mathbf{A_S} + \frac{1}{2}B\nabla xy = (0, Bx, 0)$. In this gauge the Hamiltonian (7.1) takes the form

$$\hat{H} = \frac{1}{2m^*}(p_x^2 + p_y^2) + \frac{e^2B^2x^2}{2m^*c^2} - \frac{i\hbar eBx}{m^*c}\frac{\partial}{\partial y} + V_b(x) \qquad (I.1)$$

By using a plane wave solution $exp(ik_y y)$ in the y direction, one finds immediately that the function $\Phi(x)$ describing the motion along the x-direction satisfies the equation

$$[-\frac{\hbar^2}{2m^*}\frac{d^2}{dx^2} + V_{eff}(x)]\Phi(x) = E\Phi(x) \qquad (I.2)$$

where

$$V_{eff} = \frac{1}{2}m^*\omega_c^2(x - X_0)^2 + V_b(x) \qquad (I.3)$$

As usual, $X_0 \equiv \hbar k_y c/eB = l_B^2 k_y$ is interpreted as the "center" of the cyclotron orbit (of radius $R_n = (2n+1)^{1/2}l_B$) associated with the n-th Landau level. When $V_b = const.$, Eq.(I.2) reduces to the familiar harmonic-oscillator Hamiltonian whose solutions are equidistant Landau levels having the same energy $\hbar\omega_c(n + 1/2)$ for all values of k_y. In the presence of the barrier potential $V_b(x)$ the translational invariance along x is broken: the eigenvalues of Eq.(I.2) depend on X_0 and a non-flat dispersion relation develops in the x direction

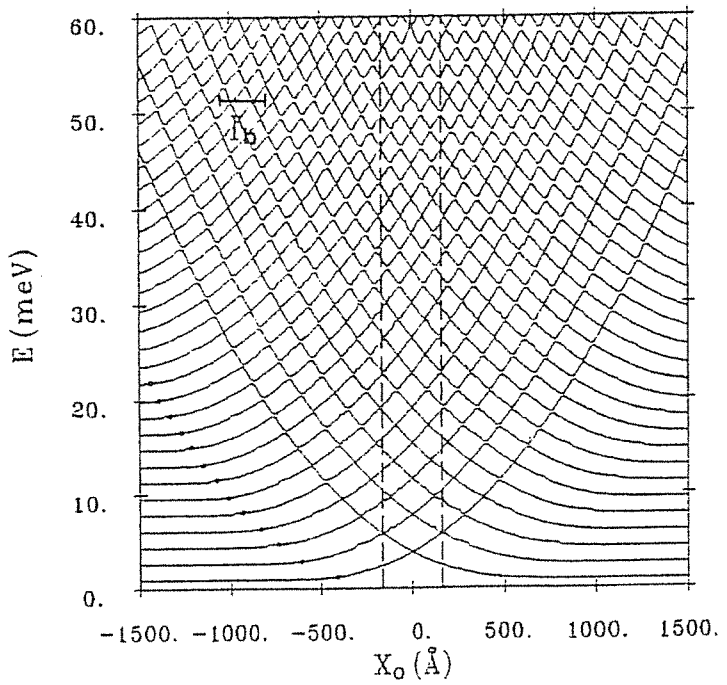

Figure I.1:
Magnetic energy levels vs. the center X_0 of the semi-classical orbit, at $B = 1\ T$. The barrier parameters are $V_0 = 0.06\ eV$ and $d = 328\ \AA$. The magnetic length $l_B = 256\ \AA$ is shown in the upper part of the Figure. The dots are the orbit radii $R_n = (2n+1)^{1/2} l_B$, measured from the left edge of the barrier (which is indicated with dashed lines). The effective mass m^* used is that of an electron at the bottom of the conduction band of $GaAs$, i.e. $m^* = 0.067\, m_0$, m_0 being the bare electron mass.

[133]. We show in Fig.I.1 the eigenvalues of (I.2) as a function of X_0, in the presence of the same barrier used for our time-dependent calculations. These eigenvalues were calculated using an efficient iterative method, based on the Numerov' algorithm, which is decribed in detail in Appendix O. The barrier is indicated with dashed lines and the magnetic length l_B is also shown. The barrier is centered at $x = 0$.

From Fig.I.1 one can see that the deviations from "unperturbed", flat Landau levels occur at a distance from the barrier corresponding to the cyclotron orbit radii $R_n = (2n+1)^{1/2} l_B$ (points in the figure): this is consistent with an intuitive, purely classical picture, in which the energy levels are expected to change when the cyclotron orbit "touches" the barrier (for a thorough discussion of Landau levels in heterostructures, see for example Ref. [133]). Where

the Landau levels come close in energy they interact and small gaps open up between them. For instance, at $X_0 = 0$ one sees from Eq.(I.2) that the effective potential V_{eff} is symmetric about $x = 0$, so that the wavefunctions can be either even or odd with respect to a reflection about the origin. The splitting in energy between pairs of wavefunctions with opposite parity is determined by the tunneling probability through the barrier and thus decreases exponentially with the barrier transparency Kd. For the thick barrier of Fig.I.1, these splittings are very small and hardly visible on the scale of the figure.

The bending of a Landau level near the barrier implies the presence of an edge current. It follows from Ehrenfest's theorem that the current parallel to the edge of the potential step is proportional to [150]:

$$v_y \equiv d<y>/dt = <\partial H/\partial p_y> = \hbar^{-1}(\partial E/\partial k_y) = (c/eB)(\partial E/\partial X_0) \qquad (I.4)$$

Let's consider, for the sake of simplicity, the case of an infinite potential step V_∞ extending from $x = 0$ towards positive x and take in particular $X_0 = 0$, i.e. the center of the cyclotron orbit is right at the interface. The potential energy term in (I.3) is $V_0 = \frac{1}{2}m\omega_c^2 x^2 + V_\infty$; the solution Φ_0 of lowest energy is the n=1 harmonic oscillator wave function, which has a node at x=0 [1]:

$$\Phi_0 = \begin{cases} (\frac{2}{\sqrt{\pi}})^{1/2}(\frac{m\omega_c}{\hbar})^{3/4} x e^{-m\omega_c x^2/2\hbar} & \text{if } x \leq 0 \\ 0 & \text{if } x > 0 \end{cases} \qquad (I.5)$$

with energy $E_0 = \frac{3}{2}\hbar\omega_c$.

Let's now consider the shifted potential $V' = \frac{1}{2}m\omega_c^2(x - X_0)^2 + V_\infty \simeq V_0 - m\omega_c^2 x X_0$, with X_0 arbitrarily small: the difference $V' - V_0$ can be treated within first-order perturbation theory. In this approximation the energy of the state Φ_0 is $E'(X_0) \simeq E_0 + \frac{2}{\sqrt{\pi}}\hbar\omega_c X_0(m\omega_c/\hbar)^{1/2}$. Thus, from (I.4):

$$v_y = \frac{2\hbar}{\sqrt{\pi}m^*}(eB/\hbar c)^{1/2} = \frac{2}{\sqrt{\pi}}\omega_c l_B \qquad (I.6)$$

This result can be compared to that obtained by considering a classical semi-circular "skipping" orbit (like the one indicated with dash-dot line in Fig.7.7 in the text) of radius l_B where the electron, repeatedly reflected from the barrier, drifts along it with a net velocity $v_y \approx (2l_B)/(\pi/\omega_c)$.

[1] In general, any odd-n harmonic-oscillator wave function will be an acceptable solution of this simple problem.

Appendix J

2-D isotropic harmonic oscillator.

The Ehrenfest equations associated with the Hamiltonian (7.4) in the absence of the barrier potential $V_b(x)$ are:

$$\begin{aligned}
\frac{d<x>}{dt} &= \frac{1}{m^*}<p_x> + \frac{1}{2}\omega_c <y> \\
\frac{d<y>}{dt} &= \frac{1}{m^*}<p_y> - \frac{1}{2}\omega_c <x> \\
\frac{d<p_x>}{dt} &= -\frac{1}{4}m^*\omega_c^2 <x> + \frac{1}{2}\omega_c <p_y> \\
\frac{d<p_y>}{dt} &= -\frac{1}{4}m^*\omega_c^2 <y> - \frac{1}{2}\omega_c <p_x> \qquad (J.1)
\end{aligned}$$

These equations coincide with the canonical Hamilton's equations for a 2-D isotropic harmonic oscillator of frequency $\omega_c/2$ (see Sect.7.2). One can easily show that the solution of the system of equations (J.1) is given by:

$$\begin{aligned}
<x> &= (p_{0x}/m^*\omega_c)sin(\omega_c t) - (p_{0y}/m^*\omega_c)cos(\omega_c t) + x_0 + p_{0y}/m^*\omega_c \\
<y> &= (p_{0y}/m^*\omega_c)sin(\omega_c t) + (p_{0x}/m^*\omega_c)cos(\omega_c t) + y_0 - p_{0x}/m^*\omega_c \\
<p_x> &= +\frac{1}{2}[(p_{0y} - \frac{1}{2}m^*\omega_c x_0)sin(\omega_c t) + (p_{0x} + \frac{1}{2}m^*\omega_c y_0)cos(\omega_c t) + \\
&\quad +(p_{0x} - \frac{1}{2}m^*\omega_c y_0)]
\end{aligned}$$

$$<p_y> = -\frac{1}{2}[(p_{0x} + \frac{1}{2}m^*\omega_c y_0)sin(\omega_c t) - (p_{0y} - \frac{1}{2}m^*\omega_c x_0)cos(\omega_c t) - \\ -(p_{0y} + \frac{1}{2}m^*\omega_c x_0)] \qquad (J.2)$$

Here $\mathbf{r}_0 \equiv (x_0, y_0)$ and $\mathbf{p}_0 \equiv (p_{0x}, p_{0y})$ denote the initial average position and momentum. The trajectory is an arc of a circle, centered at $(x_0 + p_{0y}/m^*\omega_c, y_0 - p_{0x}/m^*\omega_c)$, of radius

$$R_c = (p_{0x}^2 + p_{0y}^2)^{1/2}/m^*\omega_c \qquad (J.3)$$

Appendix K

The Chebychev time-propagation scheme.

We describe in this Appendix the basic ingredients of the Chebychev method that we used in Chapter 7 to solve the Time-Dependent Schrödinger Equation. We follow in the exposition Ref.[137] and Ref.[140] mainly.

The method is based on a suitable polynomial expansion of the time-evolution operator $\hat{U} = exp[-i\hat{H}t/\hbar]$. The problem of a series representation of the operator $\hat{U}$ is mathematically equivalent to representing the scalar function e^z by a polynomial expansion in the complex variable z, where z belongs to the domain which includes all the eigenvalues of the operator $-i\hat{H}t/\hbar$. It has been demonstrated [137] that the best approximation is achieved by an expansion in the complex Chebychev polynomials Φ_k. These polynomials are the complex version of the real Chebychev polynomials of the first kind T_k [142] and are defined by $\Phi_k(\omega) = i^k T_k(-i\omega)$, with $\omega \in [-i, i]$.

In practical implementations of the method the wavefunction to be propagated in time is represented on a discrete spatial grid (see Sect.7.3). The domain of the eigenvalues λ of the Hamiltonian $\hat{H}$, which depends on the discretization prescription, can be estimated as follows. The maximum kinetic energy is roughly $P^2_{max}/2m^*$, where $P_{max} \simeq \sqrt{\sum_{i=1}^{d}(\pi/\Delta_i)^2}$. Thus $\lambda \in \{V_{min}, V_{max} + P^2_{max}/2m^*\}$, where V_{min}, V_{max} are the minimum and maximum of the potential represented on the d-dimensional grid.
Using the definitions

$$R = \frac{1}{2\hbar}(P^2_{max}/2m^* + V_{max} - V_{min})t \quad , \quad G = \frac{t}{\hbar}V_{min} \qquad (k.1)$$

and

$$\omega = -z/R - i(R+G)/R \tag{k.2}$$

one can write

$$e^z = e^{-i(R+G)} e^{-R\omega} \tag{k.3}$$

with $\omega \in [-i, i]$. Note that R is the size of the time-energy phase-space volume spanned by the system. At this step e^z is expanded into a (truncated) Chebychev series:

$$e^z \simeq \sum_{k=0}^{M} a_k \Phi_k(\omega) \tag{k.4}$$

where the coefficients a_k are given by

$$a_k = (-1)^k c_k e^{-i(R+G)} J_k(R) \tag{k.5}$$

Here the J_k are Bessel functions of the first kind of order k and $c_k = 1$ if $k = 0$, otherwise $c_k = 2$. The Chebychev polynomials $\Phi_k(\omega)$ can be computed iteratively using the recurrence relation

$$\Phi_k(\omega) = 2\omega \Phi_{k-1}(\omega) + \Phi_{k-2}(\omega) \tag{k.6}$$

together with $\Phi_0(\omega) = 1$ and $\Phi_1(\omega) = \omega$. The propagation scheme is finally obtained by substituting $-i\hat{H}t/\hbar$ for z in Eq. (k.2) and using it in the series (k.4). The action of the Hamiltonian on the wave function is evaluated locally in direct-space: non-local terms (i.e. terms containing spatial derivatives) can be efficiently calculated using a Fast Fourier Transform algorithm.

The high accuracy of the expansion (k.4) [137] can be traced to the fact that when k is greater than R, $J_k(R)$ goes to zero exponentially fast. Thus the degree M of the expansion has to be at least R. Typical values of R encountered in our calculations are of the order of a few hundreds.

The basic algorithm described above can be used very efficiently as a one-step propagator which allows to obtain the wave function $\Psi(t)$ directly from the initial state Ψ_0. It is remarkable that, within this approach, the size of the time step t is by no means limited by accuracy requirements, the necessary accuracy being achieved only by including a sufficient number of terms in the expansion (k.4). It must be noted, however, that the above method is not suited to the case when a fine temporal mesh is required, i.e. when the the initial wavefunction is propagated for a "small" time t: in fact it has been shown [141] that a lower

limit exists ($M \sim 40 - 50$) for the number of terms needed to converge the sum (k.4).

Since for each of the M terms in (k.4) most of the computer time is invested in FFT computations, numerical effort for the overall calculation of $\Psi(t)$ scales roughly as $\sim t\, L^d\, ln\, L$, where L is the side of the d-dimensional "box" containing the system.

Being based on a truncated series expansion of a unitary operator, the Chebychev scheme is not unitary: therefore energy and norm of the wave functions are not conserved. This means that the accuracy in the computation of the propagated wave function can be estimated by looking at the deviations of the average energy and norm of the wave function at time t from their values at $t = 0$. Typical deviations encountered in our simulations are reported in Sect.7.4.

Appendix L

Transmission coefficient for a Double Barrier in a transverse magnetic field: an approximate calculation.

In this Appendix the effect of a transverse magnetic field on the tunneling probability of electrons in a Double-Barrier (DB) potential is investigated under the simplifying assumption that the field is confined to the DB region. This approximation may apply in real heterostructures to the case of heavily doped emitter and collector regions (i.e. the semiconductor electrodes, enclosing the DB structure, from which carriers are injected and collected respectively), where the Landau levels are expected to be smeared out by disorder.

It is shown [154] that, in this case, the value of the transmission coefficient at resonance is unaffected by the field: however, the width of the resonance peak is found to decrease monotonically with increasing magnetic field. As a result, the peak in the current-voltage characteristic of the Double-Barrier as a diode is largely depressed when the magnetic field strength is increased.

Consider a beam of particles, of kinetic energy E and effective mass m^*, incident on a rectangular potential barrier of height V_0 and width d. The "opacity" of the barrier is determined by Kd, where $K \equiv \sqrt{(2m^*/\hbar^2)(V_0 - E)}$ is the decay constant of the wave function in the classically forbidden region.

Recent works[132,130] were concerned with the elastic tunneling of elec-

trons in a transverse magnetic field (i.e. the field **B** is applied perpendicularly to the tunnel current direction) up to 5 Tesla, through very opaque barriers ($Kd \gg 1$), realized with $Al_xGa_{1-x}As$ layers sandwiched between two n-doped $GaAs$ buffers. Few hundreds Ångstroms-thick barriers were used: the sideway deflecting effects of the magnetic field on the tunnel current are in fact expected, on classical grounds, to be more significant if the width of the barrier is of the order of the cyclotron radius of the electrons $l_B \equiv (\hbar c/|e|B)^{1/2} \sim 256/\sqrt{B\,[Tesla]}\,\mathring{A}$.

The dynamics of a particle tunneling through a thick barrier in a transverse magnetic field has been extensively studied in Chapter 7 of this thesis and in particular, in Sect.7.8, the effect of the magnetic field in reducing the "transparency" of the barrier has been investigated using a semi-classical WKB approach. We repeat here the simple argument contained in Sect.7.8 which allows to understand qualitatively the observed reduction of the tunnel current when a transverse magnetic field is applied [130,132].

With $\mathbf{B} \| z$ and x the heterostructure growth direction, the Hamiltonian of the system is given by Eq.(I.1) of Appendix I, i.e.

$$H = \frac{1}{2m^*}(p_x^2 + p_y^2) + \frac{e^2B^2x^2}{2m^*c^2} - \frac{i\hbar eBx}{m^*c}\frac{\partial}{\partial y} + V_b(x) \qquad (L.1)$$

Here $\mathbf{p} \equiv -i\hbar\nabla$. $V_b(x)$ is the barrier potential and the Landau gauge $\mathbf{A_L} = (0, -Bx, 0)$ has been chosen. By using plane waves in the z and y direction (and neglecting spin effects), one finds that the envelope function $\Phi(x)$ describing the motion along the x-direction satisfies the equation $H_0\Phi(x) = E(k_y)\Phi(x)$ with H_0 given by (see Eq.(I.2 and I.3 in Appendix I):

$$H_0 = -\frac{\hbar^2}{2m^*}\frac{d^2}{dx^2} + \frac{1}{2}m^*\omega_c^2(x - X_0)^2 + V_b(x) \qquad (L.2)$$

$X_0 = \hbar k_y c/eB \equiv l_B^2 k_y$, as usual, is interpreted as the center of the semi-classical cyclotron orbit of the electron (see Sect.7.8 and Appendix I). The reduction of the tunnel current through the barrier with increasing magnetic field can be easily understood in terms of the increase of the effective barrier height due to the diamagnetic term $m^*\omega_c^2(x - X_0)^2/2$ in Eq. (L.2): if one assumes that the magnetic field is confined to the barrier region, then the last two terms in Eq.(L.2) can be viewed as giving an effective potential barrier $V_{eff}(x)$. If one neglects the band bending due to possible charge redistribution, the term

$V_b(x)$ can be modelled by a simple rectangular potential profile of height V_0 and width d: the resulting V_{eff} is schematically drawn in Fig.7.10, for two different values of X_0. The origin of the x-coordinates is chosen here at the center of the barrier.

The WKB transmission probability $T_{eff}(B)$ for this effective barrier has been obtained in Sec.7.8 and is given by Eq.(7.22) therein: the effect of the magnetic field is mainly to cause an exponential decrease of T_{eff} with B^2. No such reduction of the transmission coefficient, as we shall see in the following, takes place when the electron experiences *resonant* tunneling through a Double-Barrier structure like the one sketched in Fig.6.2.

It is well known that resonant tunneling occurs (see Sect.6.2) at an incident energy, E_0, where there is a quasi-local level within the barriers: the transmission probability $T_d(E)$ has a sharp peak near $E = E_0$ and the thickness of the confining barriers affects mainly the width of the peak, the latter being related to the lifetime for escape out of the well; this peak gives in turn the dominant contribution to the tunneling current through the Double-Barrier. The DB potential $V_b(x)$ used in the following calculations is shown in the inset of Fig.L.1: a narrow well ($\sim 30\,\mathring{A}$) is cut in a thick and low barrier and its depth is chosen in such a way to develop a single quasi-bound level at about 10 meV above the bottom of the conduction band (which is taken as the zero of the energy scale). The confining barriers are 40 meV high and 200 $\mathring{A}$ thick.

The WKB approach [151] provides a simple way for calculating approximatively the transmission coefficient T_d of potential barriers. However, due to the non-trivial form of the barrier in the present case, we prefer to adopt a direct numerical procedure to evaluate this quantity.

In our calculation the magnetic field is assumed to be confined in the barrier region [130], i.e. in the interval $[x_1, x_2]$ shown in the inset of Fig.L.1. The time-independent Schrödinger equation associated with the Hamiltonian (L.2) admits two independent solutions Ψ_1 and Ψ_2 of the wave equation for a given energy E. One can choose Ψ and $\Phi \equiv (1/k)d\Psi/dx$ at x_1 as independent variables[158]: the same quantities at x_2 are given by

$$\Psi_2 = a\Psi_1 + b\Phi_1$$

$$\Phi_2 = c\Psi_1 + d\Phi_1 \qquad (L.3)$$

The real coefficients a, b, c and d can be determined by computing numerically two linearly independent solutions of the Schrödinger equation with energy

E in the interval $[x_1, x_2]$ and matching them with plane-waves solutions $e^{\pm ik_1 x}$, $e^{\pm ik_2 x}$, where k_1 and k_2 are the x-direction wave vector components in the two regions of constant potential outside the interval $[x_1, x_2]$ (if the DB structure is not biased, one has $k_1 = k_2$). The matching is obtained by imposing the usual conditions of continuity of Ψ and $d\Psi/dx$ (i.e. the effect of any mass mismatch at the points of discontinuity of the potential is ignored). By relating the amplitudes of the plane-waves to that of the numerical solutions at x_1 and x_2, one finds for the transmission probability $T_d(E)$ the following expression:

$$T_d(E) = \frac{4k_1}{k_2[(a+d)^2 + (b-c)^2]} \qquad (L.4)$$

Note that the conservation of the probability current at x_1 and x_2 implies [158]:

$$ad - bc = k_1/k_2 \qquad (L.5)$$

This formula provides a useful check on the accuracy of the numerical procedure used to integrate the Schrödinger equation: in the present case we used an iterative method, based on the Numerov' recursive algorithm [159], which is described in detail in Appendix O.

We plot in Fig.L.1 the logarithm of the calculated transmission probability T_d as obtained from Eq.(L.4) vs. the energy E of the incident particle, for several values of the applied magnetic field B. The curves shown refer to the particular case $X_0 = 0$ (symmetric effective barrier) where the transmission coefficient is maximum. For the purpose of comparison the $B \neq 0$ curves have been superimposed on the $B = 0$ one: actually they should be slightly shifted towards higher E/V_0, the largest shift being ~ 1.2 meV at $B = 10T$.

The results of Fig.L.1 can be easily interpreted as follows: near the bottom of the band, where the (imaginary) velocity of the electron $\hbar K/m^*$ is high, the tunnelling probability is relatively small: the Lorentz force, which is proportional to the (real) velocity $(2E/m^*)^{1/2}$, is also small. On the other hand, near the top of the barrier, although the transmission probability at zero-field is higher, the sideway deflection due to the Lorentz force is also higher and contributes to depress the transmitted flux. At resonance, however, the electron can easily complete its orbit through the confining barriers without being scattered, no matter how thick these barriers are.

From Fig.L.1 one sees that as the field strength B increases, the resonant peak in $T_d(E)$ sharpens more and more, always being equal to unity at resonance. However, the current-voltage characteristics of the double barrier

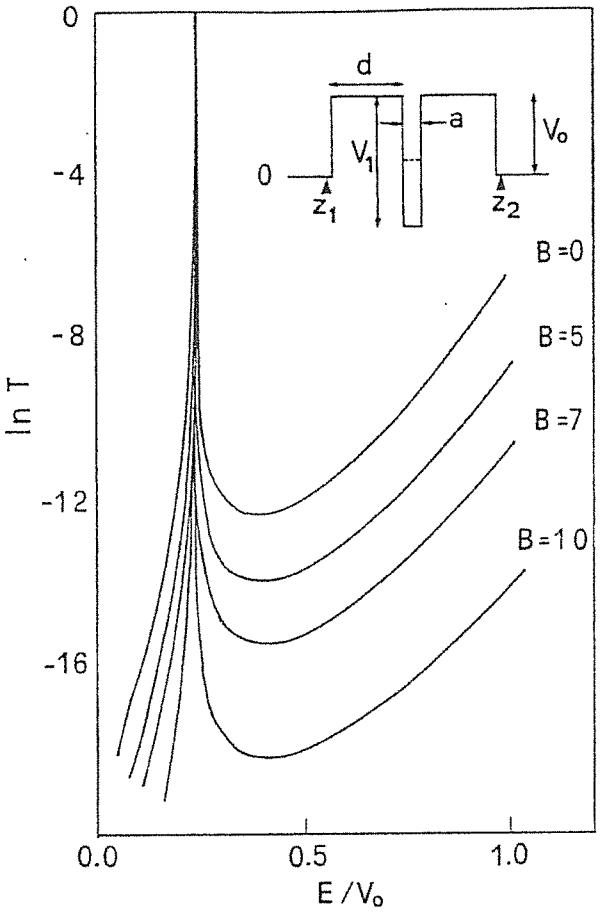

Figure L.1:
Calculated transmission probability $T_d(E)$ for different values of the applied magnetic field. The potential energy profile used (at B=0) is shown in the insert graph : $d = 200\mathring{A}$, $a = 30\mathring{A}$, $V_0 = 0.04\,eV$, $V_1 = 0.11\,eV$.
The magnetic field is assumed to be confined in $[z_1, z_2]$. The GaAs electron effective mass $m^* = 0.067m_0$ has been used.

as a diode depend strongly on the width ΔE_r of the peak (which is given approximately by Eq.(6.19) in Sect.6.2, for the case $B = 0$), the transmission probability being integrated over the incident energy E when the tunnel current is calculated (see the following). The average height of the effective barrier is roughly $\overline{V_{eff}} \sim V_0 + m^* \omega_c^2 d^2/24$, while the position of the resonant level E_r shifts with B as $E_r(B) \sim E_r(0) + \hbar\omega_c/2$: thus, from Eq.(6.19) with $\kappa_r \simeq \sqrt{2m^*(\overline{V_{eff}} - E_r(B))/\hbar^2}$, one sees that the width ΔE_r of the peak in the transmission probability decreases *exponentially* with B for large fields. The effect of the resonance in the tunnel current is thus expected to be strongly reduced by the application of large magnetic fields.

In fact the tunnel current I per unit area for a DB structure, at a given applied bias V, can be calculated within the stationary-state (free-electron) model, from [120]

$$I(V) = \frac{m^* e K_B \Theta}{2\pi^2 \hbar^3} \int_0^{V_0} T_d(E,V) N(E,V) dE \qquad (L.6)$$

$T_d(E,V)$ is the transmission coefficient of the double barrier under bias. K_B is the Boltzmann constant and Θ the temperature of the system. The supply function $N(E,V)$ accounts for the occupation of states to the left- and to the right-hand side of the DB, according to the Fermi statistic, and is given by:

$$N(E,V) = ln\Big[\frac{1 + exp((E_F - E)/K_B\Theta)}{1 + exp(E_F - E - eV)/K_B\Theta)}\Big] \qquad (L.7)$$

Here E_F is the Fermi energy of the left electrode.

We show in Fig.L.2 the tunnel current I as a function of the applied voltage V for three different values of the applied magnetic field: it is evident the strong reduction in the peak current as the magnetic field increases. The curves in Fig.L.2 have been obtained using Eq.(L.6) with $E_F = 12$ meV and $\Theta = 4.2^0 K$, and with $T_d(E,V)$ computed numerically from Eq.(L.4) (the electric field has been assumed, for simplicity, to be constant in the barrier region). Note from the figure that the current rises abruptly when the applied voltage is such that the energy E_0 of the quasi-bound state confined in the well is aligned with the Fermi energy of the left electrode, reaches a maximum value and thus drops suddenly as E_0 crosses the conduction-band edge: the two values of the voltage V at which the two crossings occur (at B=0) are indicated with arrows in the figure.

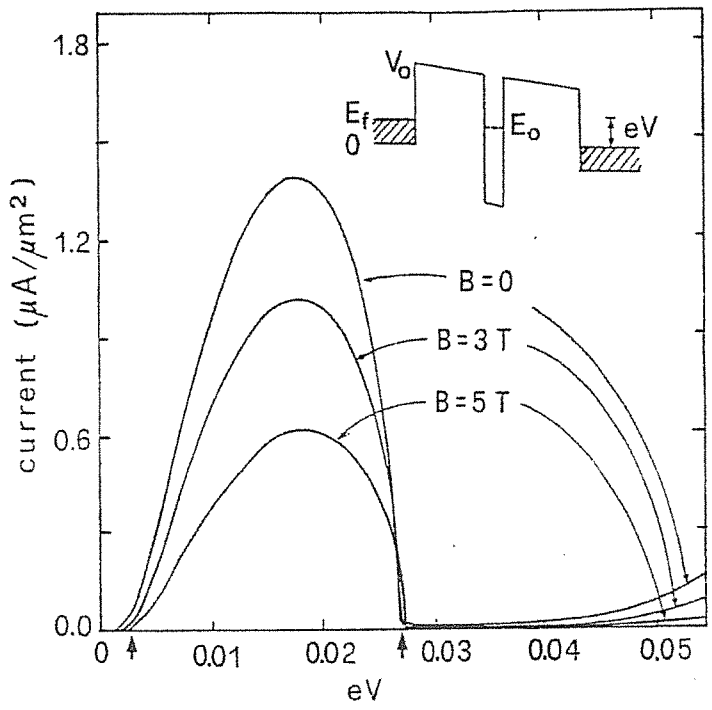

Figure L.2:
Calculated current-voltage characteristics for the Double-Barrier structure of Fig.L.1 for three different values of the applied magnetic field B. The inset shows the DB potential profile under a positive bias V, for the case B=0. The two arrows indicate where the quasi-bound state energy E_0 crosses the Fermi level and the conduction-band edge of the left electrode (taken as the zero of the energy scale), respectively.

Appendix M

Numerical solution of the time-independent Schrödinger equation.

This Appendix contains a brief description of an efficient method, based on the Numerov' algorithm[156], that can be used to integrate the one-dimensional time-independent Schrödinger equation. We used this method to calculate the Landau levels in the stationary-state calculations of Appendix I and Sect.7.10 and also to compute the transmission coefficient for the Double-Barrier in a transverse magnetic field, see Appendix L. We will follows in this exposition Ref.[159] and Ref. [155] mainly.

Let's write the one-dimensional Schrödinger equation in the form

$$\frac{d^2u}{dx^2} = f(x)u(x) \qquad (M.1)$$

where

$$f(x) = (\frac{2m^*}{\hbar^2})[V(x) - E] \qquad (M.2)$$

Here $V(x)$ is the potential energy function and m^* is the effective mass of the particle. $V(x)$ could be any potential provided it is characterized by being repulsive to the particle for large (either negative and positive) values of x and attractive in some region in between. This implies that f is positive for large values of $|x|$ and negative for the intermediate range. The values of x such that $f(x) = 0$ define the classical turning points. We assume that the potential

energy has a single minimum so that one has only two turning points, say x_1 and x_2. The desired solution $u(x)$ thus has increasing exponential behavior for $x < x_1$, oscillatory behavior between the two turning points $x_1 < x < x_2$ and decreasing exponential behavior for $x > x_2$. We look for solutions $u(x)$ which are bounded and square-integrable, with $u(\pm\infty) = 0$. Thus the energy E in Eq.(M.1) is an eigenvalue which characterizes a discrete bound state and is to be determined so that the particular solution $u_N(x)$ has exactly N nodes, where $N = 0, 1, 2, \ldots$. The canonical method for solving Eq.(1) is the Numerov' method which is based on the following basic formula :

$$[1-T(x+h)]u(x+h)+[1-T(x-h)]u(x-h) = [2+10T(x)]u(x) - \frac{h^6}{240}u^{(6)}+\ldots \qquad (M.3)$$

where

$$T(x) \equiv \frac{h^2}{12}f(x) = \frac{h^2}{12}\frac{2m}{h^2}[V(x)-E] \qquad (M.4)$$

Eq.(M.3) is a recursive formula which connects three consecutive values of $u(x)$ on a uniform one-dimensional grid of step size h. $u^{(6)}$ denotes the 6-th derivative of $u(x)$. The high order of accuracy of the formula (M.3) is to be traced to the fact that the Schrödinger equation is a linear second order differential equation with the first spatial derivative absent (for a detailed derivation of Eq.(M.3), see Ref.[159]). Eq.(M.3) in principle allows to find all subsequent points on the curve representing the eigensolution $u(x)$, given an initial estimate for the energy eigenvalue E, once the very first two points are given. The first step is thus to choose a starting value $x = a < x_1$ in the classically forbidden region to the left of the first turning point. $u(a)$ can be set arbitrarily, since one multiplicative factor is free. To get going with the Numerov' method, we require an approximation to $u(a+h)$ for the exponentially increasing solution. Quite sizeable errors are permitted here. An erroneous choice of $u(a+h)$ has the effect of admixing, to the desired exponentialy increasing solution, a component proportional to the other, exponentially decreasing. This erroneous component becomes smaller and smaller as we proceed from a towards the first turning point x_1. As a crude approximation one can use

$$u(a+h) = u(a)exp[\int_a^{a+h} f^{1/2}(x)dx] \simeq u(a)exp[(3T(a))^{1/2} + (3T(a+h))^{1/2}] \qquad (M.5)$$

The last term in (M.5) follows from approximating the integral with the trapezoidal rule. Eq.(M.5) is one step cruder than the usual WKB approximation

but is good enough for use here. From this point, given an initial estimate for the energy eigenvalue E, Eq.(M.3) can be used, in theory, to generate all the subsequent values of $u(x)$. In practice this is not quite so. One must realize that beyond the second turning point x_2 the solution u diminishes exponentially, which means that any error in this region will be magnified exponentially with respect to the solution. This can be turned to one's advantage if the direction of the integration is reversed, in which case the solution will grows exponentially and the error will *diminish* exponentially. The correct way to implement the Numerov' formula is then to integrate from the initial point $x = a$ outward to some point x_0 in the classically allowed region and then to integrate inward, from a point $x = b$ to the right of the second turning point, to the same point x_0. The logarithmic derivatives of the two functions u_i and u_o (obtained from the inward and outward integration respectively) match at x_0 only when the energy eigenvalue is correct. Let Q be the initial guess for the energy eigenvalue E in Eq.(M.2) and $u_i(x)$ and $u_o(x)$ the wave functions obtained as described above. It can be shown[159] that an improved estimate of the "true" energy can be obtained from:

$$\frac{2m^*E}{\hbar^2} \simeq \frac{2m^*Q}{\hbar^2} - \frac{u(x_0)(u_i' - u_o')}{\int u^2(x)dx} \qquad (M.6)$$

u_o' is the value of the first derivative of the wave function at $x = x_0$ obtained from the outwards integration, while u_i' is obtained from inwards integration. The free multiplicative constant is adjusted so that $u(x)$ turns out to be continuous at x_0, $u_i(x_0) = u_o(x_0)$. A sufficiently accurate expression for the first derivative needed in Eq.(M.6) is quoted in Ref.[159]:

$$u' = (1/2h)[1-2T(x+h)]u(x+h)-(1/2h)[1-2T(x-h)]u(x-h)+0(h^4) \quad (M.7)$$

Note that the error term is poorer than the basic error of the Numerov' recursive formula (M.2).

One now has an iteration scheme for finding the desired eigenvalue E: starting from a "trial" eigenvalue Q, sufficiently near to E, one can obtain improved approximations to E using (M.6) iteratively. The improvement is second order, i.e. the error of E is proportional to the square of the error of the trial value Q, once Q is close enough. The iteration scheme is terminated when convergence is achieved, i.e. when the last correction $|E - Q|$ found is sufficently small.

In practice the iteration procedure works only if the trial energy Q is already quite close to the true eigenvalue E_N, associated with the eigenfunction $u_N(x)$

which has the desired number N of nodes. Let us suppose that we know two energies Q_1, Q_2 such that $E_N \in [Q_1, Q_2]$. One then tries the value

$$Q = (Q_1 + Q_2)/2 \qquad (M.8)$$

and ascertain whether Q lies above or below E_N. This can be done by counting the nodes of the generated trial wave function. If the node count exceeds N, then the trial value Q is too high; conversely, if the node count is below N, then Q is too low. If Q lies above E_N, one replaces Q_2 by Q and repeats the process; if Q lies below E_N, Q_1 is replaced by Q and the process is repeated. Few stages of halving suffice in general to get close enough to E_N so that one can use the faster, second-order iteration formula (M.6). To ensure convergence one has in practice to:

- ascertain whether the number of nodes in $u(x)$ equals N; if not, proceed with halving, as explained above.
- if the node counting agrees, proceed to evaluate the second-order correction (M.6). The sign of the correction is right, even if the magnitude is far off. Thus, if $E - Q > 0$, Q was too low and one replaces Q_1 by Q; otherwise Q_2 is replaced by Q.
- compute the new value predicted by the second-order formula. If this new value lies between Q_1 and Q_2, it is safe to use for successive iterations; if not, the next trial value is determined using (M.8).

In practice once the correction $E - Q$ gets very small, it is not necessary to readjust Q_1 and Q_2, and it is actually safer not to, in order to avoid dangerous accumulations of round-off errors.

It remains to decide suitable values for the starting points a and b for inwards and outwards integration. If a [b] is too close to the turning point x_1 [x_2], one fails to generate enough of the desired wavefunction; if it is too far, a lot of computer time is lost by generating the wave function in a region where it is extremely small and perhaps of no particular physical interest. In practice one can choose the starting point $x = a$ [$x = b$] so that $u(a)$ [$u(b)$] is smaller than the value at the turning point $u(x_1)$ [$u(x_2)$] by a factor $exp(A)$, with A given *a priori*. In our calculations the value $A = 16$ has been chosen, corresponding to a factor of roughly 10^7.

Appendix N

Traversal times for tunneling.

One interesting quantity to determine is the time required for a particle to tunnel through a static potential barrier. It is surprising that even an apparently simple question like this has been controversial in recent years, and a variety of results have been proposed [121,122,123,157,125,126].

Consider the simple problem of scattering by a square barrier of Sec.7.4. A time *delay* for this scattering process can be calculated by following the peak of a wave packet via the method of the stationary phase [146]. According to this approach, the time it takes for the peak of the transmitted wave packet to appear, measured from the moment the peak of the incident packet strikes the barrier, is given by:

$$\tau_\varphi = \hbar \frac{d\Delta\varphi}{dE} = (\frac{m^*}{\hbar k}) \frac{d\Delta\varphi}{dk} \qquad (N.1)$$

Here $\Delta\varphi$ is the phase increase across the barrier, such that the complex amplitude of the transmitted wave is is $\sqrt{T} exp(i\Delta\phi) exp(-ikd)$. T is the transmission probability for a square barrier defined in Eq.(6.11) in the text. The above equations are correct for a wave packet characterized by a narrow momentum distribution. In the case of a very "opaque" square barrier ($Kd \gg 1$), one obtains [123]:

$$\tau_\varphi \simeq 2m^*/\hbar k K \qquad (N.2)$$

This result is independent on the barrier thickness and diverges as the energy of the incident wave packet tends to zero. It has been pointed out [125] that the method of stationary phase is an "ad hoc" approach to the tunneling time since there is no physical principle which identifies peaks on one side of the

barrier with peaks on the other side and thus expression (N.2) cannot be used as a definition of a "traversal" time. Nevertheless, this approach is widely used to discuss the time scale of a tunneling process [127,128,149,108,109].

The identification of the phase-time the with the traversal time has been questioned and several alternative definitions, relevant under different circumstances, have been proposed [122,129,157,125]. For instance, in Ref. [125] the tunneling through a time-modulated square barrier is considered. Particles incident with energy E, interacting with the periodic modulation of frequency ω, will emit or absorb quanta $\hbar\omega$. If the period of modulation is long compared to the time during which the particle interact with the barrier ($\omega\tau \ll 1$), the particle sees an effectively static barrier. At modulation frequencies high compared to the reciprocal traversal time ($\omega\tau \gg 1$) the particle tunnels through the time-averaged potential but can do it inelastically, either absorbing or emitting modulation quanta. As the modulation frequency is varied, the crossover between the two types of behavior occurs when $\omega\tau \simeq 1$, where

$$\tau = m^* d/\hbar K \qquad (N.3)$$

and d is the width of the barrier. This time can be interpreted as a barrier traversal time [125]. In this approach one can thus visualise the tunneling particle as moving freely in the inverted static potential, with an (imaginary) velocity $\hbar K/m^*$. We remark that the result (N.3) is valid in the WKB limit ($Kd \gg 1$), for energies well below the top of the barrier.

Another approach to the collision times for scattering events is based on the "dwell" time τ_d of a particle in a barrier [122], i.e. the average time a particle interacts with the barrier, whether is transmitted or reflected at the end of its stay. τ_d is defined as the ratio of the total electron density in the barrier region $\int_{-d/2}^{d/2} |\Psi|^2 dx$ divided by the incoming flux density in steady-state conditions $j = \hbar k/m^*$. For an opaque rectangular barrier one finds[125]

$$\tau_d \simeq \hbar k/v_0 K \qquad (N.4)$$

Again, this time is independent of the thickness of the barrier. The definition of τ_d does not distinguish between particles which at the end of their stay in the forbidden region have been reflected, and those that are transmitted. For this reason, this time cannot be identified with the traversal time when most of the amplitude is reflected, as it happens in the case of very thick barriers.

Another method, due to Rybachenko [129] uses the Larmor precession as a clock to measure the collision time. This approach uses incident particles

with spin polarized perpendicular to a small magnetic field confined to the region of the barrier. By considering the angle of rotation of the polarization of the transmitted and reflected particle, Rybachenko arrives at a traversal and reflection time. However, as pointed out in Ref.[145], he did not take into account that the polarization of the transmitted and reflected particles also acquires a component parallel to the magnetic field. If this effect is included [145] his method also yields the traversal time (N.4) given in Ref.[125].

We quote for completeness the main result of Ref.[157], in which the propagation through a square barrier of a uniform amplitude pulse with a well defined front in real space is studied: a "signal" propagation with constant velocity is found for these pulses, and a traversal time again of the form (N.3) is derived.

Bibliography

[1] " *Molecular Beam Epitaxy and Heterostructures*", NATO Advanced Science Institute Series (Nijhoff, Dordrecht, 1985), L.L.Chang and K.Ploog Eds.

[2] *"Metal Organic Vapor Phase Epitaxy"*, (North-Holland, Amsterdam, 1984), J.B.Mullin, S.J.C.Irvine ,R.H.Moss, P.N.Robson and D.R.Wight Eds.

[3] L.Esaki, and R.Tsu, IBM J. Res. Develop. **14**, 61 (1970).

[4] K.Ploog and K.Graf, *"Molecular Beam Epitaxy of III-V Compounds"*, (Springer, Berlin, 1984).

[5] L.L.Chang, J. Vac. Sci. Techn. **B1**, 120 (1983).

[6] J.K.Furdyna and J.Kossut, *Superlattices & Microstructures*, **2**, 89 (1986).

[7] G.Belle, J.C.Maan and G.Weimann, Sol. St. Comm. **56**, 65 (1985).

[8] K.Ploog and G.Dohler, Adv. Phys. **32**, 285 (1983).

[9] M.Heiblum, E.E.Mendez and F.Stern, Appl. Phys. Lett. **44**, 1064 (1984).

[10] M.Abe, T.Mimura, K.Nishiuici, A.Shibatomi and M.Kobayashi, IEEE, J. Quantum Electron., **QE-22**, 1870 (1986).

[11] L.Esaki, Proceedings of the 17-th International Conference on the Physics of Semiconductors, (S.Francisco, Springer-Verlag, 1984). J.D.Chadi ,W.A.Harrison Eds.

[12] L.L.Chang, N.Kawai, G.A.Sai-Halasz, R.Ludeke and L.Esaki, Appl. Phys. Lett. **35**, 939 (1979).

[13] M.Altarelli, Phys. Rev. B**28**, 842 (1983) and in *"Applications of High Magnetic Fields in Semiconductor Physiscs"* , Springer (Berlin 1983). G. Landwehr ed.

[14] Y.Gouldner, G.Bastard, J.P.Vieren, M.Voos, J.P.Faurie and A.Million, Phys. Rev. Lett. **51**, 907 (1983).

[15] For a review, see e.g. J.Y. Marzin, *Superlattices & Microstructures* , to be published.

[16] G.Osbourn, R.Biefeld and P.Gourley, Appl. Phys. Lett. **41**, 172 (1982).

[17] P.Voisin, E.Delalande, M.Voos, L.L.Chang, A.Segmuller, C.A.Chang and L.Esaki, Phys. Rev. B**30**, 2276 (1984).

[18] H.Brugger and G.Abstreiter, J. Physique (Colloque), C-**5**, 321 (1987).

[19] R.Dingle, Festkorperprobleme Vol. XV, page 21 (1975). J.Queisser Ed.

[20] R.C.Miller, D.A.Kleinman and A.C.Gossard, Phys. Rev. B**28**, 7085 (1984).

[21] J.Menendez, A.Pinczuk, D.J.Werder, A.C.Gossard and J.H.English, Phys. Rev. B**33**, 8863 (1986)

[22] D.W.Niles and G.Margaritondo, Phys. Rev. B**34**, 2923 (1986).

[23] G.Bastard, Phys. Rev. bf B24, 5693 (1981).

[24] M.Altarelli, Band structure, Impurities and Excitons in Superlattices, Lecture notes for the Winter School on Semiconductor Heterojunctions and Superlattices, Les Houches (1985).

[25] F.Bassani and G.Pastori-Parravicini, Electronic states and optical transitions in Solids, Pergamon Press, (1975). R.A.Ballinger Ed.

[26] E.O.Kane, Semiconductors and Semimetals, (Academic Press, New York, 1966). K.Willardson and A.C.Beer Eds.

[27] L.M.Roth, B.Lax and S.Zwerdling, Phys. Rev. **114**, 90 (1959)

[28] L.D.Landau and E.M.Lifshitz, Quantum Mechanics, (Pergamon Press, 1977).

[29] H.J.Lee, Y.Juravel, J.C.Woolley and A.J.Springthorpe, Phys. Rev. B**21**, 658 (1980).

[30] J.M.Luttinger and W.Kohn, Phys. Rev. **97**, 869 (1955).

[31] M.F.N.Schuurmans and G.W. t'Hooft, Phys. Rev. B**31**, 8041 (1985).

[32] J.M.Luttinger, Phys. Rev. **102**, 1030 (1956)

[33] S.S.Nedorezov, Sov. Phys. Sol. State **12**, 1814 (1972).

[34] A.Fasolino and M.Altarelli, Two-Dimensional Systems, Heterostructures and Superlattices, (Springer, Berlin, 1984). G.Bauer, F.Kuchar and H.Heinrich Eds.

[35] M.Altarelli, U.Ekenberg and A.Fasolino, Phys. Rev. B**32**, 5138 (1985).

[36] M.Altarelli and N.Lipari, Phys. Rev. B**9**, 1733 (1974).

[37] M.Altarelli and A.Fasolino,*"Highlights of Condensed Matter Theory"*, eds. F.Bassani, F.Fumi, and M.P.Tosi (1983).

[38] R.Sooryakumar, D.S.Chemla, A.Pinczuk, A.Gossard, and W.Wiegmann, Proc. 17-th Int. Conference on the Physics of Semiconductors, S.Francisco (1984).

[39] J.N.Schulman and Y.C.Chang, Phys. Rev. B**31**, 2056 and 2069 (1985).

[40] K.von Klitzing, G.Dorda and M.Pepper, Phys. Rev. Lett. **45**, 494 (1980).

[41] D.C.Tsui, A.C.Gossard and H.L.Stormer, Phys. Rev. Lett. **48**, 1559 (1982).

[42] H.L.Stormer, Festkörperprobleme Vol. XXIV, page 25 (1984). J.Queisser Ed.

[43] S.R.Yang, D.Broido and L.J.Sham, Phys. Rev. B**32**, 6630 (1985).

[44] G.Bangert and G.Landwehr, Surf. Sci. **170**, 593 (1986)

[45] E.D.Palik, G.S.Picus, S.Teitler and R.F.Wallis, Phys.Rev. **122**, 475 (1971)

[46] G.Lindemann, R.Lassnig, W.Seidenbush and E.Gornik, Phys. Rev.B**28**, 4693 (1983)

[47] J.M.Chamberlain, P.E.Simmonds, R.A.Stradling and C.C.Bradley, *"Proceedings of the 11 th International Conference on the Physics of Semiconductors"* , Warsaw (1972).

[48] D.C.Rogers, J.Singleton, R.J.Nicholas, C.T.Foxon, and K.Woodbridge, Phys. Rev. B**34**, 4002 (1986)

[49] J.C.Maan, A.Fasolino, G.Belle, M.Altarelli and K.Ploog, Phys. Rev. B**30**, 2253 (1984)

[50] C.R.Pidgeon and R.N.Brown, Phys. Rev. **146**, 575 (1966)

[51] P.Voisin, G.Bastard and M.Voos, Phys. Rev. B**29**, 835 (1984)

[52] G.D.Sanders, Y.C.Chang, Phys. Rev. B**32**, 5517 (1985)

[53] R.C.Miller, A.C.Gossard, G.D.Sanders, Y.C.Chang, J.N.Schulman, Phys. Rev. B**32**, 8452 (1985)

[54] Subsequent informations have revealed that the 90 Å sample of Ref. 5 had in fact a 80 Å well thickness.

[55] J.C.Maan, A.Fasolino, G.Belle, M.Altarelli and K.Ploog, *"Proceedings of the 17th International Conference on the Physics of Semiconductors"*, eds. J.D.Chadi and W.A.Harrison, Springer - New York (1985)

[56] M.H.Meynadier, C.Delalande, G.Bastard and M.Voos, Phys. Rev. **B31**, 5539 (1985)

[57] J.A.Brum and G.Bastard, J. Phys. **C18**, L789 (1985)

[58] F.Ancilotto, A.Fasolino and J.C.Maan, *Superlattices & Microstructures* **3**, 187 (1987)

[59] F.Ancilotto, A.Fasolino and J.C.Maan, Phys. Rev. **B38**, 1788 (1988).

[60] R.C.Miller, D.A.Kleinmann, W.T.Tsang and A.C.Gossard, Phys. Rev. **B24**, 1134 (1981)

[61] S.Tarucha, H.Okamoto, Y.Iwasa and N.Miura, Solid State Commun. **52**, 815 (1984)

[62] Q.H.F. Vrehen, J. Phys. Chem. Sol., **29**, 129 (1968)

[63] S.R.E. Yang and L.J. Sham, Phys. Rev. Lett. **58**, 2598 (1987).

[64] A.Petrou, G.Waytena, X.Liu, J.Ralston and G.Wicks

[65] G.E.W.Bauer and T.Ando, Phys. Rev. **B37**, 3130 (1988).

[66] R.L.Greene, K.K.Bajaj and D.E.Phelps, Phys. Rev. **B29**, 1807 (1984).

[67] G.Bastard, E.E.Mendez, L.L.Chang and L.Esaki, Phys. Rev. **B26**, 1974 (1982).

[68] O.Akimoto and H.Hasegawa, J. Phys. Soc. Jpn. **22**, 181 (1967)

[69] B.Deveaud, A.Regreny, A.Romestein and J.C.Maan, private communication.

[70] U.Rossler, Sol. St. Comm. **49**, 943 (1984).

[71] M.Braun, U.Rossler, J.Phys. **C18**, 3365 (1985)

[72] See, for instance, S.A.Lyon, J. Luminesc. **35**, 121 (1986).

[73] J.Shah, IEEE J. Quant. Electronics, **QE-22**, 1728 (1986).

[74] J.F.Ryan, R.A.Taylor, A.J.Turberfield and J.M.Warlock, Surf. Sci. **170**, 511 (1986).

[75] W.Cai, M.C.Marchetti and M.Lax, Phys. Rev. B**34**, 8573 (1986).

[76] K.Leo, W.W. Rühle, H.J.Queisser and K.Ploog, Phys. Rev. B**37**, 7121 (1988).

[77] K.Zerrouati, F.Fabre, G.Bacquet, J.Bandet, J.Frandon, G.Lampel and D.Paget, Phys. Rev. B**37**, 1334 (1988).

[78] M.Potemski, J.C.Maan, A.Fasolino, F.Ancilotto, K.Ploog and G.Weimann: "Spin dependent relaxation in Quantum Wells", Proceedings of the 20th International Conference on the Physics of Semiconductors (Warsaw,1988).

[79] M.Potemski, J.C.Maan, A.Fasolino, F.Ancilotto, K.Ploog and G.Weimann, to be published.

[80] J.C.Maan, M.Potemski and Y.Y.Wang, Proceedings of the International Conference on the Physics of Semiconductors in High Magnetic Fields, Wurzburg (1988). Springer-Verlag, to be published.

[81] Z.Schlesinger, S.J.Allen, Y.Yafet, A.C.Gossard and W.Wiegmann, Phys. Rev. B**32**, 5231 (1985).

[82] H.R.Trebin, U.Rossler and R.Ranvaud, Phys. Rev. B**20**, 686 (1979).

[83] F.Ancilotto and A.Fasolino, unpublished.

[84] U.Ekenberg and M.Altarelli, Phys. Rev. B**32**, 3712 (1985).

[85] A.Broido and L.J.Shamm, Phys. Rev. B**31**, 888 (1985).

[86] Z.Schlesinger and W.I.Wang, Phys. Rev. B**33**, 8867 (1986).

[87] H.Schlosser and P.M.Marcus, Phys. Rev. **131**, 2529 (1969). Appendix 1.

[88] N.Lipari and M.Altarelli, Phys. Rev. B**15**, 4883 (1977).

[89] D.C.Reynolds and T.C.Collins, *Excitons: their properties and uses*, Academic press (1981).

[90] L.Pauling and E.B.Wilson, Introduction to Quantum Mechanics, Mc-Graw Hill, New York (1935).

[91] C.Hermann and C.Weisbuch, Phys. Rev. B**15**, 823 (1977).

[92] R.L.Aggarwal, Semiconductors and Semimetals, Academic Press (1972). R.K.Willardson,A.C.Beer Eds.

[93] K.Hess, D.Bimberg, N.O.Lipari, J.U.Fischbach and M.Altarelli, Proc. 13-th International Conference on the Physics of Semiconductors, Rome (1976). F.G.Fumi Ed.

[94] K.Suzuki and J.C.Hensel, Phys. Rev. bf B9, 4184 and 4219 (1974).

[95] R.Grisar, H.Wachernig, G.Bauer, J.Wlasak, J.Kowalski and W.Zawadzky, Phys. Rev. B**18**, 4355 (1978).

[96] A.Chomette, B.Lambert, B.Deveaud, F.Clerot, A.Regreny and G.Bastard, Europhys. Lett., **4**, 461 (1987).

[97] R.C.Miller and D.A.Kleinman, J. Lumin. **30**, 520 (1985).

[98] See, for instance, E.O.Kane, in "*Tunneling Phenomena in Solids*", eds. E.Burstein and S.Lundqvist (Plenum, New York, 1969), page 1.

[99] D.J.Ben Daniel and C.B.Duke, Phys. Rev. **152**, 683 (1966).

[100] J.Bardeen, Phys. Rev. Lett. **6**, 57 (1961).

[101] B.D.Josephson, Phys. Lett. **1**, 251 (1962).

[102] L.O.Landau and E.M.Lifshitz, *Quantum Mechanics: non- relativistic theory*, Pergamon (N.Y.,1981), Chapter III.

[103] Tsu R. and Esaki L. 1973 Appl. Phys. Lett. **22** 562.

[104] Tsu R. and Esaki L. 1973 Appl. Phys. Lett. **22** 562 ; Chang L.L., Esaki L. and Tsu R. 1974 Appl. Phys. Lett. **24** 593.

[105] T.C.L.G. Sollner, W.D.Goodhue, P.E.Tannenwald, C.D.Parker and D.D.Peck, Appl. Phys. Lett. **43**, 588 (1983).

[106] T.C.L.G.Sollner, E.R.Brown, W.D.Goodhue and H.Q.Le, Appl. Phys. Lett. **50**, 332 (1987).

[107] Ricco B. and Azbel M. 1984 Phys. Rev. B**29** 1970.

[108] J.R.Barker, Physica **134**B, 22 (1985).

[109] X.Ravaioli, M.A.Osman, W.Pötz, N.Kluksahl and D.K.Ferry, Physica **134**B, 36 (1985).

[110] S.Luryi, Appl. Phys. Lett. **47**, 490 (1985).

[111] T.Weil and B.Vinter, Appl. Phys. Lett. **50**, 1281 (1987).

[112] M.C.Payne, J. Phys. C **19**, 1145 (1986).

[113] P.J.Price, Phys. Rev. B**36**, 1314 (1987).

[114] K.K. Choi, B.F. Levine,C.G. Bethea, J. Walker and R.J. Malik, Phys. Rev. Lett. **59**, 2459 (1987).

[115] F.Capasso, K.Mohammed and A.Y.Cho, Appl. Phys. Lett. **48**, 478 (1986).

[116] Merzbacher E. 1970 "Quantum Mechanics" Wiley (New York).

[117] F.Capasso, K.Mohammed and A.Y.Cho, IEEE J. of Quantum Electronics, **QE-22**, 1853 (1986).

[118] M.Tsuchiya, T.Matsusue and H.Sakaki, Phys. Rev. Lett. **59**, 2356 (1987).

[119] E.E.Mendez, J. de Physique Colloque c5, 423 (1987).

[120] Duke C.B. 1969 "Tunneling in Solids" Academic Press (New York).

[121] L.A. Mac Coll, Phys. Rev. **40**, 621 (1932).

[122] F.T.Smith, Phys. Rev. **118**, 349 (1960).

[123] T.E.Hartman, J. Appl. Phys. **33**, 3427 (1962).

[124] K.W.H.Stevens, J. Phys. C **16**, 3649 (1983).

[125] M.Büttiker and R.Landauer, Phys. Rev. Lett. **49**, 1739 (1982).

[126] J.R.Fletcher, J. Phys. C **18**, L55 (1985).

[127] S.Collins, D.Lowe and J.R.Barker, J. Phys. **C20**, 6233 (1987).

[128] S.Collins, D.Lowe and J.R.Barker, J. Phys. C **20**, 6213 (1987).

[129] V.F.Rybachenko, Sov. J. Nucl. Phys. **5**, 635 (1967).

[130] P.Gueret, A.Baratoff and E.Marclay, Europhys. Lett. **3**, 367 (1987).

[131] P.Gueret, U.Kaufmann and E.Marclay, Electronics Lett. **21**, 344 (1985).

[132] L.Eaves, D.C.Taylor, J.C.Portal and L.Dmowsky, Springer Series in Solid State Science **67**, 96 (1986).

[133] J.K.Maan, Festkörperprobleme **27**, 137 (1987).

[134] L.Brey, G.Platero and C.Tejedor, preprint.

[135] J.K.Jain and S.Kivelson, Phys. Rev. B**37**, 4111 (1988); ibid. **37**, 4276 (1988).

[136] H.A. Fertig and B.I. Halperin, "Transmission coefficient of an electron through a saddle-point potential in a magnetic field", preprint.

[137] H.Tall-Ezer and R.Kosloff, J. Chem. Phys. **81**, 3967 (1984).

[138] W.Kohn, in "Solid State Physics", F.Seitz and D.Turnbull eds., (Academic, New York, 1957), vol.5, page 257.

[139] A.Messiah, *Quantum Mechanics*, North-Holland, Amsterdam (1975), vol.1.

[140] R.B.Gerber, R.Kosloff and M.Berman, Comp. Phys. Rep. **5**, 59 (1986).

[141] R.Kosloff, J. Phys. Chem. **92**, 2087 (1988).

[142] M.Abramowitz and I.Stegun, "em Handbook of Mathematical Functions" (Dover, New York, 1964).

[143] L.Shiff, *Quantum Mechanics*, Mc Graw Hill (third edition), page 64.

[144] M.D.Feit, J.A.Fleck and A.Steigen, J. Comp. Phys. **47**, 412 (1982).

[145] M. Büttiker, Phys. Rev. B**27**, 6178 (1983).

[146] E.P.Wigner, Phys. Rev. **98**, 145 (1955).

[147] M.Sargent, M.O.Scully and W.E.Lamb, *Laser Physics*, (Addison Wesley, London, 1974), page 410.

[148] L.Shiff, *Quantum Mechanics*, Mc Graw Hill (third edition), page 521.

[149] E.H.Hauge, J.P.Falck and T.A.Fjeldly, Phys. Rev. B**36**, 4203 (1987).

[150] E.A.Johnson, A.MacKinnon and C.J.Goebel, J. Phys. C**20**, L521 (1987).

[151] C.M.Bender and S.A.Orszag, "*Advanced Mathematical Methods for Scientists and Engineers*", (McGraw-Hill, Singapore,1984).

[152] F.Ancilotto, A.Selloni, L.F.Xu and E.Tosatti, submitted to Phys. Rev. B.

[153] F.Ancilotto, A.Selloni and E.Tosatti, unpublished.

[154] F.Ancilotto, J. Phys. C**21**, 4657 (1988).

[155] P.C.Chow, Am. J. Phys. **40**, 730 (1972).

[156] B.Numerov, Publ. Obs. Central Astrophys. Russian **2**, 188 (1933).

[157] K.W.H.Stevens, Eur. J. Phys. **1**, 98 (1980).

[158] Price P. 1986 "*Superlattices & Microstructures*" **2** 213.

[159] Blatt J.M. 1967 J. Comp. Phys. **1** 382.

[160] E.E.Mendez, E.Calleja and W.I.Wang, Phys. Rev. B**32**, 6026 (1986).